MORPHOLOGICAL MAPPING AND TIDAL STRESS MODELING OF STRIKE-SLIP FAULTS ON GANYMEDE

by

Marissa E. Cameron

submitted in partial fulfillment of the requirements for the degree of

DOCTOR OF PHILOSOPHY

in

GEOLOGY AND GEOPHYSICS

at the

UNIVERSITY OF HAWAIʻI AT MĀNOA

May 2018

Dissertation Committee

Bridget Smith-Konter, Chairperson
Sarah Fagents
Paul Lucey
Stephen Martel
Peter Mouginis-Mark
H. Ronald Riggs

ACKNOWLEDGEMENTS

I have been fortunate to have many people help guide me through this incredible journey to receive my Ph.D. Joshua Villalobos, my geology instructor from my time at El Paso Community College, first sparked my interest in the field many years ago. His help made it possible for me to pursue a Bachelor's at the University of Texas at El Paso where I met my first research advisor while working on a seismology project, Aaron Velasco. I thank Tina Carrick for her excellent mentorship throughout my Bachelor's and Master's degrees, and Bridget Smith-Konter, who took me under her wing and laid the groundwork for me to attend the University of Hawai‘i for my Ph.D. Bridget has been a wonderful advisor and I consider myself very lucky to have gotten to know her and her family. I wish to thank Robert Pappalardo, Geoffrey Collins, and Donald A. Patthoff, who have all made time for me in their busy schedules to encourage and advise me every step of the way. I am grateful to the contributions made by my dissertation committee: Sarah Fagents, Paul Lucey, Pete Mouginis-Mark, and H. Ron Riggs. And a special thanks to committee member Stephen Martel, whose door was always open for countless conversations that have helped me grow as a geologist. On a personal note, I thank my parents, siblings, family, and friends who have gone above and beyond to make me feel like I have a home no matter where I am. And finally, to my husband Sam Howell, who found ways to support me even from across an ocean.

ABSTRACT

Jupiter's icy moon Ganymede displays a fractured surface with many morphologically distinct regions of inferred strike-slip faulting that may be important to the structural development of its surface. Ganymede is dominated by heavily grooved terrain, which is likely the result of extensive normal faulting, but the role of strike-slip tectonism in shaping the surface of Ganymede is not well understood. This dissertation addresses strike-slip faulting on Ganymede in a three-part study. The first part uses detailed maps based on high-resolution *Galileo* and *Voyager* images of nine geologically relevant sites spanning Ganymede's surface to document evidence of strike-slip faulting. Abundant evidence of strike-slip faulting exists at each site, indicating that strike-slip tectonism strongly affects Ganymede's surface. The second part combines the detailed mapping results with a numerical tidal stress model (SatStress) that accounts for Ganymede's orbital interactions with Jupiter and the other Galilean satellites, as well as the internal structure of Ganymede. The modeling results suggest, under particular circumstances, diurnal and secular tidal stresses such as nonsynchronous rotation (NSR) may have been sufficient to induce Coulomb failure and generate strike-slip faulting. In six of the nine regions the fault zone's predicted slip is compatible with the slip deduced from the maps. The third part focuses on the effects of diurnal tidal stresses alone, and takes into account Laplace-like resonances among Ganymede, Europa, and Io that may have once led Ganymede to acquire an eccentricity as high as ~0.07 that may have been stable for 10^7-10^9 years. This previous period of high eccentricity may have allowed diurnal tidal stresses to drive faulting during a past period of active tectonism. Assuming a conservative eccentricity of 0.05, Coulomb failure can be achieved without the need to invoke a secular stresses such as NSR, but only for a past, high eccentricity case and limited depths of less than 250 m. In sum, tidal contributions are

predicted to vary in magnitude over time as the dynamics of the Galilean system evolved, and can help drive strike-slip faulting. These findings should be of use in future missions to Jupiter and its Galilean moons.

TABLE OF CONTENTS

LIST OF TABLES

LIST OF FIGURES

CHAPTER 1. INTRODUCTION

CHAPTER 2. MORPHOLOGICAL MAPPING OF GANYMEDE: INVESTIGATING THE ROLE OF STRIKE-SLIP TECTONICS IN THE EVOLUTION OF TERRAIN

CHAPTER 3. TIDAL STRESS MODELING OF GANYMEDE: STRIKE-SLIP TECTONISM AND COULOMB FAILURE

CHAPTER 4. GANYMEDE THEN AND NOW: HOW PAST ECCENTRICITY MAY HAVE ALTERED TIDALLY DRIVEN COULOMB FAILURE

CHAPTER 1. INTRODUCTION

We live in an era where new stars, moons, and planets are discovered in far-flung reaches of the universe on a regular basis. As exotic and grand as these new discoveries are (Welsh et al., 2011), vast information is still waiting to be learned about bodies in our own galactic backyard. Consider Jupiter, the largest planet in the Solar System. Jupiter has been of interest to mankind since ancient times, being one of five planets visible to the naked eye from Earth. Galileo Galilei is credited with being the first to turn his home-built telescope to the gas giant in 1610 (Drake, 1976; Pasachoff and Leich, 2015). He observed what he initially considered to be four stars orbiting Jupiter (Figure 1.1). Today we call these "stars," now known to be moons, the Galilean satellites: Io, Europa, Ganymede, and Callisto (Morrison, 1982; Showman and Malhotra, 1999). While Galileo may have garnered acclaim for his discovery, the names of each moon come from Simon Marius (Owen, 1976), a German astronomer thought to have independently discovered the same four moons, noting his observations one day after Galileo's (Pasachoff, 2015). Regardless of any controversy surrounding their initial discovery, the Galilean satellites helped bring an end to the Aristotelian "geocentric" perspective of universe, for how could a planet have smaller bodies orbiting it if the dominant belief at that time was that all celestial bodies should circle the Earth (Taton et al., 2003)?

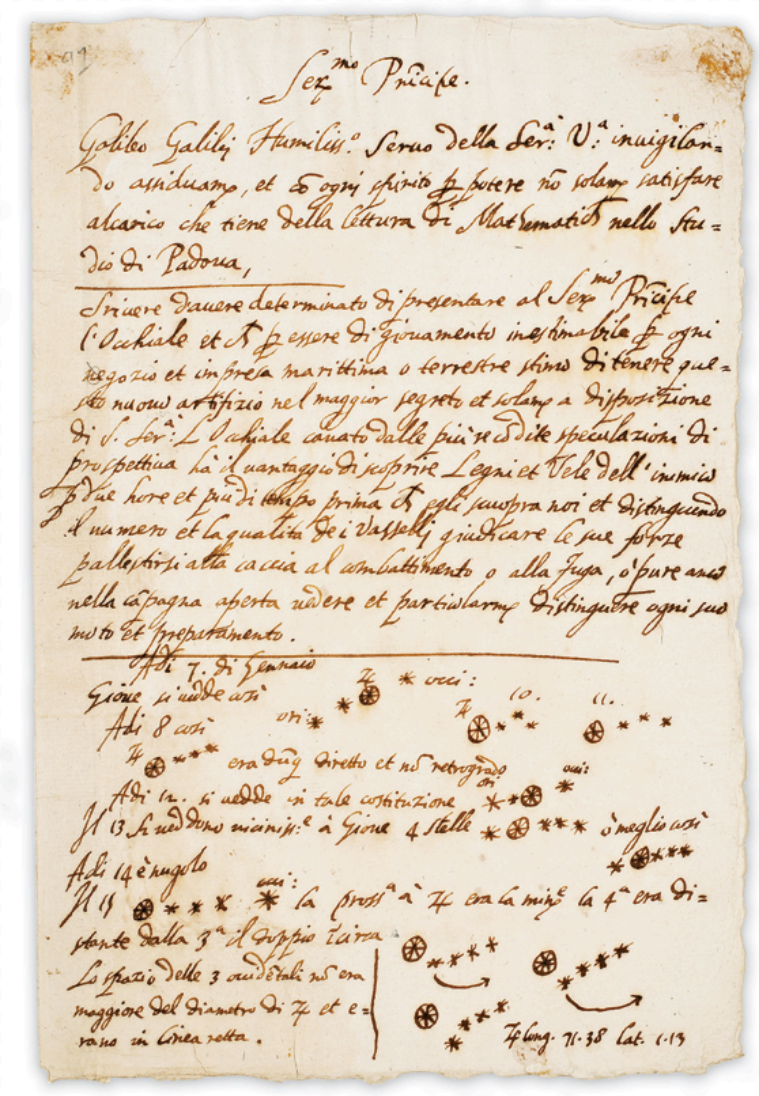

Figure 1.1. Galileo's notes on Jupiter and the Galilean satellites. Image Credit: University of Michigan Special Collections Library.

Centuries later, humankind finally set out to visit the Jupiter system with a series of flybys conducted by numerous spacecraft. NASA's *Pioneers 10* and *11* made their closest approaches in 1973 and 1974 respectively, taking the first close-up images of Jupiter and its moons (Anderson et al., 1988). NASA's *Voyagers 1* and *2* flew by in 1979 and sent back a wealth of information about the Galilean satellites and discovered Jupiter's ring system (Hanel et al., 1979). The joint NASA-ESA solar probe, *Ulysses*, returned magnetosphere data from Jupiter while using the gas giant to maneuver the probe into a polar orbit in 1992, and again in 2004 (Tsurutani et al., 1993). The joint NASA-ESA mission *Cassini* captured images of Jupiter while

en route to Saturn in 2000 (Porco et al., 2003), and NASA's *New Horizons* studied the Galilean satellites using infrared spectral imaging while using Jupiter as a gravity assist to Pluto in 2007 (Grundy et al., 2007). Of great importance is the contribution of the aptly named *Galileo* probe, which became the first spacecraft to enter orbit about Jupiter in 1995 until its planned descent and impact into the atmosphere in 2003 (Kivelson et al., 1996). In the almost eight years in orbit, the flagship mission conducted 33 total flybys of the four Galilean satellites. The data from these flybys that made the research of this dissertation possible.

Jupiter and its Galilean satellites form a dynamic system (Table 1.1): Io, the closest to Jupiter and smallest of the group, is home to over 400 active volcanoes (Lopes and Spencer, 2007). Europa sustains a global liquid ocean under an ice shell that may harbor life (Kivelson et al., 2000; Chyba and Phillips, 2001). Ganymede, also thought to have a liquid ocean overlain by ice, holds the title of largest satellite in the Solar System - even larger than the planet Mercury (Schubert et al., 1996; Kivelson et al., 2000). Callisto has one of the most heavily cratered surfaces in the Solar System, in fact the surface is so saturated with craters, any new crater tends to erase an existing one (Hartmann, 1984).

Table 1.1. Galilean satellite characteristics.

Moon	Diameter (km)	Mass (kg)	Semi-major axis (km)	Orbital period (days)	Eccentricity
Io	3660.0	8.93×10^{22}	4.218×10^{5}	1.769	.0041
Europa	3121.6	4.8×10^{22}	6.711×10^{5}	3.551	.0094
Ganymede	5268.2	1.48×10^{23}	1.070×10^{6}	7.115	.0013
Callisto	4820.6	1.08×10^{23}	1.883×10^{6}	16.69	.0074

As the Galilean satellites orbit Jupiter, the gravity of each body influences each other, causing tidal stresses (Greenberg et al., 1998). Like the Earth and Moon, the Galilean satellites are synchronously locked to Jupiter, meaning that the same side of the satellite always faces Jupiter and creates a tidal bulge on the satellite (Burns, 1976; Melosh, 1977; Helfenstein and Parmentier, 1980). On Earth, this tidal bulge is the cause of the ocean tides, where a bulge of water on either side of the Earth during "low tide" is observed on both sides of the planet

(Farrell, 1973). On Galilean satellites, this tidal bulge may be large enough to physically deform the surface (Yoder and Peale, 1981). Furthermore, the orbits of the Galilean satellites are elliptical rather than circular, meaning the tidal bulge will vary in both size and position as it changes distance from Jupiter during its diurnal orbit (Murray and Dermott, 1999). Therefore, the influence of tides provides a major source of stress and heat (Greenberg et al., 1998; Hoppa et al., 1999; Nimmo and Gaidos, 2002). Finally, the innermost Galilean satellites (Io, Europa, and Ganymede) orbit Jupiter in a configuration known as a Laplacian resonance – a resonance that is described by a three-body system with an orbital period ratio of 1:2:4 (Showman and Malthotra, 1997). Simply put, for every one orbit about Jupiter that Ganymede completes, Europa completes two, and Io completes four. The influence of this resonance may cause increased tidal heating within the interiors of the satellites, perhaps driving geologic activity on Io, the presence of a liquid water ocean under the icy surface of Europa, and the focus of this dissertation, tectonism on Ganymede (Yoder, 1979; Yoder and Peale, 1981; Greenberg, 1987; Tittemore, 1990; Malhotra, 1991; Showman and Malhotra, 1997).

Unlike Earth, Ganymede's surface is not composed of rock, but water ice. Global images of Ganymede reveal two distinct ice terrain types: an older dark terrain and a younger, grooved, light terrain. Dark terrain covers about one-third of the satellite and is characterized by an ancient, heavily cratered appearance (Shoemaker et al., 1982; Murchie et al., 1986, 1989; Neukum, 1997; Neukum et al., 1998; Prockter et al., 1998; Zahnle et al., 2003; Schenk et al., 2004). Much of the dark terrain is estimated to date from > 4 Gyr based on measured crater densities (Zahnle et al., 2003). The dark color of the terrain is inferred to be due to a thin, loose deposit overlying brighter, icy material (Cassachia and Strom, 1984; Croft and Strom, 1985; Allison and Clifford, 1987; Figueredo et al., 1999; Moore et al., 1999; Prockter et al., 2000). Light terrain covers the remaining two-thirds of Ganymede's surface and is characterized by a subparallel groove system that cross-cuts the older, dark terrain (Murchie et al., 1986; Pappalardo et al., 1998; Prockter et al., 2000; Collins, 2009). Crater density within the grooved light terrain is 2 to 10 times less than in the dark terrain, and light terrain is inferred to have been emplaced between 400 Myr and 4 Gyr ago. The large range in time reflects uncertainties in impact cratering rate histories (Zahnle et al., 1998; Neukum et al., 1998; Zahnle et al., 2003).

Although the dark and grooved light terrain may be composed of ice, the extreme cold of the outer solar system allows the ice to behave in a way similar to rocks, therefore analogous Earth processes may be used when considering the formation and interaction of these terrains. Much of the grooved light terrain is likely affected by extensional tectonism, such as horst-and-graben normal faulting, pulling the terrain apart (Shoemaker et al., 1982; Belton et al., 1996, Pappalardo et al., 1998; Dombard and McKinnon, 2001; Bland and Showman, 2007). Many authors have described these normal faulting processes since the emergence of *Voyager* data. Far fewer studies have investigated the role of a different style of tectonism: strike-slip faulting. Strike-slip faulting occurs where fault walls shift past one another laterally (Pollard et al., 1982; Naylor et al., 1986; Woodcock and Fisher, 1986; Pappalardo and Greeley, 1995), and is most famously described on Earth at the San Andreas Fault in California (Zoback et al., 1987; Graymer et al., 2002). When viewing the San Andreas from above (Figure 1.2), features such as riverbeds or fences that have been split and offset from each other. Strike-slip behavior in satellite images is observed when viewing the grooved terrain of Ganymede (Murchie and Head, 1988; Cameron et al., 2018). These regions of strike-slip faulting may be important when considering Ganymede's tectonic history, and are a focus of this dissertation.

Figure 1.2. San Andreas Fault (left) and Ganymede's Dardanus Sulcus (right). San Andreas Fault Image Credit: NOAA/NGDC.

Perhaps one of the most fascinating aspects of Ganymede is the idea that a global, subsurface liquid water ocean could lie just below the ice shell (Ojakangas and Stevenson, 1989; Kivelson et al., 1997; Carr et al., 1998). When the *Galileo* space probe orbited Jupiter and imaged its moons between 1995 and 2003, we not only gained higher resolution imagery, but improved

geophysical data. Magnetic data from *Voyager* and *Galileo* provided evidence for an induced magnetic field, suggesting the presence of a conductive layer, i.e. a subsurface liquid water ocean (Ojakangas and Stevenson, 1989; Kivelson et al., 1997; Carr et al*.,* 1998). The presence of a subsurface liquid water ocean has unique implications for the evolution of Ganymede's tectonic history and stress mechanisms, particularly if the ocean layer acts as an interface to separate the ice shell from the deep interior of the moon. This process may allow for an additional source of stress within the icy shell, known as nonsynchronous rotation (NSR), in which the surface of the moon rotates at a different rate than the interior (Helfenstein and Parmentier, 1985; Ojakangas and Stevenson, 1989). In addition to the induced magnetic field, an internally generated magnetic field on Ganymede was also inferred, making it the only moon known to have one. This field probably formed in a similar fashion to Earth's: as a result of conducting, mobile material from a molten or semi-molten iron core (Anderson, 1996; Sohl et al, 2002).

While Ganymede has likely not been active during recent geologic time, studying the history of tectonics and the stresses influencing the icy moon may have greater implications for Ganymede's neighbor, Europa. Geologic activity on Europa has likely occurred in much more recent geologic time, with some studies suggesting it may be currently active today (Schmidt et al., 2011). From a biological perspective, this is of great interest as it may imply Europa could harbor life deep in its ocean, protected from the harsh radiation of Jupiter by its ice shell (Chyba and Phillips. 2001). This increased interest in the Galilean moons has driven two upcoming missions. NASA's *Europa Clipper* is a spacecraft scheduled to launch in the 2020s with cameras, spectrometers, and other instruments to produce high-resolution images of Europa's surface and determine its composition (Philips and Pappalardo, 2014). The European Space Agency (ESA) is also sending a spacecraft, *JUICE* (*JUpiter ICy moons Explorer*), to the Jupiter system and aims to spend at least three years making detailed studies of Ganymede, Callisto, and Europa after its proposed arrival in 2030 (Grasset et al., 2013). Anticipated data from these missions will promote a more advanced understanding of the Galilean system.

This dissertation leverages the well-established body of knowledge for Ganymede with several fascinating curiosities of Ganymede's surface deformation in response to persistent tidal forces to further motivate exploration of the tectonic history on a variety of scales. Chapter 2, submitted to Icarus and presently under revision following expert review (Cameron et al., 2018a;

Morphological Mapping of Ganymede: Investigating the Role of Strike-slip Tectonics in the evolution of terrain types) examines Ganymede's heavily fractured and morphologically distinct surface and considers how strike-slip faulting may be important to the structural development of observed features. To better understand the role of strike-slip tectonism in shaping this complex icy surface, detailed mapping analyses of nine sites is performed using *Galileo* and *Voyager* imagery, noting key examples of strike-slip morphologies where present. Sites of both light, grooved terrain (Nun Sulci, Dardanus Sulcus, Tiamat Sulcus, Uruk Sulcus, and Arbela Sulcus), and terrains that are transitional from dark to light terrains (Nippur and Philus Sulci, Byblus Sulcus, Anshar Sulcus, and the Transitional Terrain of Northern Marius Regio) are mapped. Abundant examples of strike-slip morphologies are found at every site, suggesting strike-slip tectonism is indeed important to Ganymede's evolutionary history. Moreover, incorporation of strike-slip tectonism with pre-existing observations of extensional behavior provides an improved, synoptic representation of Ganymede's history.

Chapter 3, also submitted to Icarus and presently under review (Cameron et al., 2018b; Tidal Stress Modeling of Ganymede: Strike-slip Tectonism and Coulomb Failure) revisits the detailed mapping results of Cameron et al. (2018a) and considers tidal stresses stemming from Ganymede's orbital interactions with Jupiter and the other Galilean satellites. The Coulomb criterion is used to investigate the roles of tidal stresses and assess the failure potential of individual fault segments. This criterion considers tractions that facilitate (tensile) and resist (compressive) slip on a fault, the shear tidal traction, the coefficient of friction of ice, and stress at depth due to the overburden pressure (Thatcher and Hill, 1991). Numerical modeling results suggest that under particular circumstances, diurnal and secular tidal stresses such as nonsynchronous rotation (NSR) may have been sufficient to induce shear failure and cause strike-slip faulting. The fault zone's predicted slip sense is compared to the inferred slip sense from the structural mapping efforts of Cameron et al. (2018a); compatible senses of slip among six of the nine regions are found. Results suggest that combined diurnal and NSR tidal stresses promote Coulomb failure within the shallow (< 2 km) icy lithosphere across much of Ganymede. Based on these results, we infer that while diurnal stresses alone are not enough to drive tectonism on Ganymede, nonsynchronous rotation may have assisted the formation and evolution of strike-slip structures.

Chapter 4, in preparation for submission to EPSL (Cameron et al., 2018c; Ganymede Then and Now: How Past Eccentricity may have Altered Tidally Driven Coulomb Failure) isolates the effects of diurnal tidal stresses and considers how Laplace-like resonances among Ganymede, Europa, and Io (Greenberg 1987; Malhotra, 1991; Showman and Malhotra, 1997) may have once led Ganymede to acquire an eccentricity as high as ~0.07 (presently e = 0.0013). While diurnal stresses at Ganymede today are quite small (less than 10 kPa), a previous period of high eccentricity may have permitted a significant diurnal tidal stress influence on faulting during a past period of active tectonism, with stresses increasing by at least an order of magnitude. Results of Coulomb failure along three fault zones at Dardanus Sulcus, Tiamat Sulcus, and Nun Sulci are re-examined. Findings from Cameron et al. (2018b) are supported, showing that Coulomb failure is not expected along any of the three shear zones when considering present-day (low) eccentricity for diurnal stresses only. Coulomb failure is predicted, however, for a past, high eccentricity case, although in isolated periods during an orbit and limited to very shallow depths (< 250 m).

The findings of this dissertation highlight the need to consider the full range of Ganymede's evolution through time (with ancient terrain dating to > 4 Gyr) when describing a complex tectonic history. While Ganymede may not currently be geologically active, satellite images provide a rich and diverse surface morphology indicative of a past period of large-scale tectonics. Additionally, detailed mapping from this and previous studies reveals smaller-scale processes, such as strike-slip faulting, that may have helped shaped the terrain. The source of tectonics on Ganymede is largely driven by tidal forces from its interaction with Jupiter and the neighboring Galilean satellites. These tidal contributions varied in magnitude over time as the dynamics of the Galilean system evolved. Effects of a global subsurface ocean allow for additional stresses, and, at least on Europa, may have greater implications for the presence of life beyond Earth.

Specifically, this work is directly relevant to the objectives of NASA's Outer Planets Research Program in "Enhancing the scientific return from the … Galileo and Voyager… missions by continuing the analysis of their respective data sets through broadening scientific participation; Improving our understanding of the evolution of the outer Solar System, including the giant planets (or) their satellites…" When all three studies presented here are considered

together, insight may be gained into past and modern history of Ganymede, which may prove especially useful given the renewed interest in future missions to Jupiter and its Galilean moons with the recent selection of the *JUpiter ICy moons Explorer* (*JUICE*) as ESA's next mission.

CHAPTER 2. MORPHOLOGICAL MAPPING OF GANYMEDE: INVESTIGATING THE ROLE OF STRIKE-SLIP TECTONICS IN THE EVOLUTION OF TERRAIN TYPES

Marissa E. Cameron[a*], Bridget R. Smith-Konter[a], Liliane Burkhard[a], Geoffrey C. Collins[b], Fiona Seifert[c], and Robert T. Pappalardo[d]

[a] *Department of Geology and Geophysics, University of Hawai'i at Mānoa, Honolulu, HI 96822*

[b] *Physics and Astronomy Department, Wheaton College, Norton, MA, 02766*

[c] *Atmospheric, Ocean and Space Sciences Department, University of Michigan, Ann Arbor, MI 48109*

[d] *Jet Propulsion Laboratory, California Institute of Technology, Pasadena, CA 91109*

* Corresponding author. Address: Department of Geology and Geophysics, 1680 East-West Rd., University of Hawai'i at Mānoa, Honolulu, HI 96822, email: mecamero@hawaii.edu

Abstract

The heavily fractured surface of Ganymede displays many morphologically distinctive regions of inferred distributed shear and strike-slip faulting that may be important to the structural development of its surface. To better understand the role of strike-slip tectonism in shaping this complex icy surface, detailed mapping is performed at nine sites using *Galileo* and *Voyager* imagery, noting key examples of strike-slip morphologies where present. These four morphological indicators are: *en echelon* structures, strike-slip duplexes, laterally offset pre-existing features, and possible strained craters. Sites mapped consist of both light, grooved terrain (Nun Sulci, Dardanus Sulcus, Tiamat Sulcus, Uruk Sulcus, and Arbela Sulcus), and terrains that are transitional from dark to light terrains (Nippur and Philus Sulci, Byblus Sulcus, Anshar Sulcus, and the Transitional Terrain of Northern Marius Regio). At least one, if not more, of the four strike-slip morphological indicators are observed at every site, suggesting strike-slip tectonism is indeed important to Ganymede's evolutionary history. Byblus Sulcus is the only mapped site where the presence of strike-slip indicators is limited to only a few *en echelon* structures; every other mapped site displays examples of at least two types, with Arbela Sulcus containing candidate examples of all four. In addition, quantification of morphological characteristics suggests related rotation between sites, as evidenced by the predominant NW/SE trend of mapped features within the light terrain present in five different sites (Nun, Tiamat, Uruk, Nippur/Philus, Byblus, and Anshar Sulcus). Moreover, incorporation of strike-slip tectonism with previous observations of extensional behavior provides an improved, synoptic representation of Ganymede's tectonic history.

Submitted to Icarus and currently in revision.

1. Introduction

Ganymede is the largest of Jupiter's four Galilean moons (diameter of ~5270 km) and has a tectonically active past (Shoemaker et al., 1982; Schenk et al., 2001; Collins et al., 2013). The twin *Voyager 1* and *2* spacecraft imaged the Jupiter system in 1979 (Smith et al., 1979a, b), followed by the *Galileo* space probe that orbited Jupiter between 1995 and 2003 (Carr et al., 1995). In addition to high-resolution imagery, magnetic field data from *Galileo* provided evidence of an induced magnetic field, consistent with the presence of a subsurface liquid water ocean (Kivelson et al., 2002), as well as an intrinsic dipole field that may be the product of dynamo action (Kivelson et al., 1997). The exact thicknesses and depths of the differentiated layers of Ganymede's interior are uncertain, but the outer ice shell is most likely ~100 km thick (Spohn and Schubert, 2003; Schubert et al., 2004). Imagery from *Galileo* flybys revealed Ganymede's surface to be extensively fractured and composed of distinct terrains, with high-resolution imagery showing indications of both normal and strike-slip structures (Collins et al., 1998b; Pappalardo et al., 1998; Patel et al., 1999; DeRemer and Pappalardo, 2003; Pappalardo et al., 2004; Pappalardo and Collins, 2005).

The evolution of Ganymede's surface has been complex, and while most investigations so far have focused on the mechanisms for extensional tectonism (Collins et al., 1998b; Pappalardo et al., 2004; Pizzi et al., 2017), a global study of the nature and role of strike-slip tectonism using *Galileo* images is lacking. *Voyager* images of Ganymede (at best ~500 m/pixel) have been interpreted as indicating that strike-slip faulting and distributed shear deformation occurred, notably based on the sigmoidal shapes of some grooved terrain sets and candidate strike-slip offsets along major fault zones (Smith et al., 1979; Lucchitta, 1980; Murchie and Head, 1988; Pappalardo, 1994). However, the role of this process in shaping grooved terrain has been highly uncertain, and the evidence for major strike-slip fault zones was debated at the time (Schenk and McKinnon, 1987; Murchie and Head, 1988). Indeed, prior to *Galileo* imaging, it was questioned whether strike-slip faults occurred at all on Ganymede and most planetary surfaces (Golombek, 1982). In isolated *Galileo* images at high resolutions (commonly 10s m/pixel), however, strike-slip tectonism and components of distributed shear were subsequently inferred along some faults and faulted regions, helping to shape the present-day perspective of tectonic styles that may have

once contributed to Ganymede's diverse surface (Collins et al., 1998b; Pappalardo et al., 1998; Patel et al., 1999; Prockter et al., 2000; Head et al., 2002; DeRemer and Pappalardo, 2003; Pappalardo et al., 2004; Pappalardo and Collins, 2005).

Several first-order questions remain about the role of strike-slip tectonism on Ganymede: How prevalent is strike-slip faulting? What role do strike-slip structures play in the transition between prominent terrain types? If bright terrain is due to modification of dark terrain, do strike-slip processes promote this modification by breaking up the ancient dark surface to expose high albedo material? How can features related to strike-slip tectonism and features related to extension be distinguished? In this study, we aim to advance the knowledge of the structural and evolutionary history of Ganymede by documenting strike-slip faulting processes based on geological inferences, which will ultimately be synthesized with models of failure mechanics.

In this paper, the types and distribution of strike-slip features on Ganymede based on *Galileo* images targeted at candidate sites of shear deformation identified using *Voyager* imagery are identified and carefully mapped. The objectives of this mapping are to understand the range of morphologies and morphometries, and to infer the possible manifestations of strike-slip faulting. Section 2 provides a brief background of Ganymede's geologic history, including the two main types of geologic terrains that dominate the surface. In Section 3 reviews the kinematics of strike-slip tectonism and introduce key structural indicators of strike-slip faulting (*en echelon* structures, strike-slip duplexes, offset features, and strained craters). In Section 4 documents the image and mapping processes. In Section 5 presents observations and interpretations of the morphological mapping of nine target sites where strike-slip tectonism is inferred: Uruk Sulcus, Tiamat Sulcus, Nun Sulci, and Dardanus Sulcus, Transitional Terrain, Byblus Sulcus, Anshar Sulcus, Arbela Sulcus, and Nippur/Philus Sulci. Finally, in Sections 6 and 7 results from regional to global perspectives are discussed and synthesized, and include an analysis of the role of strike-slip tectonism in modifying dark materials. The ultimate goal of this work is to firmly establish observations of strike-slip behavior in support of future detailed modeling of tidal and secular stresses that may have driven Ganymede tectonics.

2. Background

2.1. Geologic Setting

Global images of Ganymede (Figure 2.1a, b) reveal two distinct terrain types (Figure 2.1b, c): an older, heavily cratered dark terrain and a younger, typically grooved light terrain (Collins et al., 2013). Ganymede's history, inferred from imagery, can be divided into three intervals of relative age: (1) formation of its dark crust during the Nicholsonian period, (2) widespread tectonic activity and rifting of crust during the Harpagian period, and (3) subsequent cratering during the Gilgameshian period (Collins et al., 2013). Dark terrain was primarily emplaced during the Nicholsonian period but some appears to be modified during the Harpagian period (Collins et al., 2013). Light terrain consists of relatively high- to moderate-albedo, tectonically deformed material from the middle-aged Harpagian period.

2.1.1. Dark Terrain

Dark terrain (Figure 2.1c, left) covers about one-third of the moon and is characterized by an ancient, heavily cratered appearance (Shoemaker et al., 1982; Murchie et al., 1986, 1989; Neukum, 1997; Neukum et al., 1998; Prockter et al., 1998; Zahnle et al., 2003; Schenk et al., 2004). Much of the dark terrain is crosscut by systems of ~10 km wide furrows inferred to be remnants of large multi-ring structures (McKinnon and Melosh; 1980; Cassachia and Strom, 1984; Moore et al., 1998, 2001; Prockter et al., 2000; Pappalardo et al., 2004). Dark terrain is estimated to date from > 4 Gyr based on measured crater densities (Zahnle et al., 2003). The terrain is inferred to consist of a thin dark regolith deposit that is heterogeneous in albedo at the scale of meters (Spencer, 1987a,b) overlying brighter, icy material that has been modified by surface processes (Cassachia and Strom, 1984; Croft and Strom, 1985; Croft and Goudreau, 1987; Allison and Clifford, 1987; Figueredo et al., 1999; Moore et al., 1999; Prockter et al., 2000). The darkest deposits are correlated with local topographic lows like crater floors and troughs, whereas brighter material is typically found along ridges and other topographic highs (Oberst et al., 1999). As dark terrain shows areas of tectonic deformation related to furrow formation, dark terrain tectonism is considered a potential precursor to grooved terrain (Patel et al., 1999; Pappalardo et al., 2004 and references within). Clear evidence of both extension and

strike-slip tectonism is far more prevalent in light terrain than in dark terrain.

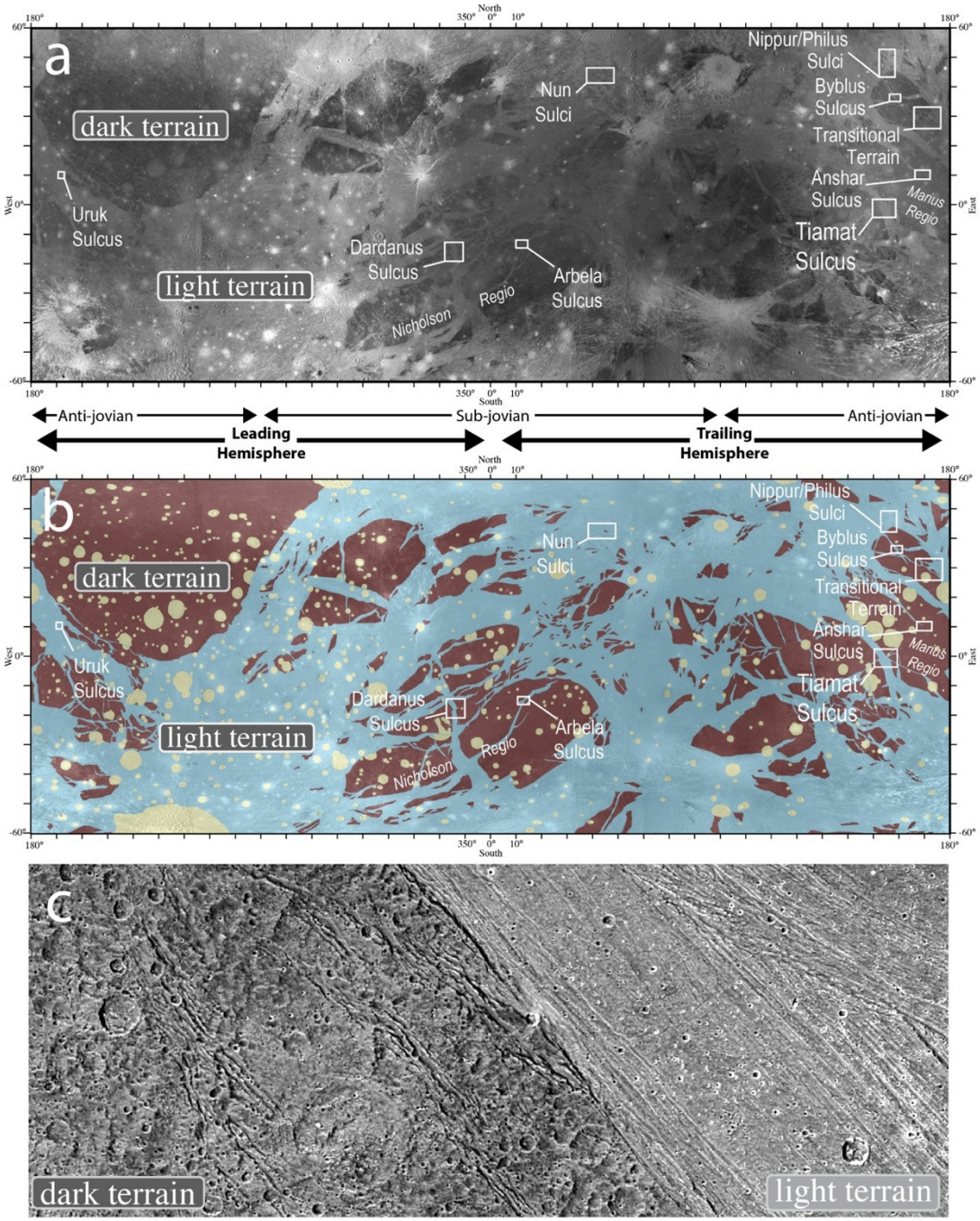

Figure 2.1: Ganymede map and terrain types: (a) Ganymede global mosaic (0° – 360° E; 60°S - 60°N) in Mercator projection. Examples of dark and light terrain are labeled; labeled boxes denote sites mapped in this study. Anti-Jovian, sub-Jovian, and leading/trailing hemispheres are labeled; (b) Ganymede global geologic map (modified from Collins et al., 2013) overlaying the global image mosaic. The domains are divided into: dark terrain (brown), light terrain (blue), and impact features (yellow); (c) Representative example of dark terrain of Nicholson Region (left) at the boundary of light (grooved) terrain (right) of Harpagia Sulcus.

2.1.2. Light (grooved) Terrain

Light terrain (Figure 2.1c, right) covers the remaining two-thirds of Ganymede's surface and is characterized by a subparallel ridge and trough system that cross-cuts the older, dark terrain (Murchie et al., 1986; Pappalardo et al., 1998; Prockter et al., 2000; Collins, 2009). Crater density within the light terrain is 2 to 10 times less than in dark terrain, and light terrain is thus inferred to have been emplaced between 400 Myr and 4 Gyr ago. The large range in time reflects uncertainty in the impact flux (Zahnle et al., 1998; Neukum et al., 1998; Zahnle et al., 2003). Morphological evidence suggests that light terrain may be tectonically modified pre-existing terrain (Head et al., 1998; Pappalardo et al., 2004). While direct evidence of cryovolcanism on Ganymede is sparse (Pappalardo et al., 1998; Prockter et al., 2000; Pappalardo et al., 2004, Bland and McKinnon, in press), the addition of cryovolcanic deposits may have helped brighten the dark terrain, for example, by flooding of graben (Cassachia and Strom, 1984; Croft and Strom, 1985; Croft and Goudreau, 1987; Allison and Clifford, 1987; Figueredo et al., 1999; Schenk et al., 2001). For the purposes of this study, light terrain is further divided into three major categories introduced by Collins et al. (2013): light irregular material; light subdued material; and light grooved material. Light irregular material displays a mixture of smooth surfaces and grooves, but the grooves have irregular orientations and spacing. Light subdued materials are characterized by smooth surfaces and faint lineaments; the lineaments generally have similar spacing and orientations in each area and are inferred to be representative of early stages of grooved terrain formation. Light grooved materials are dominated by similarly spaced and oriented areas of closely packed troughs and lineaments, likely formed through modification and deformation of pre-existing materials, such as the light subdued material or dark terrain (Collins et al., 2013).

2.2 Tectonic Setting

Previous studies focused on the relevance of extension in grooved terrain formation. *Voyager* images initially suggested that most grooves are extensional tectonic structures (Shoemaker et al., 1982), and *Galileo* images later supported this interpretation (Belton et al., 1996, Pappalardo et al., 1998; Dombard and McKinnon, 2001; Bland and Showman, 2007). Various styles of extensional tectonism have been inferred on Ganymede, including horst-and-graben grooved

terrain morphology and tilt-block-style normal faulting (Pappalardo et al., 1998, 2004 and references therein). Both Uruk Sulcus and Philus Sulcus display morphologies resembling flat-topped horst ridges and flat-floored grabens (Collins et al., 1998c), bounded by normal faults that dip in opposing directions (Davis and Reynolds, 1996). Moreover, Uruk Sulcus also displays ridges that appear triangular to rounded in cross-section, a morphology that is far more common on Ganymede and generally attributed to tilt-block, or domino style faulting (Pappalardo et al., 1998, Collins et al., 1998b), which occurs where prominent fault planes dip in the same direction (Davis and Reynolds, 1996). Prior to *Galileo*-based observations of Uruk Sulcus (Pappalardo et al., 1998), tilt-block style faulting had not been predicted to occur on Ganymede because of the high degree of extension necessary to create them (>10% of extensional strain (Wernicke and Burchfiel, 1982)) compared to horst-and-graben style faulting (< 10% extensional strain with the assumption that grooves are individual graben, as predicted by Golombek (1982)). Moreover, higher crater density in areas that show horst-and-graben morphology suggests that the terrain is older than less cratered tilt-block-style areas, and suggests faulting style may have changed over time within Uruk Sulcus (Pappalardo et al., 1998). By examining the grooves as extensional features, orientations of the stresses that formed them may be inferred, and the mechanisms of formation driven by different stressing mechanisms may be considered.

In addition, many observations of structures indicative of strike-slip processes (as discussed next) suggest that a component of horizontal shear may have contributed to shaping grooved terrain (Lucchitta et al., 1980; Murchie and Head, 1988). Using *Voyager* data (kms/pixel resolution), Murchie and Head (1988) suggested that morphologic evidence for shear zones, such as the offset of distinctive structures, exists in both the sub- and anti-Jovian hemispheres of Ganymede; however, the lack of high-resolution coverage prevented conclusive results at the time. While subsequent *Galileo* data provide much higher resolution imagery (albeit limited coverage), very few studies have followed with a thorough inspection of strike-slip tectonism and consideration of the role of horizontal shear in Ganymede's tectonic evolution (Pappalardo et al., 1998; Prockter et al., 2000). Moreover, many questions remain regarding the relevance of strike-slip faulting on Ganymede and its link to terrain types and terrain modification.

3. Four morphological indicators of strike-slip faulting

Strike-slip faulting, also known as wrench faulting, occurs as fault walls shift past one another laterally. A series of structures (Figure 2.2) may develop along a narrow shear zone where strike-slip occurs along a steeply dipping fault overlain by weakly consolidated material (Tchalenko and Ambraseys, 1970; Wilcox et al., 1973; Pollard et al., 1982; Naylor et al., 1986), which may be relevant to icy satellite tectonics (Pappalardo and Greeley, 1995). Transpression and transtension deformation involves strike-slip that is combined with either contraction or extension, respectively (Dewey et al., 1998). Strike-slip faulting can produce patterns of intersecting and/or subparallel faults and fault-bounded structures (Pollard et al., 1982; Naylor et al., 1986; Woodcock and Fisher, 1986; Pappalardo and Greeley, 1995) that are potentially relevant to the formation of the ridge and trough terrain on Ganymede.

When modeling fault mechanics, a complete quantitative analysis of faulting must specify several details, including fault geometry, boundary and initial conditions, and assumed constitutive stress-strain relationships (Segall and Pollard, 1980). Unfortunately, even in cross section, real fault geometries are complex. In addition, boundary and initial conditions for planetary surfaces are often based on inferences made from sparse data regarding materials with poorly known of unknown rheologies. Given these constraints, Earth analogs (including field observations), laboratory experiments, and an assumed linear elastic ice rheology are used to infer patterns and causes of strike-slip faulting of Ganymede's surface. Several types of diagnostic structures that can evolve as the slip along a basement fault increases are examined: *en echelon* faults, strike-slip duplexes, and offset features (Figure 2.2). Strained craters can also serve as useful markers for strike-slip tectonism (Pappalardo and Collins, 2005).

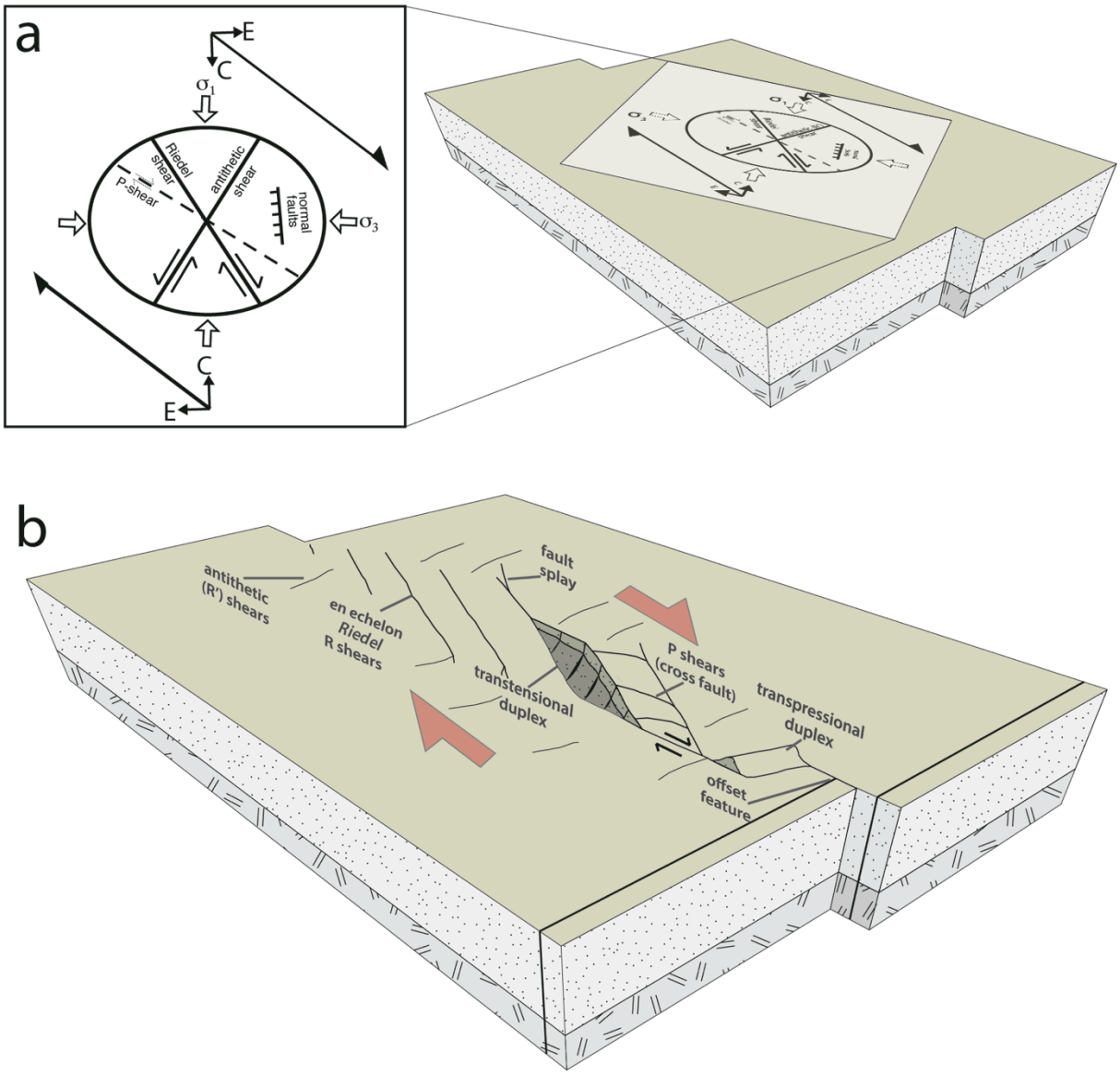

Figure 2.2: Strike-slip morphology cross section: (a) Diagrammatic strain ellipse and associated structures predicted from dextral simple shear after Reading (1980) and Harding (1974), projected onto a perspective view surface. Open white arrows represent the corresponding principal stress directions. The maximum compressive stress (σ_1) and minimum compressive stress (σ_3) can be visualized as indicating the ‘‘compression axis’’ C and the ‘‘extension axis’’ E, respectively. Half-arrows indicate the inferred direction of simple shear, either dextral or sinistral; (b) Summary of morphological predictions of strike-slip faulting (modified from Pappalardo and Greeley, 1995). Features labeled are distinctive large-scale characteristics of strike-slip faulting that can be identified in spacecraft images, and which are examined in this study.

3.1. En echelon structures

En echelon structures (Figure 2.2b and 2.3) are a series of sub-parallel structures restricted to a band that is narrow relative to its length, and separated by systematic offsets (or step-overs), used synonymously with Riedel (R) and antithetic (R') shears in this study. On Earth, *en echelon* structures appear at a broad variety of scales in numerous materials, from granite to soil to ice, and several mechanisms may explain their formation. For example, Pollard et al. (1982) argue that *en echelon* fractures grow from a dilatant parent crack that encounters a region in which the principal stresses have rotated about an axis parallel to the direction of fracture propagation. Alternatively, shear stresses acting parallel to a parent crack front may allow for growth of incipient *en echelon* cracks (Wilcox, et al., 1973; Pollard et al., 1982; Thomas and Pollard, 1993). Moreover, experimental models suggest that with low levels of strain, net simple shear causes a set of small faults (Figure 2.2), or R *en echelon* shears, to form (Tchalenko, 1970). R shears strike at a low angle to the basement fault and are characterized as right-stepping or left-stepping by determining if one must step right or left to reach the next segment when looking along strike (Tchalenko, 1970; Segall and Pollard, 1980). Right-stepping transtensional *en echelon* fault segments indicate left-lateral strike-slip, while left-stepping transtensional fault segments indicate right-lateral strike-slip; transpressional *en echelon* structures will step in the opposite sense (Kingma, 1958; Reading, 1980; Woodcock and Fischer, 1988). With increasing angle to the basement fault, conjugate faults with an opposite sense of shear (R') may also form (Tchalenko, 1970; Naylor et al., 1986). Faults may produce P shears that are roughly symmetrical to the R shears (with respect to the overall slip direction) and act to connect the R shears, ultimately linking into through-going faults (Naylor et al., 1986; Woodcock and Fischer, 1988).

En echelon structures are not limited to Earth, with evidence for them found on Venus (Basilevsky et al., 1986), Mars (Vetterlin and Roberts, 2003), Enceladus (Martin, 2016), Europa (Michalski et al., 2002, Kattenhorn, 2002; Kattenhorn, 2004; Hoyer et al., 2014), and Ganymede (DeRemer and Pappalardo, 2003). On Ganymede, examples of *en echelon* structures (Figure 2.3) are common within the grooved terrain (e.g., Uruk Sulcus), but they also occur within the dark terrain (e.g., Anshar Sulcus) (Collins et al., 1998c; DeRemer and Pappalardo, 2003; Pappalardo et al., 2004). *En echelon* structures display a variety of widths and lengths, and mapped example

zones on Ganymede range in length from several to tens of kilometers to hundreds of kilometers. Morphological observations of Ganymede's *en echelon* structures suggest a similar progression from R shears to complex fault zones with continued slip, as predicted by experimental models (Naylor et al., 1986; DeRemer and Pappalardo, 2003). This progression from simple to more complex shear zones may be related to an increase in the amount of slip (DeRemer and Pappalardo, 2003); moreover, shear zones in dark terrain might evolve into bright *en echelon* swaths as slip increases (Prockter et al., 2000; DeRemer and Pappalardo, 2003).

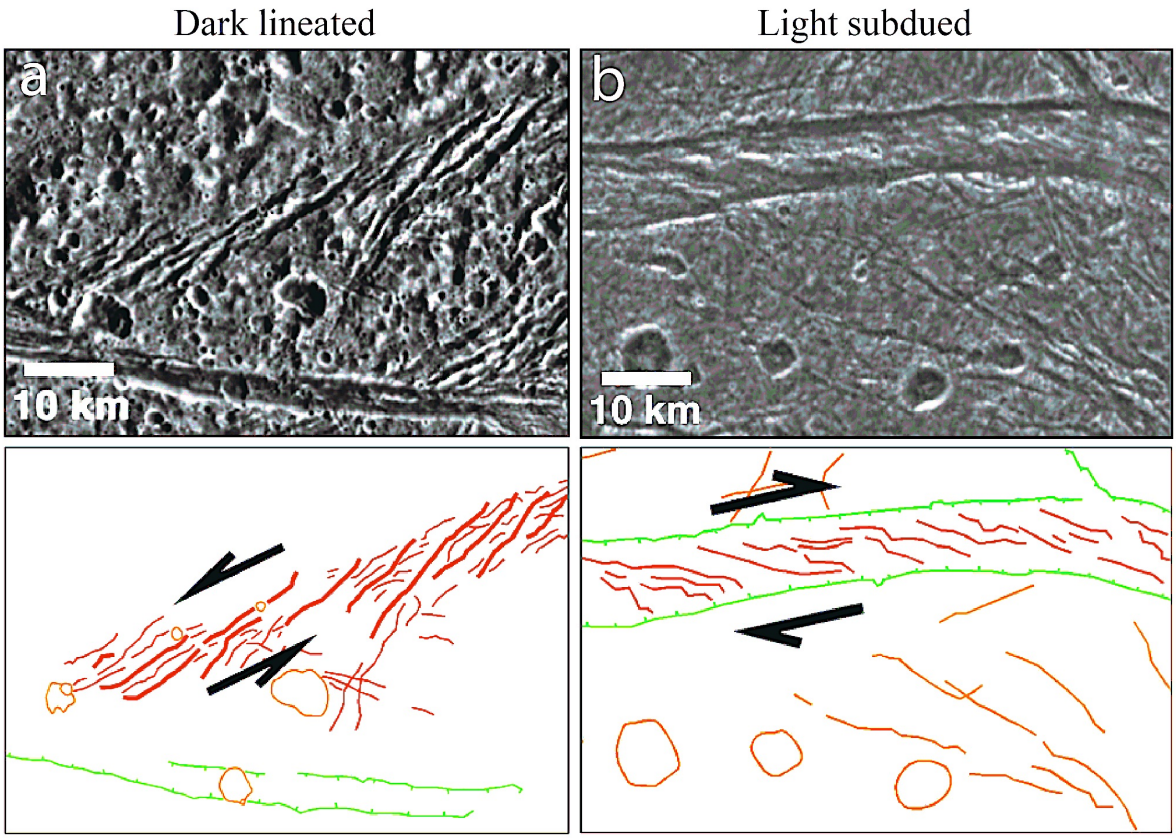

Figure 2.3: Examples of *en echelon* structures on Ganymede, with simple corresponding sketch maps and inferred shear sense, after DeRemer and Pappalardo (2003). (a) Isolated *en echelon* structures within the dark lineated terrain of Anshar Sulcus (162°E, 18°N); (b) An *en echelon* swath in the light subdued material found within Transitional Terrain (173°E, 32°N). Arrows indicate inferred shear sense assuming a transtensional origin, where bold red lines are features of interests, thin red lines are craters and features outside of the relevant zone, and green lines are scarps (ticks point downslope).

3.2. Strike-slip duplexes

Strike-slip duplexes (Figure 2.4) can form where a strike-slip fault bends and creates a sigmoidal or spindle-shaped fault-bounded area (Naylor et al., 1986; Woodcock and Fischer, 1988; Pappalardo and Greeley, 1995; Prockter et al., 2000; DeRemer and Pappalardo, 2003). A transpressional duplex can form at restraining bends or steps, while an extensional duplex can form at releasing bends or steps. In addition, smaller *en echelon* faults can dissect the duplex interior (Woodcock and Fisher, 1986).

Strike-slip duplexes have been interpreted to exist on Europa, for example, along the ~1500 km long Agenor Linea where a ~50 km contractional duplex is inferred to have formed at a restraining bend (Prockter et al., 2000). On Ganymede, sets of faults resembling strike-slip duplexes are prevalent within the light terrain (e.g., Uruk Sulcus, Nun Sulci; Figure 2.4c), but also can occur in dark terrain (e.g., Transitional Terrain; Figure 2.4a, b). Duplexes within light terrain represent mostly extensional regimes; for example, an inferred extensional duplex at Uruk Sulcus suggests transtension (Collins et al., 1998c; Pappalardo et al., 1998). Far fewer examples suggest a contractional regime, such as the inferred contractional duplex at Nun Sulci.

Previous work by Pappalardo and DeRemer (2003) suggests duplex structures on Ganymede can be categorized based on fracture density, continuity of bounding faults, and the presence of internal structure. Pappalardo and DeRemer (2003) consider three classes of duplex structures: (1) discontinuous fractures, (2) lensoid bounding structures, and (3) lensoid duplexes with subparallel internal structure. Discontinuous fractures suggesting lensoid shape (class 1, Figure 2.4a) occur in dark terrain and are defined by discontinuous bounding structures of low fracture density, where no identifiable duplex-related internal structure exists. Lensoid bounding structures (class 2, Figure 2.4b) are also found in dark terrain and have fractures of great enough continuity and density as to define continuous lensoid-shaped bounding structures. If these areas have any identifiable duplex related internal structure, the structure is not organized. Examples of duplex structure class 1 and 2 may be observed in the Transitional Terrain (Section 5.2). Lastly, lensoid duplexes with subparallel internal structure (class 3, Figure 2.4c), recognized in grooved terrain, exhibit continuous bounding structures and an organized, subparallel group of internal structures. An example of duplex structure 3 is inferred in Uruk Sulcus (Section 5.1). These morphological transitions in duplex classes might form an evolutionary sequence, perhaps

occurring during the transition from dark to grooved terrain, in which originally discontinuous structures link together, and then their interiors overlap to form fault duplexes (DeRemer and Pappalardo, 2003).

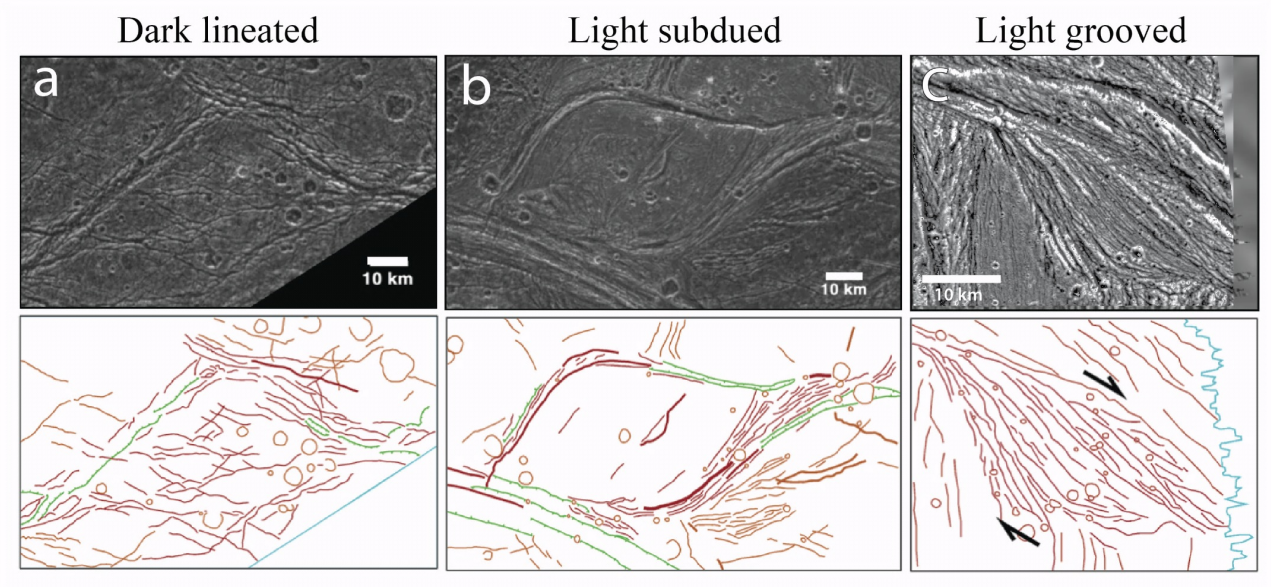

Figure 2.4: Examples of fault duplexes and duplex-like structures on Ganymede, with corresponding sketch maps, after DeRemer and Pappalardo (2003). (a) Dark lineated terrain showing discontinuous structures (class 1) suggesting a lensoid shape in Transitional Terrain (173°E, 32°N); (b) Light subdued terrain showing lensoid bounding structures (class 2) in Transitional Terrain; (c) Light grooved terrain showing a lensoid with a subparallel internal structure (class 3) in Uruk Sulcus (199°E, 0.8°N). Arrows indicate inferred shear sense assuming a transtensional origin, bold red lines are features of interests, thin red lines are craters and features outside of the relevant zone, green lines are scarps (ticks point downslope), and blue lines denote image boundaries.

3.3. Offset features

Offset of pre-existing structures (Figure 2.5) can indicate strike-slip faulting, even where other strike-slip features cannot be identified, for example, if available image resolution is limiting. Strike-slip offset can readily be observed on Earth, for example, along the San Andreas fault, a ~1300 km long right-lateral strike-slip fault where some markers suggest ~175 km of offset has occurred in the last 12 Ma (Graymer et al., 2002). Strike-slip offset is also commonly inferred on Europa, such as the ~800 km long Astypalaea Linea which exhibits ~40 km of right-lateral offset (Hoppa et al., 1999). On Ganymede, discernible fault zone offsets are inferred along both Dardanus and Tiamat Sulcus (Figure 2.5), where right-lateral strike-slip is the likely explanation for the apparent offsets of preexisting features, of ~45 and ~20 km respectively,

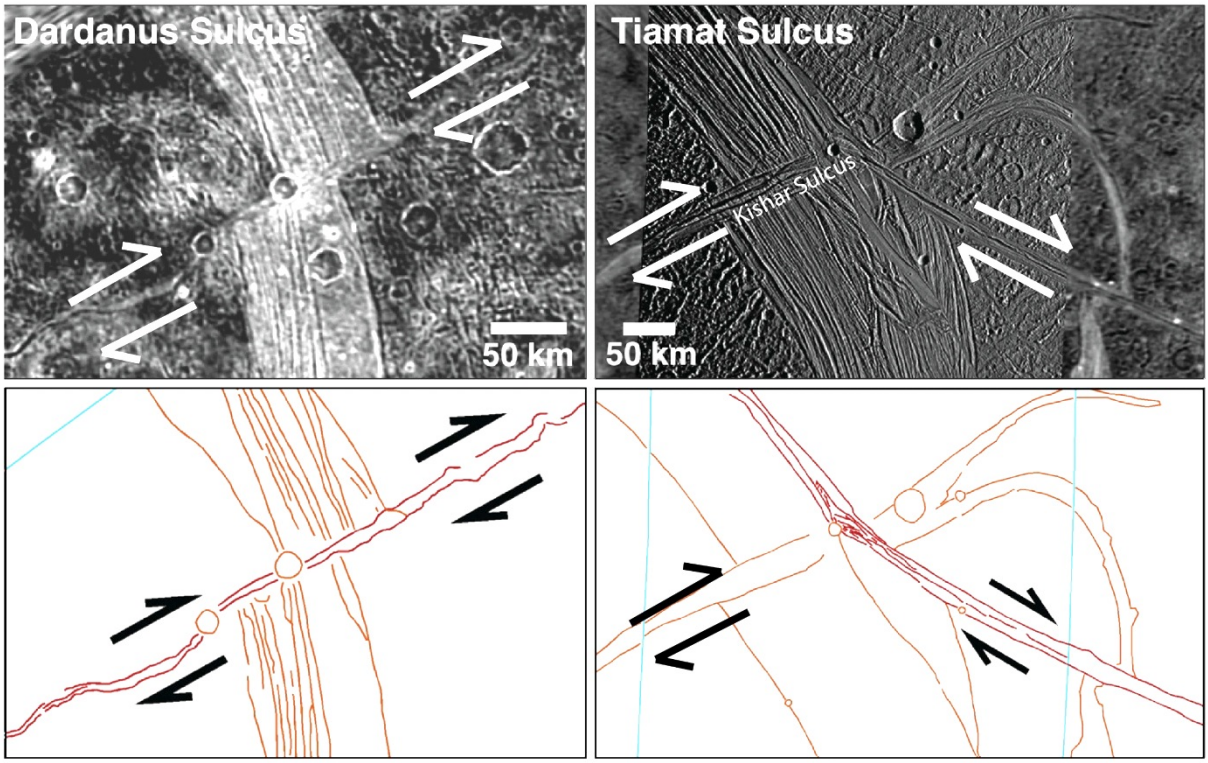

Figure 2.5: Examples of offset features at Ganymede's Dardanus Sulcus (342°E, 18°S) and Tiamat Sulcus (151°E, 0°S), with corresponding sketch maps and inferred shear sense. Arrows indicate inferred shear sense assuming a transtensional origin, bold red lines are features of interests, and blue lines denote image boundaries.

3.4. Strained Craters

Strained craters (Figure 2.6) can serve as natural strain markers on tectonically deformed planets. On Earth, markers of known initial shape, such as initially spheroidal sedimentary grains, or ooids, are commonly used to infer strain (Ramsay, 1967; Means, 1976; Ramsay and Huber, 1983). In other planetary environments, most craters originate as near-circular structures formed by impactors which strike a surface at >10° from the horizontal (Gault and Wedekind, 1978). Studies of the geometry of deformed craters have helped infer crustal shortening along reverse faults on Mercury (Strom et al., 1975; Dzurisin, 1978), and the ellipticity of Martian craters has been used to infer strain across them (Thomas and Allemand, 1993; Golombek et al., 1996).

Very few strained craters were recognized in *Voyager* images of Ganymede (Shoemaker et al., 1982), but relatively high-resolution *Galileo* images reveal several strained craters tens of

kilometers in diameter. These deformed craters have retained identifiable rim segments along a considerable portion of their circumference, but are transected by sets of subparallel ridges and troughs oriented roughly orthogonal to the long axis of the crater, suggesting that initially circular craters have been extended (Pappalardo and Collins, 2005). Pappalardo and Collins (2005) used two methods (Figure 2.6) for estimating crater elongation. (1) For craters transected by a narrow zone of ridge and trough terrain resulting in two relatively undeformed, arc-shaped crater rim segments (split craters), such as Saltu crater in Arbela Sulcus (Figure 2.6a; Section 5), two best-fit circles can be fit to the undeformed rim arc remnants, and the line connecting the centers of the two best-fit circles is the slip vector accommodated by the narrow zone of deformation (Figure 2.6a). (2) For craters that are intensely deformed by ridge and trough terrain distributed across the entire crater, the deformed crater rim roughly approximates an ellipse, such as the unnamed crater in Marius Regio near Anshar Sulcus (Figure 2.6b; Section 5) or Nefertum crater in the Nun Sulci region (Figure 2.8). Locations along the deformed rim can be digitized to fit a best-fit ellipse (Figure 2.6b). Both of these methods can be used to determine displacement by simple extension and displacement by simple shear accommodated by the ridge and trough terrain. With this consideration, Pappalardo and Collins (2005) estimate elongation amounts ranging from 5 to 50% for five studied craters (Saltu, Nefertum, Erichthonius, and two unnamed craters) on Ganymede.

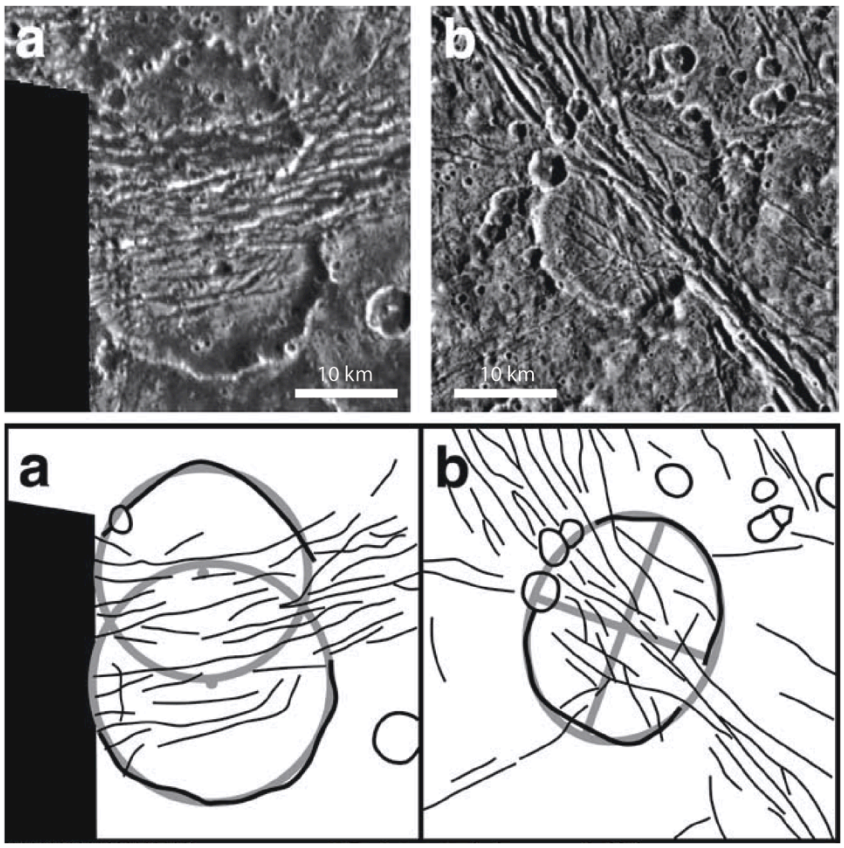

Figure 2.6: Images and sketch maps of example strained craters with representative troughs and smaller craters from Pappalardo and Collins (2005): (a) Saltu, within dark terrain of Nicholson Regio (7.3°E, 14°S); shown in gray are the circles fit to each rim segment and their corresponding centers; (b) An unnamed crater in dark terrain of Marius Regio, near Anshar Sulcus (162°E, 18°N); shown in gray are the best-fit ellipses and their corresponding major and minor axes.

4. Image processing, digitization of morphological structures, and structural analyses

Between 1996 and 2000, the *Galileo* spacecraft made six close encounters with Ganymede allowing for acquisition of high-resolution images with the Solid State Imaging (SSI) camera (Patterson et al., 2010). Tables 2.1 and 2.2 provide details related to *Galileo* geospatial data, image resolution, and nomenclature; additional *Galileo* orbital information for Ganymede remote sensing data are provided by Schenk (2010) and Bagenal et al. (2004). Although high-resolution coverage of Ganymede is sparse (Carr et al., 1995), *Voyager* data provides additional lower resolution coverage (Smith et al., 1979a,b; Shoemaker et al., 1982; McKinnon and Parmentier, 1986). Becker et al. (2001) created global image mosaics of Ganymede's surface using the best data from the *Galileo* and *Voyager* 1 and 2 missions. Both the lighting and viewing geometries

of the images used in the mosaics vary greatly, and may hinder proper characterization of terrains.

Each *Galileo* mosaic was first processed in U.S. Geological Survey ISIS 3 (Integrated Software for Imagers and Spectrometers, cf. Keszthelyi et al; 2013, 2014), then imported into ArcMap Geographic Information System (GIS) software in simple cylindrical map projection, and digitized at a standard scale ratio appropriate for each image set (ranging from 1:250 k and 1:1 M, depending on the data set). For each mosaic, imagery was first inspected for trough-like structures, which were then digitally recorded as lines on the map; ridges were also mapped in some locations and notated accordingly. Where necessary, mapped features were extended into the surrounding low-resolution imagery, and some features were mapped directly on the low-resolution images in separate GIS layers. For consistency in mapping, a reference circle appropriate to the resolution of the image was drawn for each image set, representing the smallest size structure (typically a crater) to be digitized. A stippled pattern was adopted for digitizing furrows.

All image sets and features were mapped uniformly within the varying resolution limits, and special attention was focused on identification of strike-slip indicators described in Section 3. Where identified, these structures received text labels. An ArcGIS map package created in ArcMap 10.1 containing the corresponding high-resolution imagery of each site and presence of strike-slip indicators is available for download (Cameron et al., 2018d, Mendeley dataset). While terrestrial geological map units are material units independent of structure (ACSN, 1961), exceptions are generally made in planetary mapping owing to the difficulty of using a strict lithologic definition of units when limited to remote sensing. Wilhelms (1972, 1990) outlines a process in which a broader suite of units may be defined on the basis of crater density, surface morphology, superposition relations, albedo contrasts, and other observable features (see also Head et al., 1978). The use of structure to characterize geological units, even in the qualified manner described above, can be controversial (Hansen, 2000). For the purpose of this study, "domains" are instead defined as tectonic divisions of similar and consistent morphology, reflectance, and density of any superposed craters. Where possible, the terrain types described in Section 2.1 (dark terrain, light subdued, light irregular, and light grooved) are used as a marker for assigning color types, with each terrain type receiving a unique color. Relative ages within

light terrain types are indicated by varying shades of a given color (darker with inferred age) as demonstrated in Figure 2.7. Please note the relationship between shading and relative age only applies within a single terrain type (light or dark), and is only applicable within any given individual mapping area, where contiguous high-resolution *Galileo* images exist. These color schemes were adopted to facilitate comparisons among mapped sites at a global scale.

Table 2.1: Camera and lighting geometry of *Galileo* imagery. Between 1996 and 2000, the *Galileo* spacecraft made six close encounters with Ganymede (orbits G1, G2, G7, G8, G28, and G29), allowing for acquisition of high-resolution images with the Solid State Imaging (SSI) camera (*Patterson et al*., 2010).

Site name	Observation ID	Emission angle (°)	Incidence angle (°)	Average resolution (m/pixel)
Nun Sulci	G7GSNUNSUL01	56.95-60.47	48.64-51.20	170
Dardanus Sulcus	29GSDARDAN01	19.58-30.912	20.13-31.61	2000
Tiamat Sulcus	G8GSTIAMAT01	21.21	84.51	500
Uruk Sulcus	G1GSURUSUL01	21.35-23.30	12.74-14.20	40-75
Arbela Sulcus	28GSARBELA02	14.19-17.00	31.52-34.25	132-180
Nippur/Philus Sulci	G2GSNIPPUR01	49.22-54.72	59.62-63.10	100
Byblus Sulcus	G2GSGRVLNS01	39.37-39.99	52.82-53.95	85
Anshar Sulcus	G8GSANSHAR01	9.39-10.41	67.81-70.32	145
Transitional Terrain	G2GSTRANST01	32.80-37.61	39.30-43.70	190

Table 2.2: Nomenclature and geographic coordinates of Ganymede features. For Ganymede, feature names are derived from Mesopotamian and Egyptian myths, as sanctioned by the official International Astronomical Union. With the exception of craters, names also include Latin-derived descriptive terms, such as *Sulcus* (plural, *Sulci*) meaning parallel grooves and ridges, and *Facula* meaning bright spots. In relation to image plate references, quadrangles are named and numbered according to convention, where for example, "Jg4" refers to "J"upiter satellite "G"anymede quadrangle "4". Longitude coordinates are given in an East-positive convention. Gray entries denote mapped region and corresponding plate; specific features discussed in Section 5 are listed below region name, and in alphabetical order.

Feature name	Latitude (°N)	Longitude (°E)	Plate
Nun Sulci	49.5	43.6	Jg5
Haroeris crater	28.5	63.2	Jg5
Mont crater	44.6	48.1	Jg5, Jg5.1
Nefertum crater	44.3	38.9	Jg5, Jg5.1
Tros crater	11.1	332.7	Jg6
Upuant crater	46.4	40.5	Jg5, Jg5.1
Dardanus Sulcus	-17.5	342.5	Jg6, Jg11
Barnard Regio	-10.7	341	Jg6
Damkina crater	-30	355	Jg11
Mysia Sulcus	-7	352.1	Jg6
Nicholson Regio	-33.5	355.2	Jg10, Jg11
Tiamat Sulcus	3.4	151.5	Jg8, Jg9
Kishar Sulcus	-6.4	143.4	Jg9
Maa crater	1.3	156.4	Jg8, Jg8.8
Uruk Sulcus	0.8	199.7	Jg8
En-Zu crater	11.6	191.6	Jg8, Jg8.2
Arbela Sulcus	-21.1	10.2	Jg10, Jg10.3, Jg14
Nicholson Regio	-33.5	355.2	Jg10, Jg11
Saltu crater	-14.2	7.3	Jg10
Nippur/Philus Sulci	36.9	175	Jg4
Marius Regio	6.8	178.8	Jg4
Byblus Sulcus	37.9	160.1	Jg4
Marius Regio	6.8	178.8	Jg4
Nergal crater	38.6	159.7	Jg4, Jg4.2
Anshar Sulcus	18	162.1	Jg4, Jg8, Jg8.5
Marius Regio	6.8	178.8	Jg4
Thebes Facula	7.1	157.6	Jg8
Transitional Terrain	32	173	Jg4.1
Anhur crater	32.6	167.7	Jg4, Jg4.1
Epigeus crater	23.4	179.4	Jg4, Jg4.5
Marius Regio	6.8	178.8	Jg4

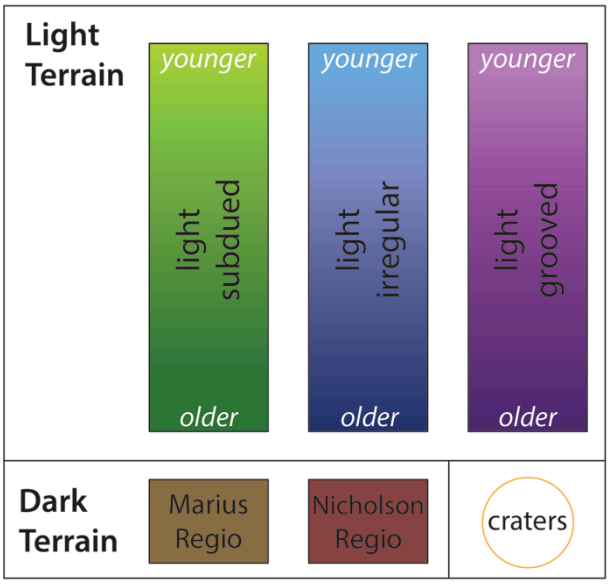

Figure 2.7: Color key for digitized maps (Figures 2.8 – 2.16) denoting material types and relative age. Each light terrain type (light subdued, light irregular, and light grooved) receives a unique color (i.e., green, blue, purple), and relative ages within terrain types are indicated by varying shades (darker with age).

Major structural domains were then grouped and exported as digital data for additional post-processing analyses. For each mapped site, a polar plot angle histogram (rose diagram) is created based on the trend of line segments in relation to the origin point (restricted to 90 - 270° for simplicity). A single rose diagram might combine several domains that are inferred to be of similar age based on their cross-cutting relationships with other domains, and are labeled according to relative age of each domain grouping (e.g., oldest, intermediate, youngest). For this analysis, similar data entries are combined into 10° wide bin domains. Each rose diagram presented in this analysis represents a distribution of values by the combined length (in meters) of line segments of a particular orientation. It is important to note that all mapped structures, whether assessed to be extensional or strike-slip in nature, were weighted equally in the rose diagrams. Finally, deformation stages, illustrated by standard strain ellipses (Figure 2.2a, after Reading (1980) and Harding (1974)) were established to account for orientations of morphological domains (or groups of domains) and the principal stress directions (open white arrows) that support these orientations. Here, open white arrows represent maximum compressive stress (σ_1) and minimum compressive stress (σ_3), which can be visualized as indicating the ‘‘compression axis’’ C and ‘‘extension axis’’ E of each strain ellipse, respectively.

Half-arrows indicate the inferred direction of simple shear, either dextral or sinistral, while a strain ellipse without half-arrows indicates a deformation stage where little indication of strike-slip behavior is inferred. The diagrammatic strain ellipses presented in this paper were configured based on the slip tendency analysis described next.

Slip tendency (T_s) describes the ability of a fault plane to slip in a given stress field, and is defined as the ratio of resolved shear (τ) to normal tractions (σ_n) acting on the plane,

$$T_s = \frac{\tau}{\sigma_n}. \quad (1)$$

The assessment of stress states and potential fault activity using slip tendency analyses has previously been used to assess hazards along terrestrial fault zones (Morris et al., 1996; Lisle and Sribastava, 2004; Collettini and Trippetta, 2007; Moeck and Zimmerman, 2009). Slip tendency analyses assume that faults already exist and are used to assess whether applied stress will cause slip on a fault, and if this slip will be manifested as strike-slip or normal faulting. Because the digitized faults are represented only by their surface traces and fault dip cannot be measured from spacecraft images, each fault trace is evaluated as both a potential vertical strike-slip fault (dipping 90° from the horizontal) and as a modestly dipping potential normal fault (dipping 60° from the horizontal). For this analysis, if the slip tendency, T_s, in pure normal fault mode is larger than the slip tendency in pure strike-slip fault mode, the trace is marked as a normal fault; otherwise it is treated as a strike-slip fault. Pure strike-slip on a fault trace is prohibited if the calculated normal stress on a given fault segment is tensile. All possible shear and normal tractions are calculated by first rotating and evaluating each possible orientation the principal stresses, σ_1 and σ_3, defined as the most and least compressive horizontal stress (deviatoric stress + vertical lithostatic (ρgz) stress), respectively, through 180° in 10° increments. Calculations consider fault planes at a depth of 1 km and assume model parameters appropriate to Ganymede: g = 1.428 m/s^2, ice density, ρ = 930 kg/m^3, and a coefficient of friction of ice (μ_f= 0.55) that is consistent with laboratory estimates of ice friction and previous studies (Schulson and Fortt, 2012). Additionally, a stress multiplier of -1 between σ_1 and σ_3 is applied, making the horizontal stresses equal, but opposite. Changing this multiplier assumption changes the total number of faults that undergo strike-slip, but it does not change the orientation at which the maximum number of faults in a set will slip.

Using the slip tendency method at each of the nine sites studied, models show where mapped structures will be locked, or experience either strike-slip or normal faulting (see Supplementary Material: Slip Tendency Analysis) and allow for the comparison of the prediction with the presence (or absence) of morphological indicators of strike-slip and normal faulting from mapping efforts (described in detail in Section 5). The resulting stress orientation is considered plausible if features with morphological strike-slip indicators undergo the correct sense of shear, and if similarly aged features interpreted as graben or normal fault sets are slipping as normal faults. Stress orientations indicating the wrong shear sense, or locked faults, are considered implausible. Stress orientations are presented for each inferred main stage of tectonic deformation for each of the nine sites studied below.

5. Morphological observations and interpretations

Nine *Galileo* target sites (Figure 2.1a), of varying terrain types displaying evidence of strike-slip indicators, were chosen for this study of strike-slip tectonism. Five of these sites are located primarily in light, grooved terrain (e.g. Nun Sulci, Dardanus Sulcus, Tiamat Sulcus, Uruk Sulcus and Arbela Sulcus); the remaining four sites occur within terrains transitional from dark to light terrain (e.g., Nippur/Philus Sulci, Byblus Sulcus, Anshar Sulcus, and the *Galileo* G2 Transitional Terrain target site). Sites also represent different hemispheric regions on Ganymede: trailing, leading, anti-Jovian, and sub-Jovian (Figure 2.1a). This section discusses the geologic setting of these nine sites, morphologic interpretations from the digitization efforts, the presence of strike-slip indicators, and inferred stress histories consistent with these observations. Note that the process of inferring geologic history (cause) from structures (effect) is distinct from traditional methods typically used to infer terrestrial geologic relationships and take care to consider uncertainties due to this in Section 6.

5.1. Grooved Terrain

5.1.1. Nun Sulci

The two-frame image mosaic of the Nun Sulci site (Figure 2.8a) shows a complex group of intersecting bands of light terrain generally trending NW-SE or E-W (Collins et al., 1998c). The

strained crater Nefertum, measures ~35 km in width and shows pervasive fracturing and elongation. Other named craters include ~14 km diameter Upuant and 11 km diameter Mont. The bright splotches that appear throughout the site are inferred to be secondary craters from bright-ray craters Tros, a ~95 km diameter central dome crater located ~3690 km to the southwest of the image mosaic (Moore and Malin, 1988; Schenk et al., 2004), and Haroeris, located ~1310 km to the southeast of the image mosaic. Arcuate, scalloped features in the eastern portion of the image mosaic have been interpreted as cryovolcanic calderas (Lucchitta, 1980; Schenk and Moore, 1995; Head et al., 1998; Kay and Head, 1999; Schenk et al., 2001; Spaun et al., 2001).

Here we identify seven domains of similar morphologies in this primarily light terrain site (Figure 2.8b), with only a small area of dark terrain present (label j). The oldest domains 1 – 3 are grouped separately based on variations from smooth to more heavily grooved terrain (Figure 2.8c); all share a similar NW-SE trend of lineations within domains, although domain 3 contains some NE-SW trending structures. Domain 1 consists of both subdued and grooved terrain, domain 2 is heavily grooved and bounded on each side by prominent troughs, and domain 3 consists of mostly subdued grooves. Structures in the youngest domains (4 – 7) have an E-W trend and crosscut domains 1 – 3, while the boundary between domains 2 and 6 is ill-defined. Several domains have plentiful examples of *en echelon* structures (labels d – i) and possible left-lateral offset (labels b – c, see also Murchie and Head, 1988). Analyses performed by Pappalardo and Collins (2005) on the strained crater Nefertum (label a, see also Supplementary Figure 10) suggests right-lateral deformation; we find the orientation of expected right-lateral R shears corresponds with the strained crater's major axis.

We infer two main stages of tectonic deformation of light terrain at Nun Sulci (Figure 2.8d): (Stage I) NE-SW extension and normal faulting of the oldest domains (1 – 3), perhaps accompanied by a component of right-lateral shearing along the R shearing axis of Nefertum crater. Slip tendency analysis suggests that a principal stress orientation of σ_1 = 140° – 150° provides the best match to these observations (Supplementary Figure 1); (Stage II) counterclockwise rotation of the principal stresses about a vertical axis to a NW-SE extensional regime, resulting in left-lateral offset (Murchie and Head, 1988) of domain 2 along the simple shear axis, reactivation of extensional fractures in youngest domains (4 – 7), and formation of several *en echelon* fractures in domain 1. Slip tendency analysis suggests a principal stress

orientation of σ_1 = 60° – 70° provides the best match to these observations (Supplementary Figure 1). For Stage I, strike-slip indicators are less prevalent, as indicated by the absence of half-arrows of its representative strain ellipse; we infer that extension dominated this first stage.

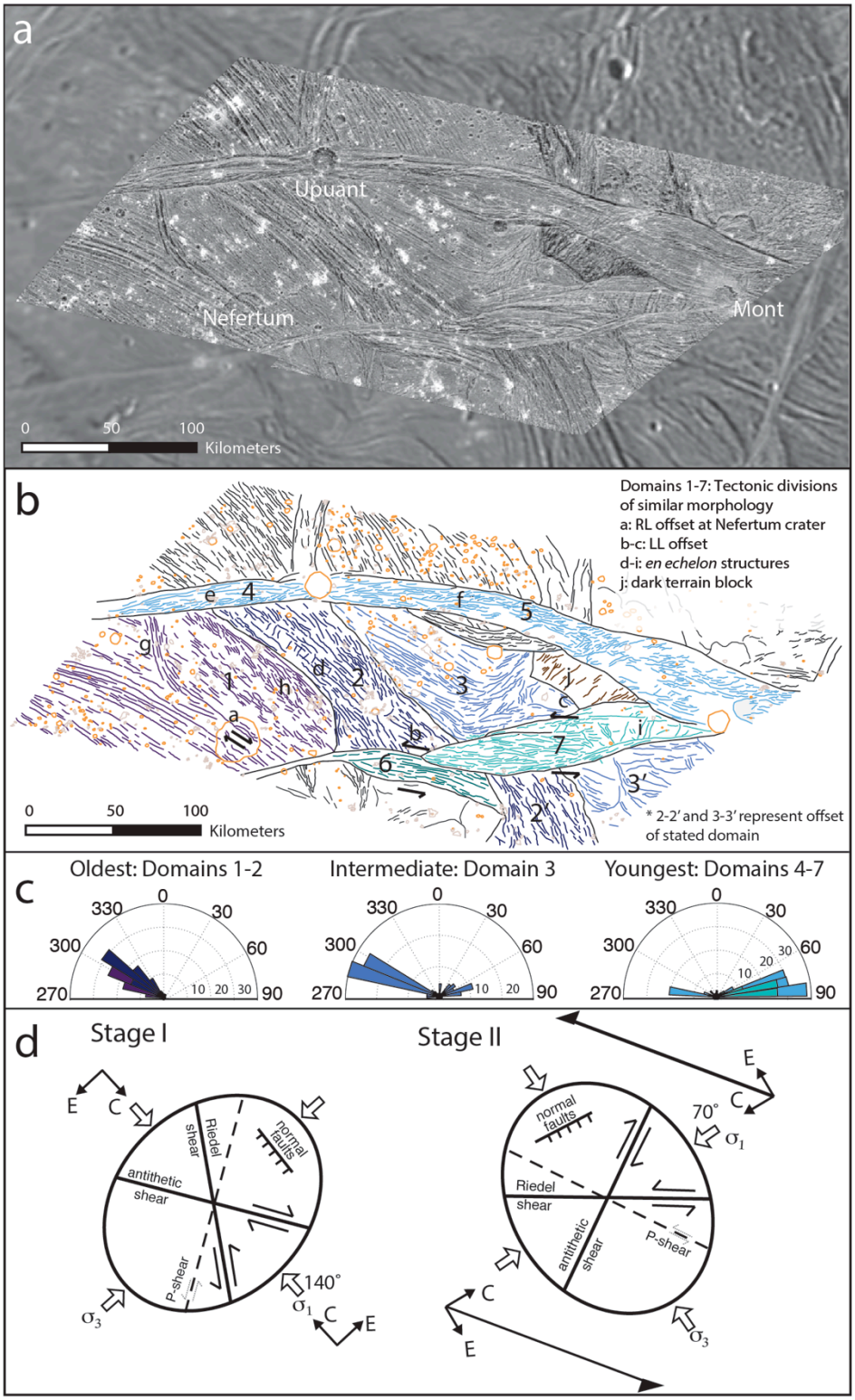

Figure 2.8: Nun Sulci. (a) Voyager background imagery underlying Galileo high-resolution imagery, (b) lineament map, with letters and numbers referred to in the text, (c) rose diagrams (by length), and (d) diagrammatic strain ellipses.

5.1.2. Dardanus Sulcus

Galileo image resolution for Dardanus Sulcus (Figure 2.9a, Table 2.2) was lower than for other regions in this study (Collins et al., 2013). Dardanus Sulcus is a NW-SE trending band of light terrain ~150 km wide that cuts the surrounding Nicholson Regio dark terrain in the sub-Jovian hemisphere. It displays ~45 km of right-lateral offset along an unnamed NE-SW fault with a wavy planform that cuts through Nicholson Regio (Murchie and Head, 1988). *En echelon* structures are observed in several of the light terrain domains. Barnard Regio and Mysia Sulci lie north of Dardanus Sulcus near the top of the mosaic. Damkina, a ~175 km wide central dome crater, is visible at the lower right of the image mosaic.

Here we identify eight domains of distinct morphology (Figure 2.9b), with the oldest (domain 1) being the heavily cratered dark terrain of Nicholson Regio. Intermediate light terrain (domains 2 – 4) cross-cut Nicholson Region and are subsequently cross-cut by younger light terrain (domains 5 – 8). A NE-SW striking fault (label a) offsets the grooved terrain of domains 2 and 3 ~45 km right-laterally (Murchie and Head, 1988). Possible *en echelon* structures indicative of left-lateral shear are visible in domain 2 (label b, see also Supplementary Figure 10). We interpret domain 4 to represent the southern extension of domain 3, as they appear to have similar grooved terrain spacing and appearance. Domain 5 appears to have a less organized internal structure than domains 2 – 4, and also is oriented quite differently. The relationship of domains 7 and 8 with respect to other domains is unclear, but domain 7 shares a similar orientation and appearance to domain 8. Rose diagrams of structures within the dark terrain indicate the structure generally strikes NW-N (Figure 2.9c). The intermediate-aged offset band of light terrain trends mostly NW, while the lineations of the youngest of the light terrain domains trends NE (Figure 2.9c). Domain 6, a thin swath of grooved material that shares a similar orientation to domains 2 – 4, appears to crosscut domain 5, but we do not clearly understand how the feature fits into the tectonic history. Domain 6 could be the youngest domain and reflect an additional period of tectonic deformation. Due to this uncertainty, we do not include it in our slip analysis.

We infer two main stages of tectonic deformation of light terrain at Dardanus Sulcus (Figure 2.9d): (Stage I) ENE-WSW extension of the oldest of the bright terrain domains 2 – 4. We do not include domain 1 due to the lack of distinct, linear structures. Slip tendency analysis suggests a

principal stress orientation of σ_1 = 170° provides the best match for extension of the light terrain domains (Supplementary Figure 2); (Stage II) counterclockwise rotation of the principal stresses about a vertical axis to a more NE-SW extension regime resulting in right-lateral slip of domains 2 and 3 along the fault. Slip tendency analysis suggests a principal stress orientation of σ_1 = 120° – 140° provides the best match for the inferred right-lateral offset (Supplementary Figure 2).

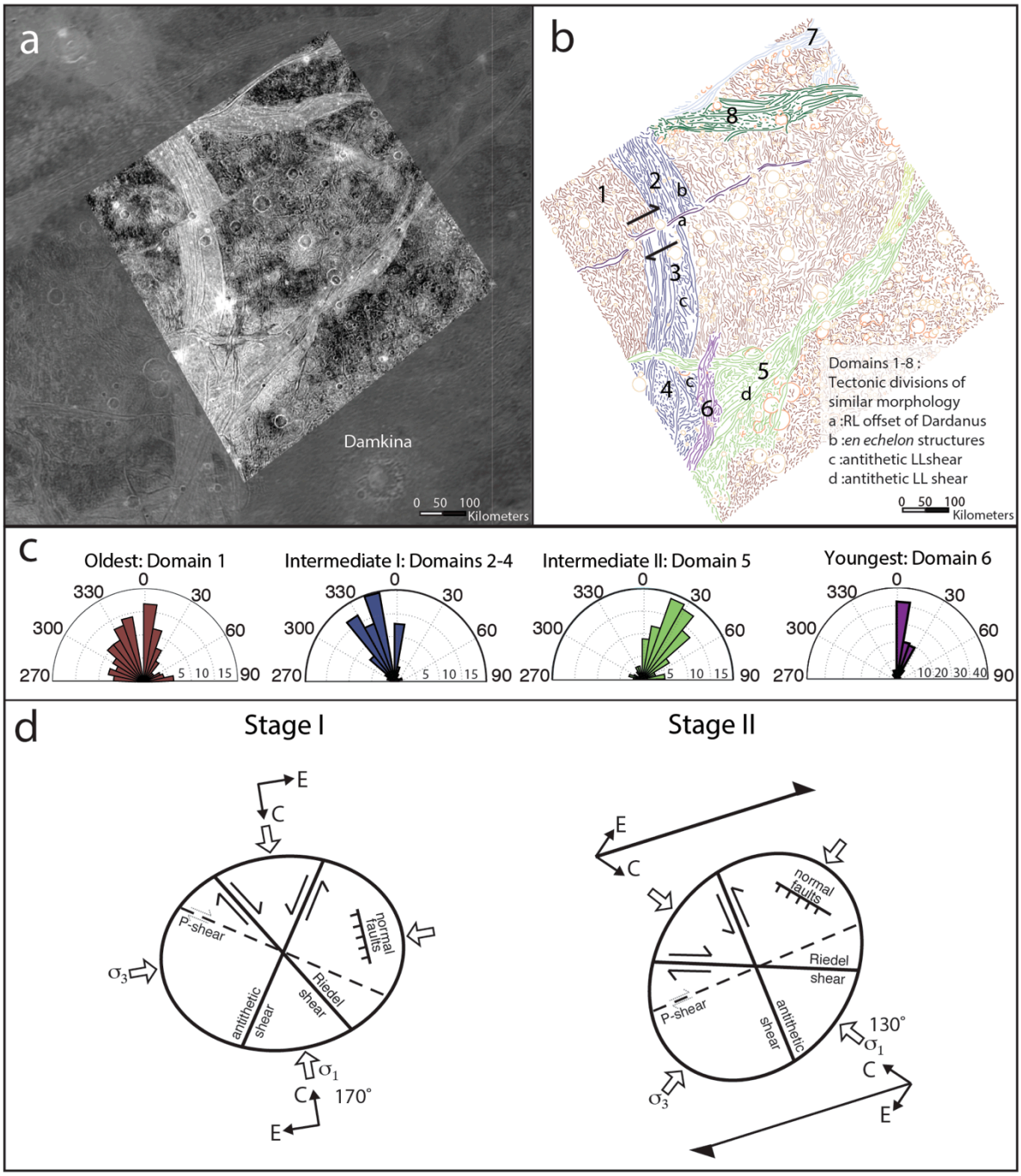

Figure 2.9: Dardanus Sulcus. (a) Voyager background imagery underlying Galileo high-resolution imagery, (b) lineament map, with letters and numbers referred to in the text, (c) rose diagrams (by length), and (d) diagrammatic strain ellipses.

5.1.3. Tiamat Sulcus

Tiamat Sulcus (Figure 2.10a) appears as a band of light terrain trending NW-SE and cutting through the dark terrain of Marius Regio. Tiamat Sulcus appears to be tens of kilometers wider south of the NE-SW trending Kishar Sulcus than to its north. Murchie and Head (1988) interpreted that right-lateral slip occurred here, and perhaps the southern section of Tiamat experienced more extension, as the light terrain in the southern portion of Tiamat seems to either be contemporaneous or postdate the slip along Kishar Sulcus. Other bands of light terrain in the east appear to bend either south from an initial NE-SW trend, or north from an initial NW-SE trend. Maa crater (Figure 2.10a) measures ~ 30 km in diameter, and many other older, relatively flat and presumably viscously relaxed, craters appear throughout the dark terrain.

Here we identify twelve domains of distinct morphology in this rather complex region (Figure 2.10b). The oldest domains (1 – 3) belong to the surrounding Marius Regio dark terrain, while intermediate (4 – 10) and young (11 – 12) light terrain domains primarily trend NW-SE and NE-SW (Figure 2.10c). Murchie and Head (1988) examined this region and refer to domains 11 and 12 as a single lineament, but also note the ~30° – 40° change in orientation from the northwestern to southeastern end. Domains are distinguished by changes in orientation of internal structure, and also by appearance, most notably the uniquely braided appearance of domain 4. Braided, or anastomosed zones, are sometimes observed in strike-slip systems on Earth, such as the Carboneras fault in Spain, where an array of steeply dipping fault planes link to form a complex system of branching faults and shear lenses (Keller, et al., 1995; Davis et al., 2000; Faulkner et al., 2003). *En echelon* structures are observed in many of the light terrain domains (labels c – e, see also Supplementary Figure 10) including within the braided domain 4. There are also instances of possible right-lateral offset between domains 6 and 7 (label b) judging by the similarity of groove spacing along domain 9, Kishar Sulcus. Additionally, domain 8 appears to have experienced right-lateral slip along domain 11; a clear example of offset (Murchie and Head, 1988) lies off the digitized map area.

We infer three corresponding stages of deformation of light terrain at Tiamat Sulcus (Figure 10d): (Stage I) NNW-SSE extension of dark terrain domains (1 – 3), as well as formation of domain 9. We note that domains 1-3 may instead be related to furrow formation, limiting this strain ellipse to account only for the formation of domain 9; additionally, strike-slip indicators

are minimal here. Slip tendency analysis suggests a principal stress orientation of σ_1 = 40°-60° provides the best match for extension of these domains (Supplementary Figure 3); (Stage II) NE-SW extension of old to intermediate aged domains (4 – 7), right-lateral shearing, and offset of domain 9 along simple shear axis. Slip tendency analysis suggests a principal stress orientation of σ_1 = 130° provides the best match to these observations (Supplementary Figure 3); (Stage III) slight clockwise rotation of the principal stresses about a vertical axis with formation and perhaps right-lateral shearing of the young domain 11. Slip tendency analysis suggests a principal stress orientation of σ_1 = 150° – 180° provides the best match to these observations (Supplementary Figure 3).

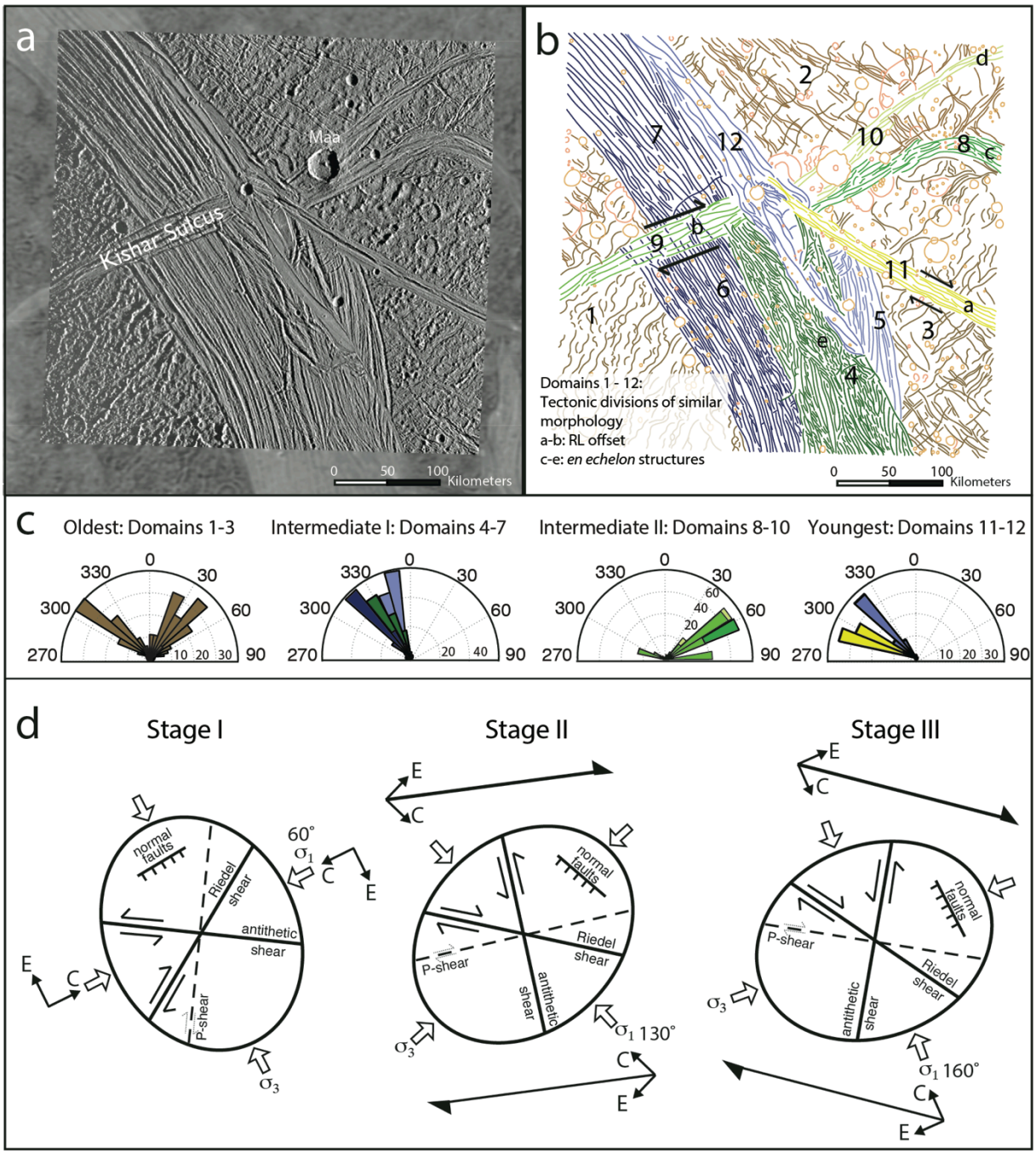

Figure 2.10: Tiamat Sulcus: (a) Voyager background imagery underlying Galileo high-resolution imagery, (b) lineament map, with letters and numbers referred to in the text, (c) rose diagrams (by length), and (d) diagrammatic strain ellipses.

5.1.4. Uruk Sulcus

This five-frame image mosaic of the Uruk Sulcus region (Figure 2.11a) displays several intersecting bands of light terrain with various trends (cf. Pappalardo et al., 1998). For example, a NE-SW trending section of light terrain in the northeastern corner of the mosaic is cut by a NW-SE band of light terrain, which may also cut an older impact crater. Packets of N-S trending grooves occur throughout. Stereo coverage implies a close correlation between albedo variations and topography, with bright material along topographic highs, such as ridges, and dark material at local topographic lows, such as trough and crater floors (Collins et al., 1998b; Oberst et al., 1999). One of these dark floored craters is the ~6 km diameter En-Zu (labeled), and many small craters spot the site. Previous studies by Collins et al (1998b) suggest two scales of ridges and troughs are observed in the Uruk Sulcus region.

Here we identify fifteen domains of distinct morphology in this complex section of light terrain; no dark terrain appears in this region (Figure 2.11b). The oldest domains (1 – 4) belong to pitted and lineated terrain of various orientations. Younger domains (6 – 15) compose the more striated and ridged terrain of this region. The oldest domains in this site are predominantly NNW-SSE and NNE-SSW, while younger domains trend more NW-SE (Figure 2.11c). *En echelon* structures are prevalent in the younger domains (labels a – d), and a possible strike-slip duplex is among the youngest domains (label e, see also Supplementary Figure 2.10). This duplex may be an example of a lensoid with subparallel internal structure, or duplex class (3), as described in Section 3.2.

We infer three main stages of deformation of light terrain at Uruk Sulcus (Figure 2.11d): (Stage I) NW-SE extension and formation of pitted terrain domains (2 – 4) through normal faulting with formation of left-lateral antithetic shear structures within domains 3 and 4. Slip tendency analysis suggests a principal stress orientation of σ_1 = 20° – 30° provides the best match to these observations (Supplementary Figure 4). Domain 1 was not included in the slip tendency analysis due to the severely reduced image resolution; (Stage II) counterclockwise rotation to a E-W extension direction, along with formation of intermediate aged bright terrain domains (5 – 9) through normal faulting. Slip tendency analysis suggests a principal stress orientation of σ_1 = 170° – 10° provides the best match to these observations (Supplementary Figure 4); (Stage III) counterclockwise rotation of the principal stresses about a vertical axis to a

NE-SW extension, and formation of young domains (10 – 15) with possible right-lateral shearing and normal faulting. *En echelon* features in domain 15 align with the implied right-lateral R shear axis, while features within the duplex of domain 14 correlate to the inferred extension direction. Slip tendency analysis suggests a principal stress orientation of σ_1 = 150° – 160° provides the best match to these observations (Supplementary Figure 4). These results are in agreement with Collins et al. (1998a), in which the least compressive stress (here labeled σ_3) for the oldest units was NW-SE, rotating over time to a NE-SW orientation during the formation of the youngest units.

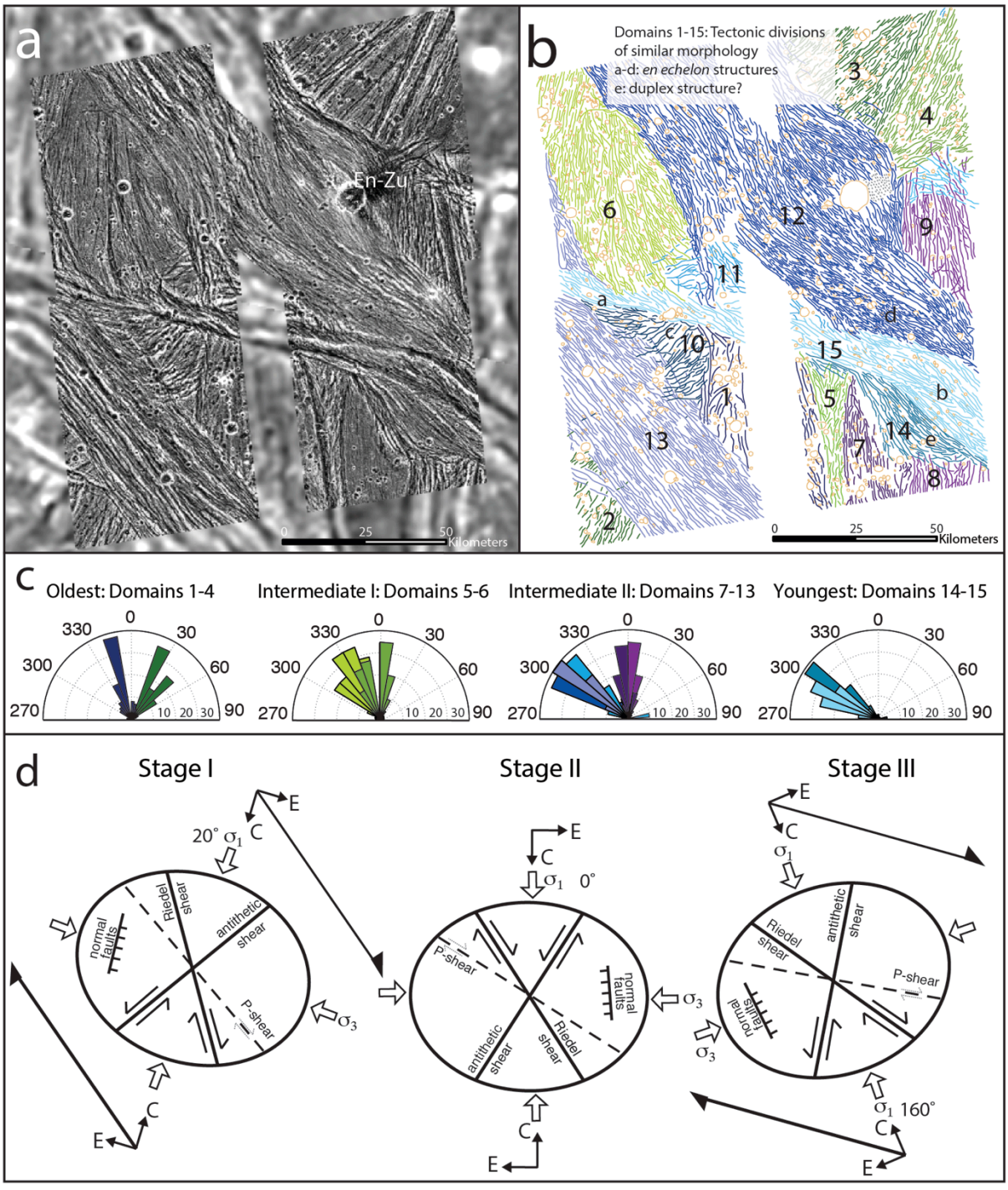

Figure 2.11: Uruk Sulcus: (a) Voyager background imagery underlying Galileo high-resolution imagery, (b) lineament map, with letters and numbers referred to in the text, (c) rose diagrams (by length), and (d) diagrammatic strain ellipses.

5.1.5. Arbela Sulcus

The multi-frame mosaic of the Arbela Sulcus region (Figure 2.12a) contains the dark terrain of Nicholson Regio, and two bands of light terrain trending NE-SW cut through the eastern portion of the site. One of these bands is intensely grooved and may be transitional from normal-faulted dark terrain (Patel et al., 1999) and is disrupted by the second, much smoother band, Arbela Sulcus. Nicholson Regio also has several regions of narrow fractures throughout, especially noticeable in the southeastern area of the mosaic. One of these fracture zones splits the ~30 km wide crater, Saltu, and is identified as a possible strained crater by Pappalardo and Collins (2005). In fact, the site contains three strained craters examined by Pappalardo and Collins (2005): Saltu crater (label e), and two unnamed strained craters (label d). A possible split crater (label c – c'; Head et al., 2002) is also mapped. A relatively bright and smooth area just north of Saltu may be a palimpsest: an ancient, circular, low-relief impact scar that is different in appearance from typical impact craters (Guest et al., 1988; Lucchitta et al., 1992; Jones et al., 2003).

Here we identify five domains of distinct morphology (Figure 2.12b). This region is dominated by the dark, heavily cratered terrain of Nicholson Regio (domain 1) and contains fractures that trend NE-SW (Figure 2.12c). The younger domains (2 – 5) within the Arbela Sulcus site include a NE-SW trending highly grooved band and an even younger NNE-SSW trending smooth band (domain 3). The latter shows possible structures associated with left-lateral shear of the grooved band of domain 2 (label a, see also Supplementary Figure 10), consistent with a step-over feature in domain 3 (label b, see also Supplementary Figure 10). The relationship of domains 4 and 5 and other domains in the site is difficult to determine given limited high-resolution imagery; we note that these domains have a similar appearance and orientation to domain 2.

We infer two main stages of deformation of light terrain at Arbela Sulcus based on the general orientation of the structures in the bright terrain domains 2-5 (Figure 2.12d): (Stage I) NW-SE extension (matching the inference of Pappalardo and Collins (2005) based on the direction of lengthening at Saltu crater), along with formation of bright terrain domain 2. Slip tendency analysis suggests a principal stress orientation of σ_1 = 40° – 60° provides the best match to the extensional formation of domain 2 (Supplementary Figure 5); (Stage II)

counterclockwise rotation of the principal stresses about a vertical axis to a WNW-ESE extension, with formation of domain 3 through normal faulting, along with possible left-lateral shear of domain 2 along the antithetic shear axis. Slip tendency analysis suggests a principal stress orientation of $\sigma_1 = 0° – 30°$ provides the best match to the extensional formation of domain 3 (Supplementary Figure 5). Indeed, a reconstruction by Head et al. (2002) suggests the bright smooth lane of Arbela Sulcus (defined here as domain 3) formed through crustal separation, left-lateral strike-slip, and counterclockwise relative rotation of the eastern portion of the mosaic. Additionally, the major-axis of the possible right-lateral strained crater Saltu aligns with the right-lateral R shear axis, while the major-axis of the left-lateral strained unnamed craters (label d) aligns with the left-lateral antithetic shear axis.

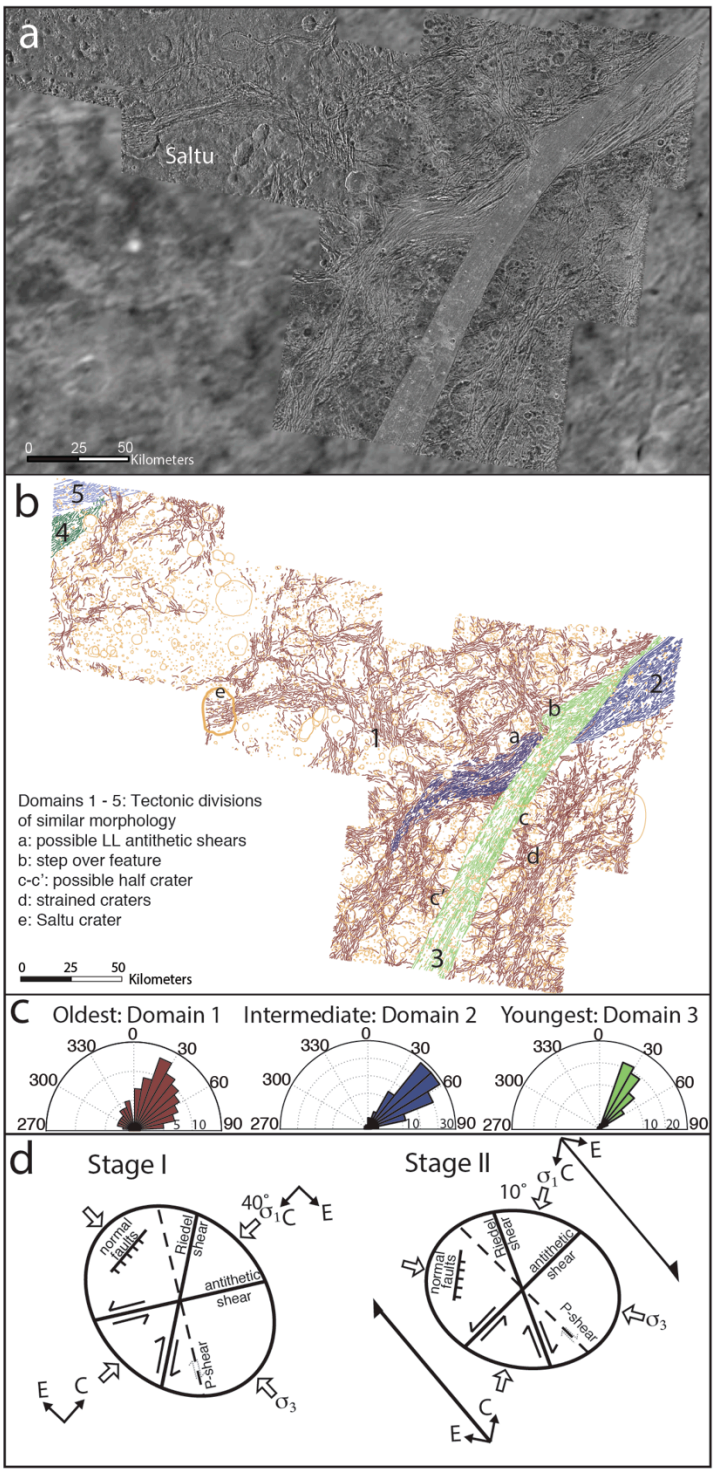

Figure 2.12: Arbela Sulcus: (a) Voyager background imagery underlying Galileo high-resolution imagery, (b) lineament map, with letters and numbers referred to in the text, (c) rose diagrams (by length), and (d) diagrammatic strain ellipses.

5.2. Dark to light transitional terrain

5.2.1. Nippur/Philus Sulci

In the three-frame mosaic of the Nippur/Philus Sulci site (Figure 2.13a), several crosscutting bands of light terrain show differing degrees of deformation from smooth and less deformed bands, to heavily grooved and deformed terrain. The narrow, NW-SE trending smooth band Nippur Sulcus shows the least amount of deformation in the site. In the northeastern corner of the mosaic, NW-SE trending light terrain appears to partially fracture a zone of light terrain that trends E-W. The light terrain of Philus Sulcus lies south of Nippur Sulcus and displays fractures striking NE-SW. In contrast, a NW-SE trending belt, that may mark a series of grabens, cuts through Philus Sulcus. The heavily deformed dark terrain of Marius Regio shows multiple furrows in the southeastern portion of the site, as well as a possible unnamed strained crater (label e, Figure 2.13b; see Pappalardo and Collins, 2005).

Here we identify six domains of distinct morphology (Figure 2.13b). The dark terrain of Marius Regio (domain 1) contains structures that trend NW-SE, with a lesser contribution of structures oriented E-W (Figure 2.13c), with some features that may be related to furrow formation (dashed blue lines). The oldest of the light terrain, domain 2, trends almost E-W and is located in the northeastern corner of the site; domain 3 trends NE-SW and shares an orientation with the furrows (dashed lines) of the dark terrain; the youngest domains (4 – 6) trend more NW-SE. Domain 5 is grouped separately from domain 4 due to a slight change in orientation, most noticeable in the *Voyager* context imagery. The smooth band of domain 6 borders the abrupt change in orientations between southern and northern light terrain. There are few direct indicators of strike-slip tectonism in this region: some *en echelon* structures within domain 3 (label d) and domain 5 (label a, see also Supplementary Figure 10), possible right-lateral offset (label c) of inferred drag features (label b) within Philus Sulcus, and a possible right-lateral strained crater (Pappalardo and Collins, 2005) within domain 1 (label e). Pappalardo and Collins (2005) note that at least three differently oriented sets of fractures cut this crater, including lineaments that are subparallel to Philus Sulcus, suggesting the dextral shear inferred within Philus Sulcus may also have deformed the neighboring dark terrain and crater.

We infer three main stages of tectonic deformation of the light terrain in the Nippur/Philus

Sulci site (Figure 2.13d): (Stage I) NW-SE extension and formation of dark terrain structures and furrow system of domain 1. Slip tendency analysis suggests a principal stress orientation of σ_1 = 60° provides the best match to an extensional formation of domain 1 (Supplementary Figure 6). We note the complex nature of domain 1, coupled with the possibility that some structures may be impact related furrow structures, may result in uncertainty (as denoted by the asterisk in Figure 2.13d); (Stage II) clockwise rotation of the principal stresses about a vertical axis to a N-S extension and formation of the northeastern most domain 2 of Philus Sulcus through normal faulting, along with possible right-lateral shearing of the strained crater in domain 1, and offset of drag features in domain 3 along the simple shear axis. The oldest light terrain of domain 2 is difficult to place into one of these two tectonic episodes, but it does predate all the other light terrain domains. Slip tendency analysis suggests a principal stress orientation of σ_1 = 80° – 100° provides the best match to these observations (Supplementary Figure 6); (Stage III) NE-SW extension and formation of the remaining young domains (4 – 6), with domain 6 sharing the inferred orientation for normal faulting. Slip tendency analysis suggests a principal stress orientation of σ_1 = 140° – 150° provides the best match to these observations (Supplementary Figure 6).

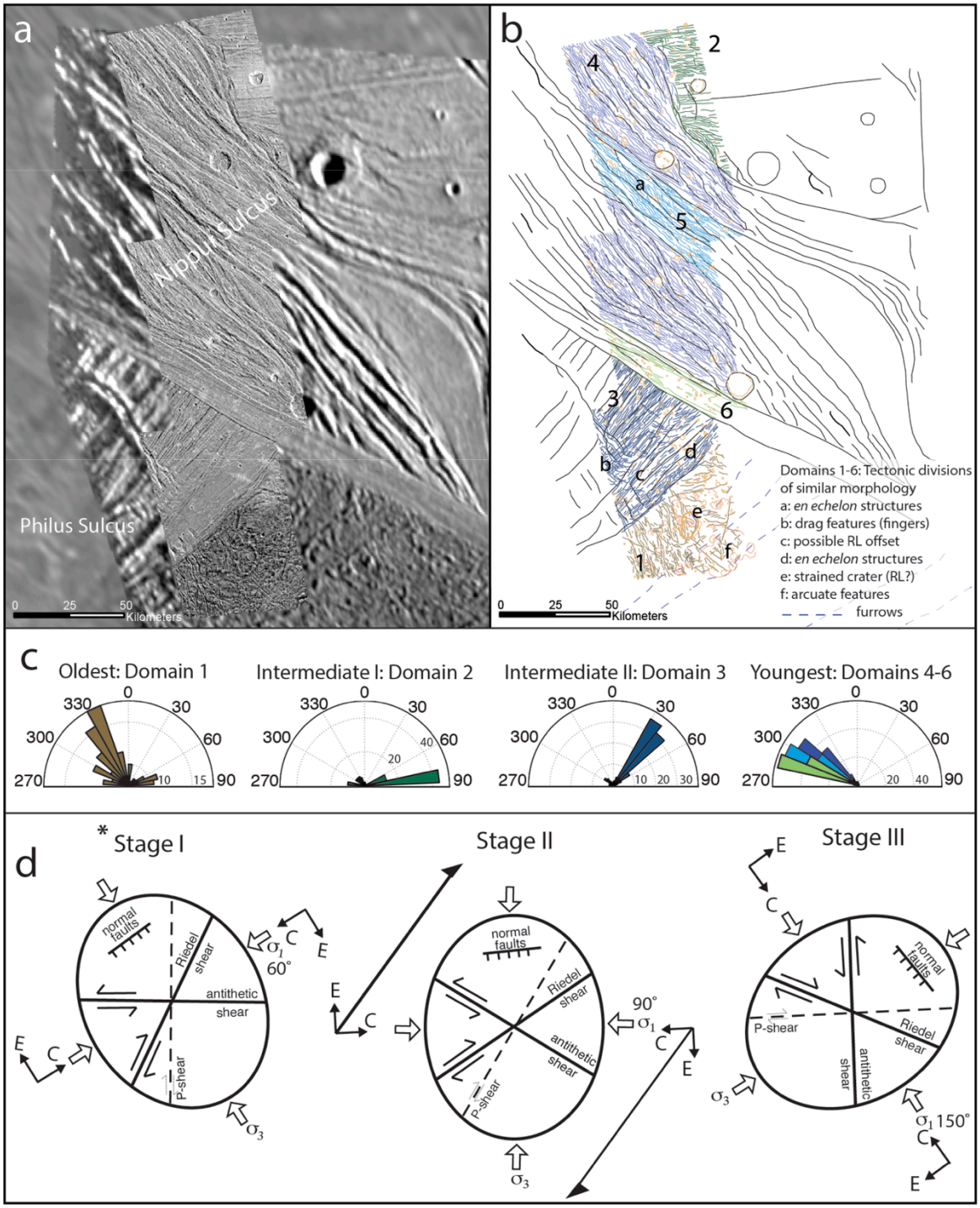

Figure 2.13: Nippur/Philus Sulci: (a) Voyager background imagery underlying Galileo high-resolution imagery, (b) lineament map, with letters and numbers referred to in the text, (c) rose diagrams (by length), and (d) diagrammatic strain ellipses. *Asterisk denotes uncertainty in principal stress orientations due to prominent furrows that may be impact related structures.

5.2.2. Byblus Sulcus

Byblus Sulcus (Figure 2.14a) is a lane of light terrain oriented NW-SE which transects the surrounding dark terrain of Marius Regio. The dark terrain west of Byblus shows a degraded furrow that truncates at Byblus Sulcus. Other narrow fractures in the dark terrain east of Byblus appear to truncate at Byblus Sulcus, while similar narrow fractures occur throughout the site. Nergal (labeled, Figure 2.14a) is a ~8 km wide dark floored crater located near the center of the image mosaic and which post-dates Byblus.

Here we identify three domains of distinct morphology (Figure 2.14b). The oldest is the dark terrain of Marius Regio, containing minor structures that trend both NW-SE and NE-SW (Figure 2.14c); fracture chronology in this terrain is difficult to determine, and could have possibly formed simultaneously as conjugate sets, and may contain structures related to furrow formation (dashed blue lines). Domain 2 is distinguished from domain 1 by its more grooved appearance. Domain 3 is a mostly smooth band, with orientation similar to the NW-SE trends of grooves in the dark terrain, perhaps indicating a genetic relationship between the two domains. This region also hosts few strike-slip indicators, with some possible *en echelon* structures observed in domain 2 (label b, see also Supplementary Figure 10). Although limited by resolution in the surrounding images, the northwestern curving planform shape of domain 2 may indicate it is part of a fault duplex (label a).

We infer two primary stages of tectonic deformation here, notably without a dominant shearing presence (Figure 2.14d): (Stage I) Considering only NW-SE extension and formation of NE-SW extensional features in the Marius Regio dark terrain domain 1, slip tendency analysis suggests a principal stress orientation of σ_1 = 60° provides the best match to the extensional formation of domain 1 (Supplementary Figure 7), and matches the orientation from nearby Nippur/Philus Sulci's stage I; (Stage II) counterclockwise rotation of the principal stresses about a vertical axis to a NE-SW extension and formation of the band of the grooved light terrain (domain 3) through normal faulting, with possible reactivation of NW-SE structures in Marius Regio dark terrain. Additionally, the possibly left-stepping *en echelon* features within domain 2 align with the right-lateral Reidel shear axis. Slip tendency analysis suggests a principal stress orientation of σ_1 = 130° – 140° provides the best match to the extensional formation of domain 3 (Supplementary Figure 7), and matches the extension orientation from nearby Nippur/Philus

Sulci's stage III.

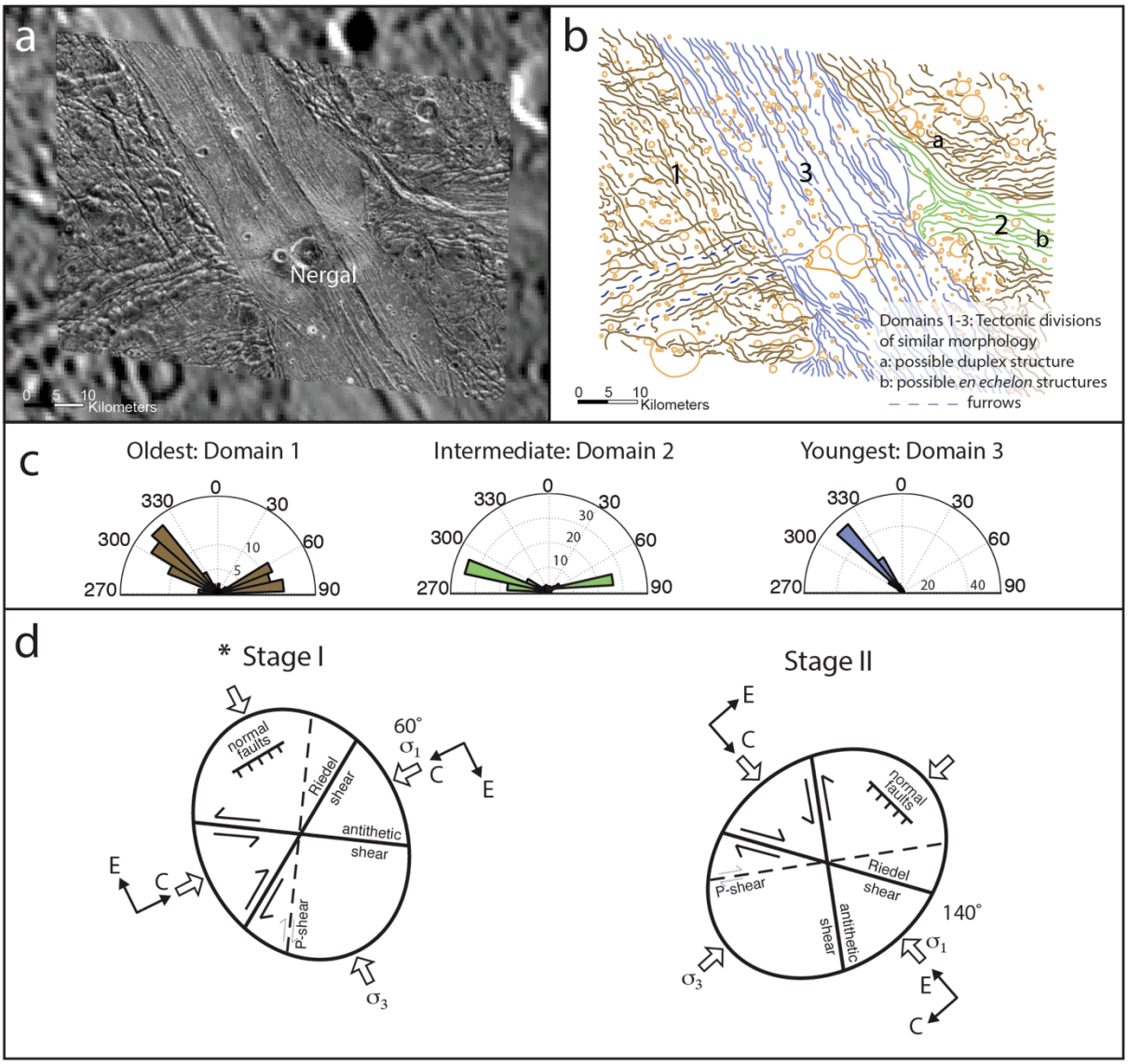

Figure 2.14: Byblus Sulcus: (a) Voyager background imagery underlying Galileo high-resolution imagery, (b) lineament map, with letters and numbers referred to in the text, (c) rose diagrams (by length), and (d) diagrammatic strain ellipses. *Asterisk denotes uncertainty in principal stress orientations due to prominent furrows that may be impact related structures.

5.2.3. Anshar Sulcus

The Anshar Sulcus area is composed of mostly Marius Regio dark terrain (Figure 2.15a), with a very narrow (~20 km wide) band of generally NW-SE oriented light terrain that cuts across the site, truncating several craters in the surrounding dark terrain. The dark terrain is pervasively fractured, and in some cases craters have been pulled apart, including the ~22 km wide unnamed crater (label a, Figure 2.15b) identified as a strained crater by Pappalardo and Collins (2005). A reconstruction by Prockter et al. (2000) of a crater that appears to be missing its southern rim (label i, Figure 2.15b) suggests the crater was rifted and destroyed during the sulcus formation, rather than just pulled apart. Recent studies by Pizzi et al. (2017) suggests the missing portion of the rim may have been erased by subsequent cratering events, or by superimposed furrows, and that spreading or crustal separation still best describes the observed features of the region. Other fractures in the southwestern portion of the site are perhaps related to Thebes Facula, a palimpsest located east of the image mosaic. Several degraded furrows trend NE-SW in the dark terrain as well.

Here we identify six domains of distinct morphology (Figure 2.15b), with domains 1 and 2 belonging to the heavily cratered Nicholson Regio, with structural trends that are both NE-SW and NW-SE (Figure 2.15c). While the NW-SE trending structures of domains 3 and 4 do share an orientation with structures in the surrounding dark terrain, the appearance of these domains are much more heavily fractured. Structures within domain 5 trend NE-SW and represent a large zone of *en echelon* structures (Prockter et al., 2000), though we note formation of domain 5 may have preceded the formation of domains 3 and 4. Domain 6 is a heavily grooved, trough-bounded structure trending NW-SE. This region contains prevalent *en echelon* structures in both dark and light terrain (labels b-g, see also Supplementary Figure 10). In addition, the unnamed strained crater (label a) suggests a left-lateral component of strike-slip (Pappalardo and Collins, 2005). What may be a right-lateral fault splay is visible at the eastern portion of the high-resolution image boundary (label h).

We infer two main stages of deformation within the Anshar Sulcus site (Figure 2.15d): (Stage I) ENE-WSW extension and formation of structures within dark terrain domain 2 and light terrain domains 3 and 4. Furthermore, this ENE-WSW extension matches the direction of inferred lengthening along the unnamed strained crater. Slip tendency analysis suggests a

principal stress orientation of σ_1 = 110° – 120° provides the best match to the extensional formation of light terrain domains 3 and 4 (Supplementary Figure 8); (Stage II) Counterclockwise rotation of the principal stresses about a vertical axis to a NE-SW extension direction and formation of the youngest bright terrain domain (6) through normal faulting, as well as right-lateral shearing of the eastern margin of Anshar Sulcus. Slip tendency analysis suggests a principal stress orientation of σ_1 = 130° – 160° provides the best match to these observations (Supplementary Figure 8). These results coincide with the previous findings of Prockter et al. (2000).

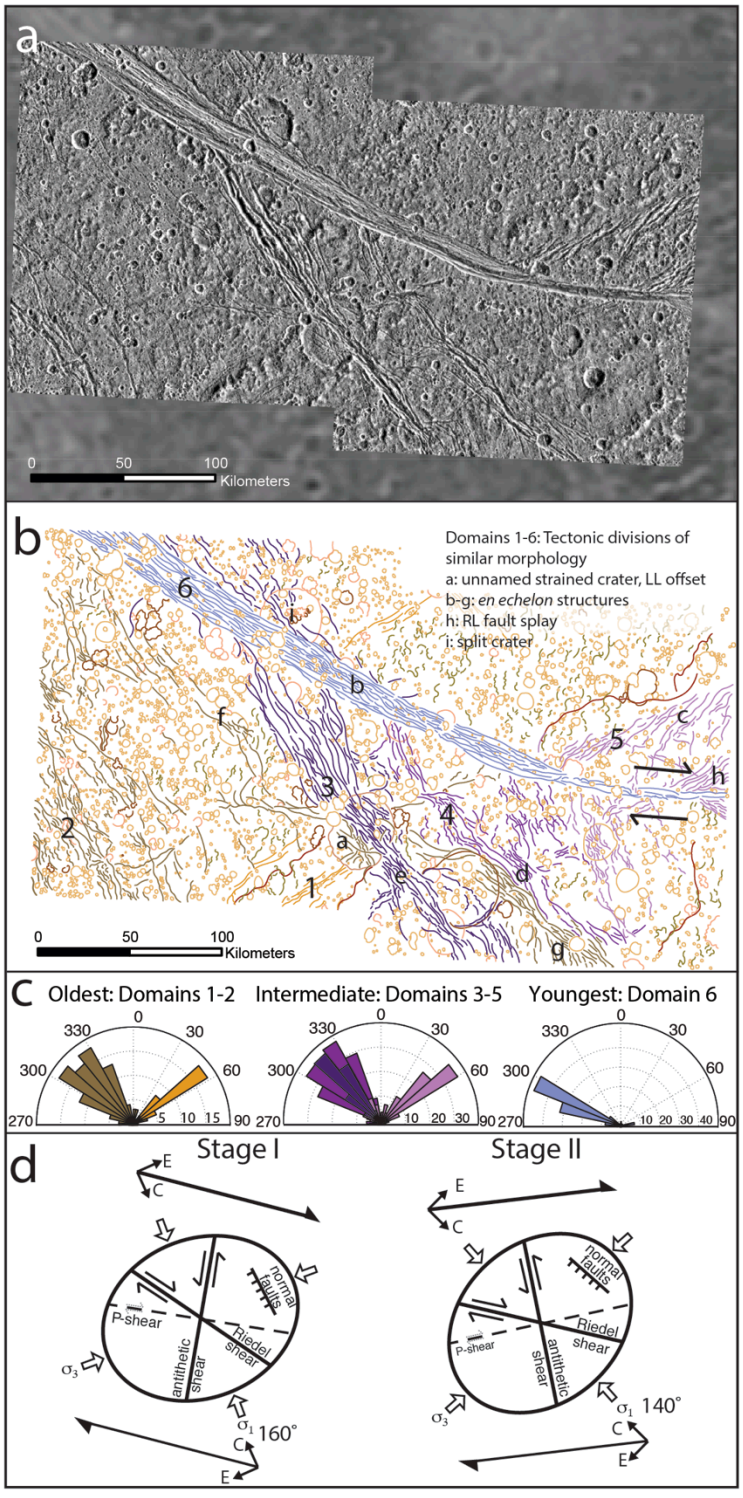

Figure 2.15: Anshar Sulcus: (a) Voyager background imagery underlying Galileo high-resolution imagery, (b) lineament map, with letters and numbers referred to in the text, (c) rose diagrams (by length), and (d) diagrammatic strain ellipses.

5.2.4. Transitional Terrain

The four-frame mosaic of the "Transitional Terrain" site imaged during the *Galileo* G2 encounter (Figure 2.16a) contains the dark terrain of northern Marius Regio, which is broken into blocks by narrow lanes and patches of bright terrain. The dark terrain is heavily fractured with numerous grabens, especially in the southern portion of the site. Patches of dark terrain that are most heavily fractured are also brightest, suggesting that the formation of bright terrain is related to intense fracturing of ancient dark terrain (see Prockter et al., 1998, 2000; Moore et al., 1999; Oberst et al., 1999). Noticeable fault duplex shapes are likely associated with strike-slip. A small section of Nippur Sulcus (labeled) lies at the northeast of the image mosaic. The ~25 km diameter Anhur crater (labeled) is located in the eastern portion of the image mosaic, with many of the other craters in the south and east inferred to be secondary craters from the ~340 km diameter penepalimpsest Epigeus (Schenk et al., 2004), just southeast of the image mosaic.

Here we identify ten domains of distinct morphology (Figure 2.16b), with *en echelon* structures (labels d – e, see also Supplementary Figure 10) and fault duplexes (labels b – c) characterizing the region. We have separated domain rose diagrams by terrain type rather than age in order to distinguish bounding structures. The lensoid bounding structures of the inferred central duplex (label b) suggests it is an example of duplex class 2 structure as described in Section 3.2. Discontinuous fractures suggesting a lensoid shape (duplex class 1 structure) characterize the outer duplex (label c). The dark terrain of Marius Regio (domains 1 – 3) shows primarily NW-SE trending structures (Figure 2.16c), with some NE-SW structures found as well. Some of the structures within the dark terrain may be related to impact generated furrow structures. The orientation of structures in the light terrain (domains 4 – 6) ranges widely, although bounding structures of the inferred fault duplexes (Figure 2.16b, thick black lines) trend primarily NW-SE, similar to those in dark terrain, suggesting inheritance of structural trends.

We infer two main stages of deformation in the Transitional Terrain (Figure 2.16d): (Stage I) NW-SE extension and formation of grabens within the dark terrain of domain 1. Slip tendency analysis suggests a principal stress orientation of $\sigma_1 = 60° – 80°$ provides the best match to these observations (Supplementary Figure 9), though it is important to note uncertainty may be introduced if many of the structures within domain 1 are related to impact processes; (Stage II) counterclockwise rotation of the principal stresses about a vertical axis allowing for N-S

extension and normal faulting of the central fault duplex, as well as left-lateral shearing of both the central and outer duplex along the antithetic shear axis. Slip tendency analysis suggests a principal stress orientation of σ_1 = 80° – 90° provides the best match to these observations (Supplementary Figure 9).

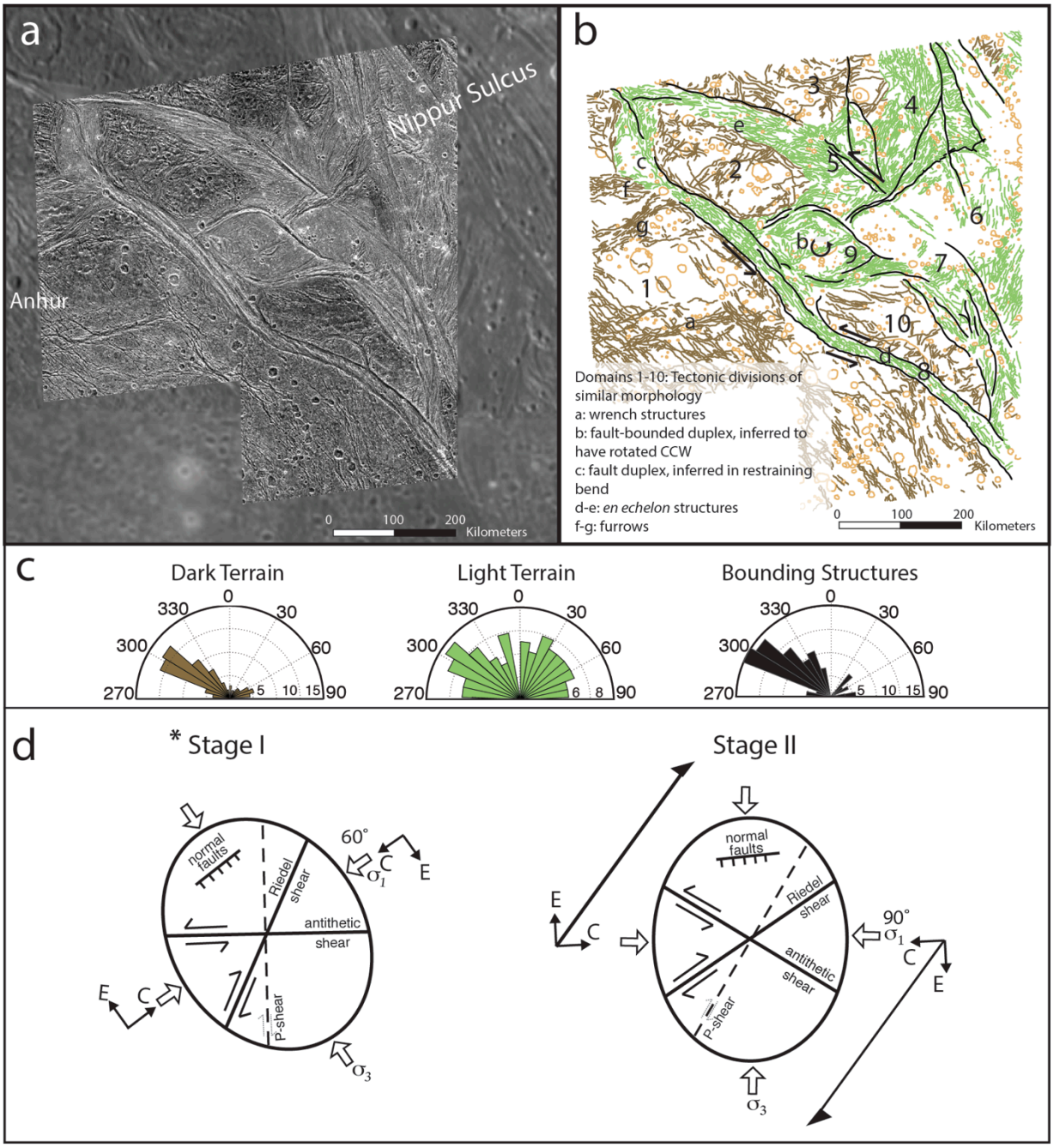

Figure 2.16: Transitional Terrain: (a) Voyager background imagery underlying Galileo high-resolution imagery, (b) lineament map, with letters and numbers referred to in the text, (c) rose diagrams (by length), and (d) diagrammatic strain ellipses. *Asterisk denotes uncertainty in principal stress orientations due to prominent furrows that may be impact related structures.

6. Discussion

When considering the complexity of Ganymede's heavily fractured surface, mapping domains that are based on regions of similar morphology help illustrate interactions between dark and bright terrain and to infer the history of geologic events. The formation and subsequent deformation of the most pristine grooved terrains tends to be associated with the most recent events. In some regions, like the Transitional Terrain area, grabens within the dark terrain share similar orientations to the light terrain, and duplex characteristics within the light terrain are likely associated with strike-slip (Figure 2.16 b, d). The mechanism for how the transition from dark to light terrain occurs is not well understood. Possible explanations point to tectonic modification of dark terrain, ultimately causing it to become more heavily fractured and brightened with time, perhaps due to tectonism exposing ice-rich, high albedo material (Head et al., 1998; Pappalardo et al., 2004). Extensional processes such as horst-and-graben, tilt-block or domino-style faulting are likely fundamental to this (Collins et al., 1998b, Pappalardo et al., 2004). A strike-slip strain component may also influence terrains during these processes, especially with increased lateral offset.

Detailed morphological mapping of these nine intriguing sites suggests strike-slip tectonism at both large and small scales may have played a key role in the development of Ganymede's complex surface terrain. At least one, if not more, of the four strike-slip morphological indicators (*en echelon* fractures, strike-slip duplexes, offset markers, and strained craters) are observed at each of these sites (Table 2.3). *En echelon* structures, indicative of the lowest amount of shear strain (Tchalenko, 1970; Naylor et al., 1986), are the most prevalent strike-slip structure and are found in every site examined here. Byblus Sulcus is the only mapped region where the presence of strike-slip indicators is limited to only a few *en echelon* structures, while every other mapped site displays examples of at least two types of strike-slip indicators, and the Arbela Sulcus site contains candidate examples of all four. The widespread presence of these indicators suggests strike-slip tectonism is indeed important to Ganymede's morphological history and evolution.

Inspection of rose diagrams and strain ellipses of each mapped site also suggests that trends exist in the orientations of features mapped within light terrain domains, with many regions exhibiting a predominant NW-SE orientation for light terrain domains (Table 2.3). Within the

mapped sites, only the light terrain of Arbela Sulcus exhibits a dominant NE-SW orientation, while Dardanus Sulcus and the Transitional Terrain do not seem to show any preference for structural orientation of light terrain. Regions that share similarities of light terrain orientation are also linked by geographic proximity, considering that many of these sites are within 50° latitude and 30° longitude of each other within the anti-Jovian hemisphere.

Analysis of regional slip tendency also permits a comparison of total inferred rotation and direction of each site (Table 2.3). Figure 2.17 provides a synthesis of these results, presenting the most plausible principal stress orientations acting within the local deformation stages at each of the nine sites. Dardanus, Arbela, and Nun Sulcus all lie within the sub-Jovian hemisphere and may have experienced 30 – 70° of counterclockwise rotation between the two main stages of local deformation. In the anti-Jovian hemisphere, many sites share roughly the same principal extension directions across three main stages of local deformation. For example, Nippur/Philus, Byblus, and Tiamat Sulcus all have inferred principal stress orientations of 60° for Stage I, and 140 – 160° for Stage III, yielding 80 – 100° of total inferred clockwise rotation of the principal stresses about a vertical axis. We also note that while Anshar, Byblus Sulcus, and Transitional Terrain do not have all three corresponding deformation stages (dashed boxes in Figure 2.17c), their associated principal stress orientations are placed within the most appropriate stage panel based on regional stratigraphic relationships. Uruk and Anshar Sulcus (within 18° latitude and 30° longitude from each other) behave differently than the other sites within the anti-Jovian hemisphere; examination of principal stress orientations suggest that they both experienced between 20 – 40° of total inferred counterclockwise rotation of the principal stresses between Stage I and Stage III.

These similarities in principal stress orientations and inferred direction and amount of rotation based on slip tendency analyses, coupled with the dominant NW-SE trend of light terrain, suggest there may be a connection between the orientation of the principal stresses and the emplacement of light material on a global scale. These observations and inferences may be important for understanding the relationship between dark and light terrain, given that stratigraphic relationships between dark terrain and grooved terrain imply an evolutionary sequence in which the dark terrain is heavily fractured and becomes brighter with time (Collins et al., 1998b; Prockter et al., 2000). A companion study is already underway to investigate the

role of tidal stresses on Ganymede in the formation and evolution of strike-slip structures in both dark and grooved terrains (Cameron et al., 2018), where priority consideration is being given to tidal stress scenarios that explore Ganymede's variability in eccentricity. Showman and Malhotra (1997) showed that Ganymede's eccentricity (presently ≈0.0013) once could have been altered by Laplace-like resonances among Ganymede, Europa, and Io to as high as ~0.05 (depending on the past ratio of tidal dissipation between Ganymede and Jupiter). Diurnal stresses during a past period of high eccentricity could have been significant, and could have played an important role in triggering and controlling faulting on Ganymede during its period of tectonic activity (Nimmo et al., 2002).

Table 2.3: Strike-slip indicators within mapped Ganymede sites: **E* - *En echelon* structures; D - Strike-slip duplexes; O - Offset features; Sc - Strained craters. Check marks indicate presence of strike-slip indicators, double check marks indicate the region displays numerous examples, and question marks indicate uncertainty. Hemisphere location*: T – trailing; L – leading; SJ – Sub-Jovian; AJ – Anti-Jovian. The remaining columns display dominant orientation of mapped features within the light terrain at each site, and total magnitude and direction of assumed rotation through time.

Site name	Presence of strike slip indicators *				Hemisphere location *	Dominant orientation of light terrain domains	Inferred total rotation and direction
	E	D	O	Sc			
Nun Sulci	✓		**?**	✓	T, SJ	NW-SE	70°CCW
Dardanus Sulcus	✓		✓		L, SJ	none	40° CCW/ 20°CW
Tiamat Sulcus	✓		✓		T, AJ	NW-SE	100° CW
Uruk Sulcus	✓	?			L, AJ	NNW-SSE	40° CCW
Arbela Sulcus	✓	✓	✓	✓✓	T, SJ	NE-SW	30° CCW
Nippur/Philus Sulci	✓			✓	T, AJ	NW-SE	90°CW
Byblus Sulcus	✓	?			T, AJ	NW-SE	80°CW
Anshar Sulcus	✓			✓	T, AJ	NW-SE	20° CCW
Transitional Terrain	✓	✓✓			T, AJ	none	30° CW

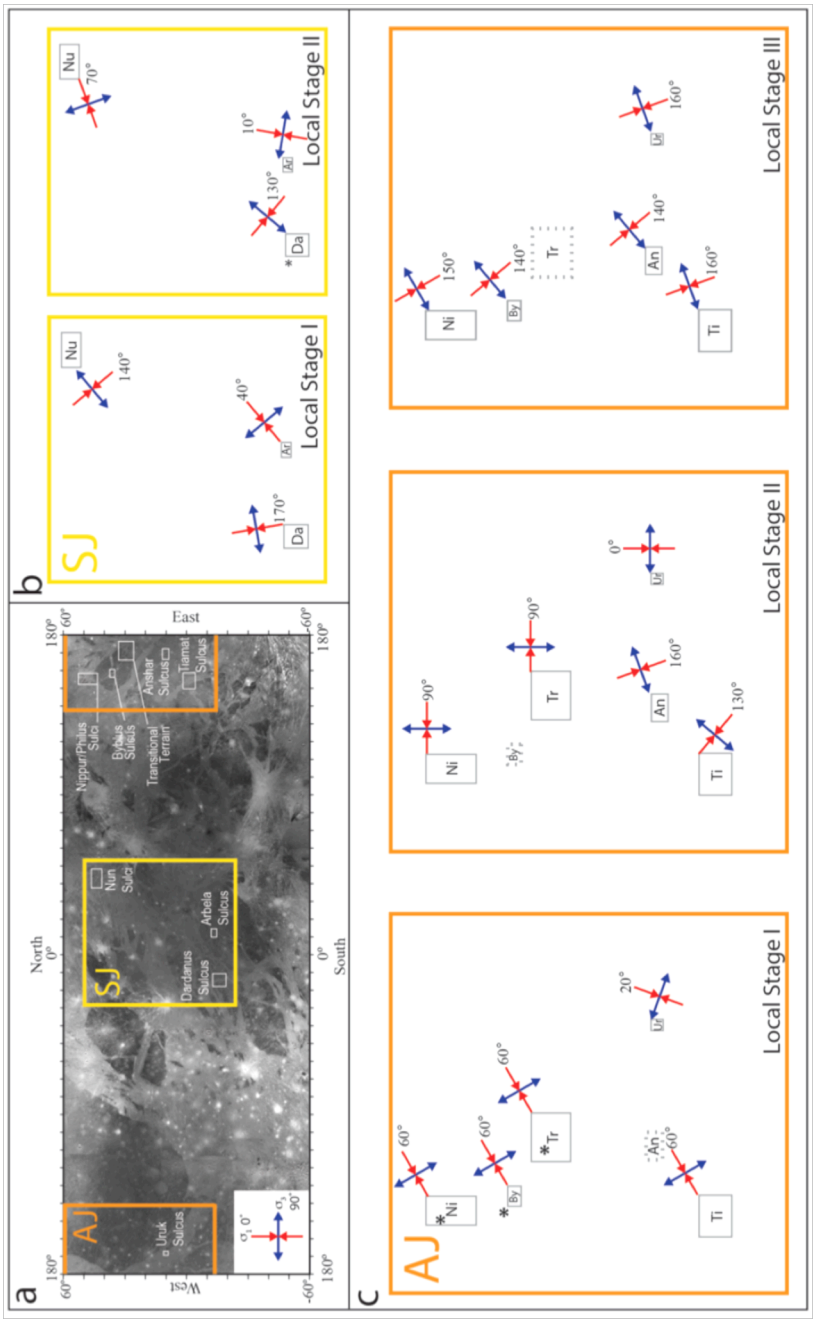

Figure 2.17: Local stress evolutionary sequence: (a) Ganymede global mosaic (0° – 360° E; 60°S - 60°N) in Mercator projection. Small, labeled boxes denote sites mapped in this study; large boxes labeled SJ (Sub-Jovian) and AJ (Anti-Jovian) refer to zoomed in region shown in (b) and (c). Bottom left inset shows a representative symbol denoting principal stress axes orientation, with σ_1 (red) and σ_3 (blue) being defined as the most and least compressive horizontal stress, respectively. (b) The most plausible principal stress orientation of the local deformation stages within each mapped site in the Sub-Jovian hemisphere. Numbers indicate the orientation of σ_1 in degrees from North. *Due to difficulty in determining age relationships within Dardanus Sulcus Stage II, labels i-ii represent orientations based on two different possible domain groupings; (c) Same as (b), but for the Anti-Jovian hemisphere. Dashed boxes indicate regions that do not have a corresponding deformation stages.

7. Conclusions

In this study, we explore the role of strike-slip tectonism in shaping Ganymede's terrain by performing detailed morphological mapping of *Galileo* high-resolution imagery set within lower resolution *Galileo* and *Voyager* image context. Where applicable, the presence of strike-slip indicators is available for download as an ArcGIS map package (Cameron et al., 2018d, Mendeley dataset), providing additional context for investigation of inferred sense of slip and tectonic evolution of Ganymede's fractures. We utilize rose diagrams, slip tendency, and strain ellipse methods to infer and interpret relationships between and among tectonic domains of similar morphology.

We find that examples of strike-slip faulting on Ganymede are ubiquitous, with representative strike-slip indicators identified at every examined site, and in both terrain types. Strike-slip tectonism may play a role in the transition between dark and light terrain, perhaps by exposing fresh, high albedo ice. While caution must be taken not to attribute morphology solely to strike-slip processes, we find that by incorporating strike-slip tectonism with previous inferences of extensional-tectonic behavior, we gain a more complete view of Ganymede's tectonic history. We also find that the mapped sites share similarities with each other, both in the occurrence of strike-slip indicators and in the stages of deformation when comparing neighboring regions. These correlations may allow for inferences about the effects of a shifting stress field through time from a local to global scale. Future work aims to further study the principal stress directions that could have acted at the regional or global scale to produce Ganymede's grooved terrain, and to examine plausible stress mechanisms (such as tidal stresses and nonsynchronous rotation) that support the development of observed tectonic features from detailed mapping.

Acknowledgements

We thank D. Alex Patthoff, S. Martel, P. Lucey, S. Fagents, and P. Mouginis-Mark for constructive conversations that helped clarify this manuscript. We also thank Lindsay DeRemer Keener for her work identifying the morphological indicators of strike-slip faulting used as a basis in this study. We appreciate the careful review offered by Scott Murchie and an anonymous

reviewer. The portion of this research by R.T.P. was carried out at the Jet Propulsion Laboratory, California Institute of Technology, under a contract with the National Aeronautics and Space Administration. This research was supported by the NASA Outer Planets Research Program (NNX14AE15G).

Author Contributions

M.C. performed the image processing and georeferencing of all images used in the study. M.C. digitized two regions and directed L.B. on digitization of six regions. F.S. digitized one region while at NASA JPL. M.C. interpreted all nine regions with the consultation of B.S.K., G.C., and R.P.. Four images were provided by R.P., but M.C. created all others. G.C. assisted M.C. with slip tendency method. M.C. wrote the manuscript with consultation from B.S.K, G.C., and R.P..

Supplementary Figure 1-9: Plausible orientations of the principal stress axes for domains within each of the nine sites, subpanels a-c correspond to their respective deformation stages (Stages I-III). An orientation is considered plausible if features with morphological strike-slip indicators undergo the correct sense of slip, and if contemporaneous features interpreted as graben or normal fault sets are slipping as normal faults. A sample principal stress orientation diagram is shown with σ_3 arrows pointing out, and σ_1 arrows pointing in to help distinguish between the two. Note: Features were mapped in Mercator projection, but are displayed here in x-y projection rather than Mercator, accounting for some of the differences in appearance.

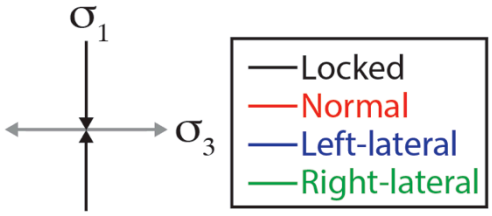

Figure 1: Nun Sulci

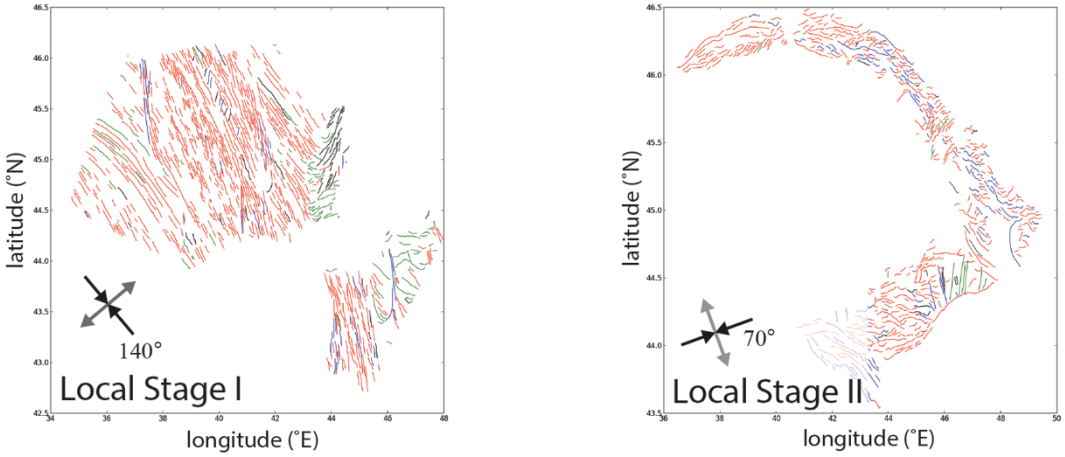

Figure 2: Dardanus Sulcus

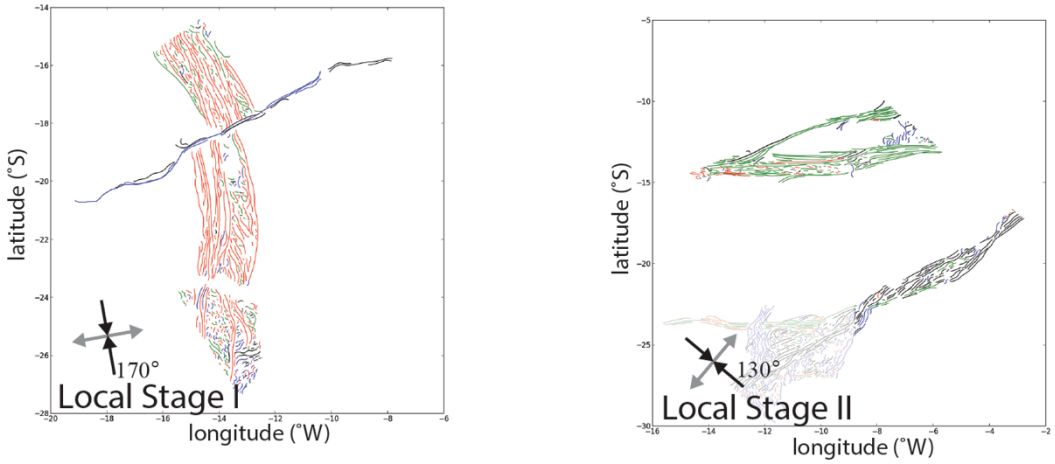

Supplementary Figures, continued

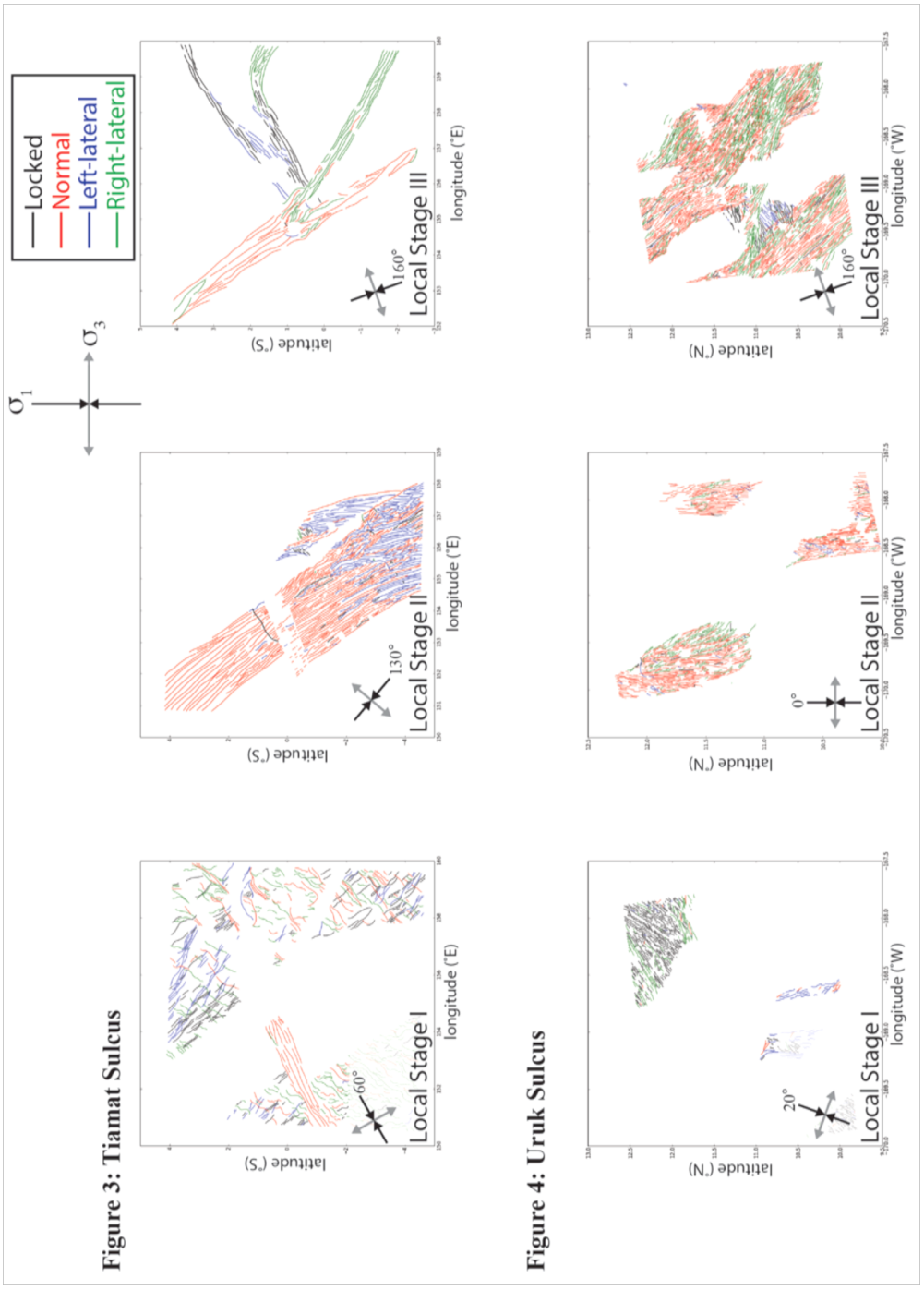

Figure 3: Tiamat Sulcus

Figure 4: Uruk Sulcus

Supplementary Figures, continued

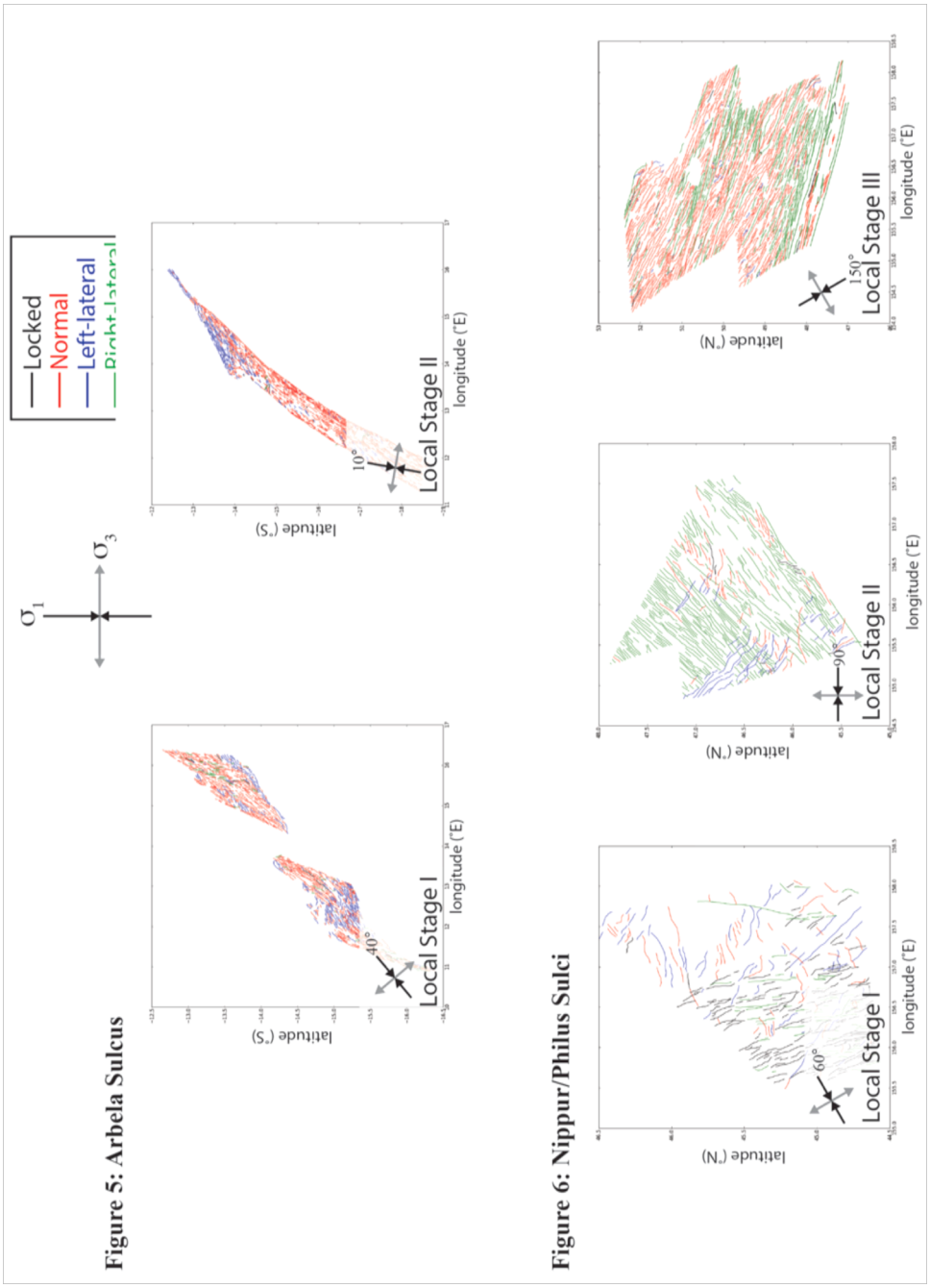

Figure 5: Arbela Sulcus

Figure 6: Nippur/Philus Sulci

Supplementary Figure 1, continued

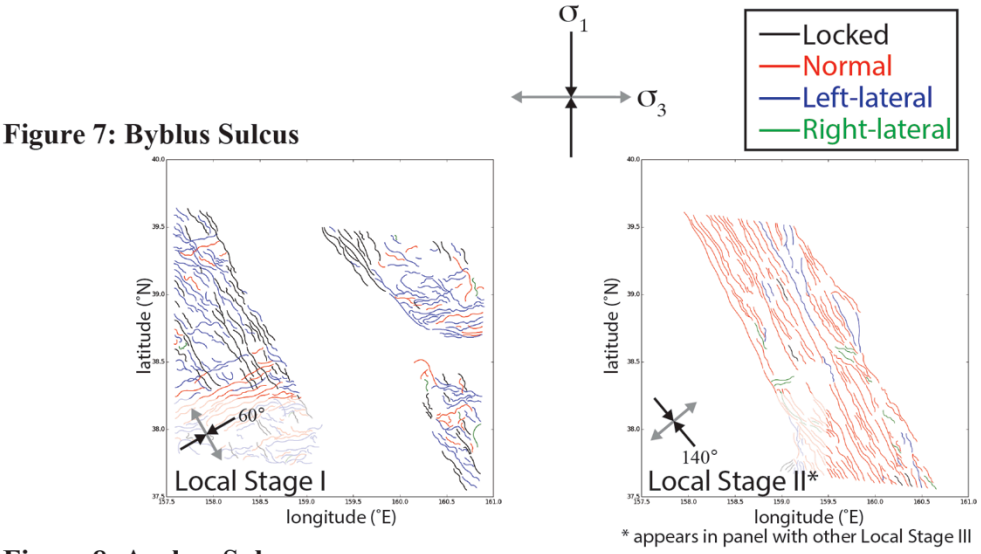

Figure 7: Byblus Sulcus

Figure 8: Anshar Sulcus

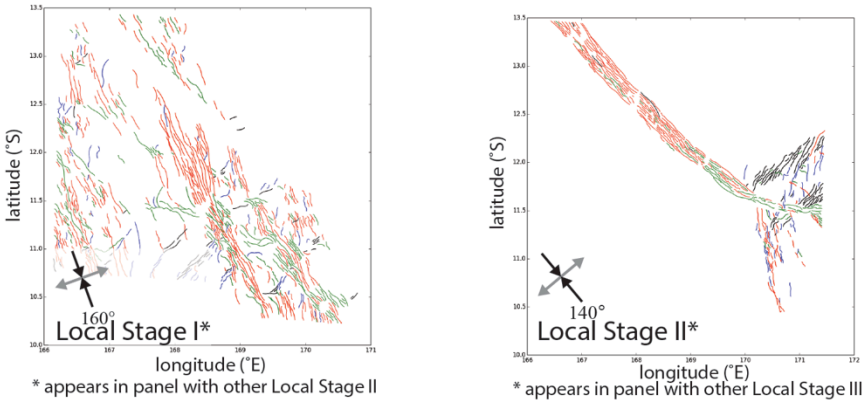

Fifure 9: Transitional Terrain

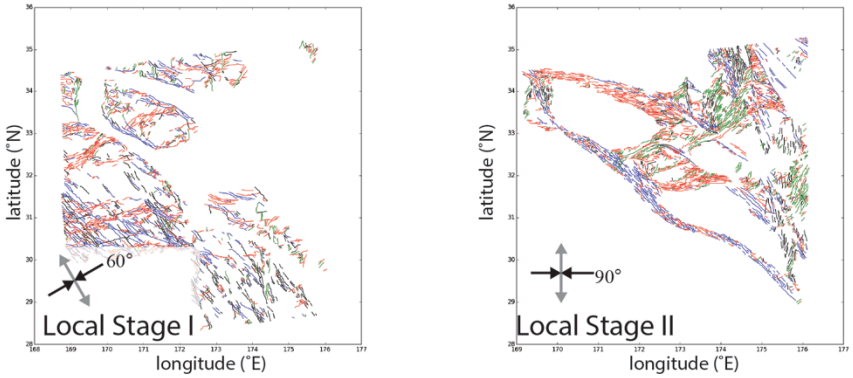

Supplementary Figure 10: Higher resolution images of key strike-slip morphological indicators at each of the nine regions studied. Letter labels refer to each region's main text imagery.

Nun Sulci

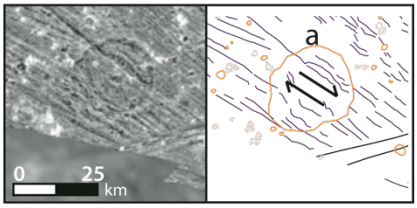

Dardanus Sulcus

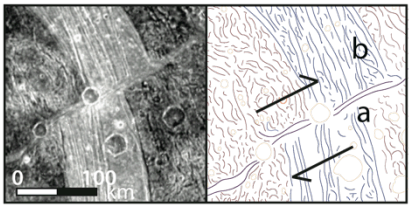

Tiamat Sulcus

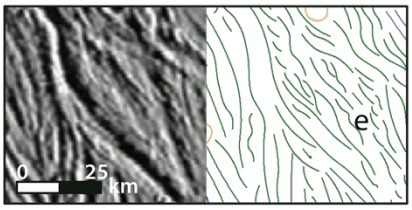

Uruk Sulcus

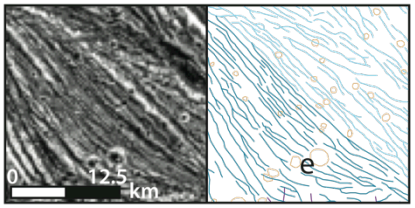

Arbela Sulcus

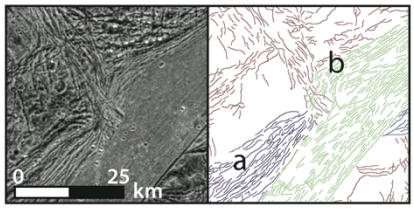

Nippur/Philus Sulci

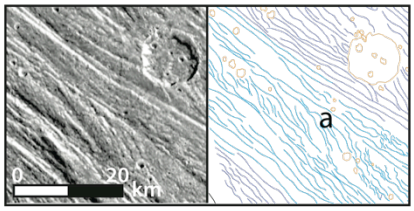

Byblus Sulcus

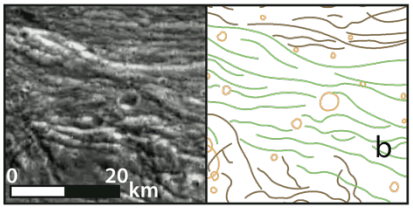

Anshar Sulcus

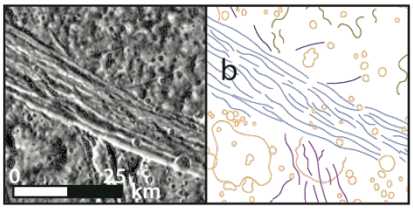

Transitional Terrain

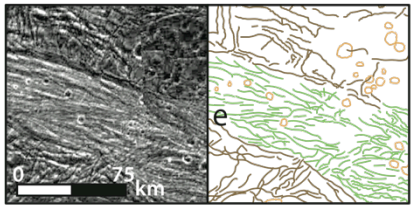

CHAPTER 3. TIDAL STRESS MODELING OF GANYMEDE: STRIKE-SLIP TECTONISM AND COULOMB FAILURE

Marissa Cameron[1], Bridget Smith-Konter[1], Geoffrey C. Collins[2], Donald A. Patthoff[3], and Robert T. Pappalardo[4]

[1]*Department of Geology and Geophysics, University of Hawai'i at Mānoa, Honolulu, HI 96822*

[2]*Physics and Astronomy Department, Wheaton College, Norton, MA, 027663*

[3]*Planetary Science Institute, apatthoff@psi.edu*

[4]*Jet Propulsion Laboratory, California Institute of Technology, Pasadena, CA 91109*

[*] Corresponding author: mecamero@hawaii.edu

Abstract

High-resolution Galileo data from Ganymede's complex surface provide strong and ubiquitous evidence of strike-slip faulting: *en echelon* structures, strike-slip duplexes, laterally offset pre-existing features, and strained craters. In a previous study, we mapped in detail strike-slip morphologies within nine regions on Ganymede: Dardanus Sulcus, Tiamat Sulcus, Nun Sulci, Byblus Sulcus, Nippur and Philus Sulci, the Transitional Terrain of Northern Marius Regio, Anshar Sulcus, Arbela Sulcus, and Uruk Sulcus. We also find evidence of normal faulting at each site. However, the prominence of strike-slip indicators suggests that strike-slip faulting has played an important role in the structural development of Ganymede's surface. Moreover, tidal stresses on Ganymede, under particular circumstances, may have been sufficient to induce Coulomb failure and strike-slip faulting. Here we investigate the role of both diurnal and nonsynchronous rotation (NSR) tidal stresses on Ganymede using the numerical code SatStress. We resolve normal and shear tractions onto discrete fault segments of specified orientation and assess Coulomb failure potential for the nine regions. Testing a range of subsurface fault depths (z = 0-5 km) and ice friction coefficients (μ_f = 0.2-0.6), we find that tidal stress models of combined diurnal and NSR stress readily promote Coulomb failure within each studied fault zone. High friction (μ_f = 0.6) limits failure depths to ~1 km, while low friction (μ_f = 0.2) extends failure depths to ~2 km, consistent with elastic thickness estimates. We also compare each fault zone's predicted slip sense to the slip sense inferred from our structural mapping efforts and find compatible senses of shear among six of the nine regions that exhibit notable fault offset and/or other strong evidence of strike-slip faulting. In addition, principal stress orientations and failure feasibility computed on a global scale suggest that combined diurnal and NSR tidal stresses promote Coulomb failure within the shallow (< 2 km) icy lithosphere across much of Ganymede. Coulomb failure is restricted near the equator by large compressive NSR stresses, but stresses at mid- to high-latitudes readily promote Coulomb failure along a wide range of fault orientations. Based on these results, we infer that nonsynchronous rotation may have assisted the formation and evolution of strike-slip structures on Ganymede.

Submitted to Icarus and currently under review.

1. Introduction

Observations by *Voyager* and *Galileo* of Ganymede, the largest of Jupiter's four Galilean moons (~5260 km in diameter), revealed a surface of extensively fractured and distinct dark and grooved terrains. High-resolution imagery provides evidence of both normal and strike-slip faulted structures (Collins et al., 1998; Pappalardo et al., 1998; Patel et al., 1999; DeRemer and Pappalardo, 2003; Pappalardo et al., 2004; Pappalardo and Collins, 2005). Previous investigations of these structures focused on the mechanisms for extensional tectonism (Collins et al., 1998; Pappalardo et al., 2004; Pizzi et al., 2017), however a recent global study of the morphological expression of strike-slip tectonism (Cameron et al., 2017) found that examples of strike-slip faulting on Ganymede are ubiquitous; representative strike-slip indicators, such as distinct offsets, *en echelon* structures, and strained craters were identified at nine examined sites. Furthermore, detailed morphological mapping of these nine sites suggests that strike-slip tectonism, which is visible at both large and small scales, may have played a key role in the development of Ganymede's complex surface terrain (Figure 3.1).

Previous studies suggest tectonic fractures on icy satellites result from gravitational tidal stresses (as at Europa; Helfenstein and Parmentier, 1985; McEwen, 1986; Leith and McKinnon, 1996; Geissler et al., 1998; Greenberg et al., 1998; Hoppa et al., 1999; Figueredo and Greeley, 2000; Kattenhorn, 2002; Spaun et al., 2003; Schenk et al., 2008, Rhoden et al., 2010). As Ganymede orbits Jupiter every 171.6 hours (Figure 3.2), variations in gravitational tidal forces, due in part to the satellite's eccentric orbit, act to deform the satellite (Greenberg et al., 1998). Nonsynchronous rotation stresses (NSR) may also arise if a tidally flexed satellite like Ganymede has an outer icy shell that is decoupled from its interior (Ojakangas and Stevenson, 1989) by a global liquid layer. As the outer shell rotates, the surface migrates eastward relative to the tidal bulge, and this can result in an additional source of stress within the icy shell. Both of these stressing mechanisms have been linked to the formation of both extensional and strike-slip tectonic structures on other moons, such as Ganymede's neighbor, Europa, and Saturn's moon Enceladus, (Showman and Malhotra, 1997; Greenberg et al., 1998; Hoppa et al., 1999; Nimmo and Gaidos, 2002; Nimmo et al., 2007; Smith-Konter and

Pappalardo, 2008; Olgin et al., 2011) and tidal stresses probably are the catalyst for faulting on Ganymede (Greenberg et al., 1998; Hurford et al., 2007; Collins, 2009).

Given that the surface of Ganymede displays several candidate regions of strike-slip tectonism, with shear failure presumably driven by a combination of global and local stress sources, a variety of questions arise: Can we identify a dominant mechanism for driving strike-slip tectonism on Ganymede? Are simulations of tidal stress able to explain the expression, distribution, and orientation of strike-slip structures on Ganymede? What plausible sets of conditions (i.e., normal and shear traction magnitudes, fault orientation and depth, coefficient of ice friction) permit strike-slip faulting on Ganymede?

To better illuminate the temporal and spatial variability of tidal stresses on Ganymede, as well as the implications for strike-slip tectonism from these stresses, we investigate the relationship between shear and normal tractions resolved onto fault structures in nine target regions (Figure 3.1): Dardanus Sulcus, Tiamat Sulcus, Nun Sulci, Byblus Sulcus, Nippur/Philus Sulci, Transitional Terrain, Anshar Sulcus, Arbela Sulcus, and Uruk Sulcus. In this paper, we first provide a brief background of Ganymede's geologic history, including the two main types of geologic terrains that dominate the surface and the previous work aimed at identifying key strike-slip morphologies of these terrains (Section 2). We also review possible tidal stress mechanisms and introduce the numerical model SatStress (Wahr et al., 2009) used to calculate both diurnal and NSR tidal stresses at Ganymede's surface (Section 3). We describe our method for resolving tidal stress components on an existing fault plane and for calculating shear failure based on the Coulomb failure criterion (Section 4). We present candidate regions for Coulomb failure for each target region and consider a range of plausible friction coefficients and brittle fault depths, and evaluate how failure estimates vary as a function of depth, ice friction, geographic location, and fault geometry (Section 5). Finally, we synthesize these results from a regional to global perspective, and include an analysis of the role of tidal stresses as a driver for strike-slip tectonism (Section 6). The ultimate goal of this work is to reconcile observations of strike-slip tectonism with comprehensive mechanical models of Ganymede tectonics.

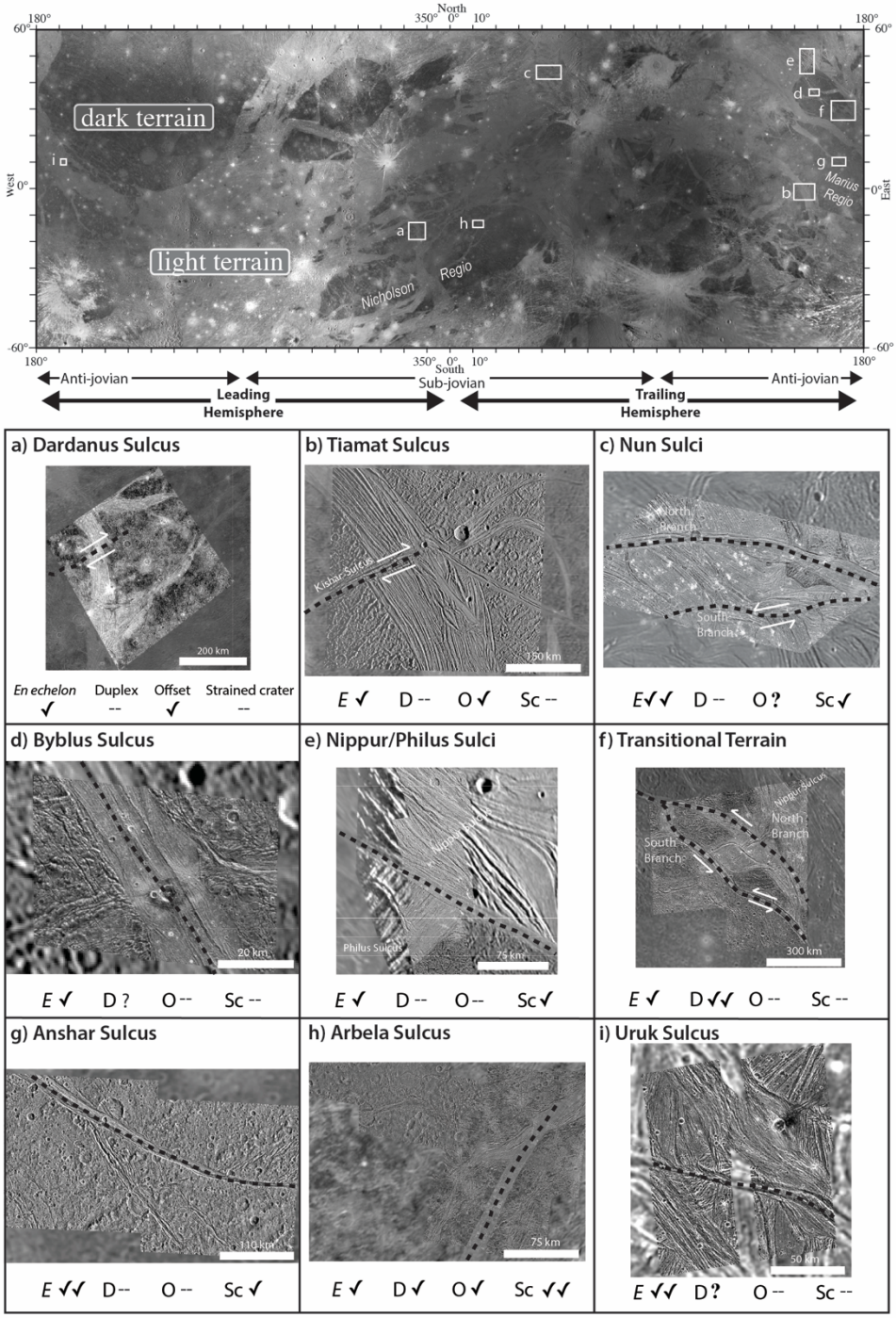

Figure 3.1. Regions of strike-slip tectonism on Ganymede. (Top) Ganymede global mosaic (0° – 360° E; 60°S - 60°N) in Mercator projection (modified from Cameron et al., 2017). Examples of dark and light terrain are labeled; labeled boxes denote sites where inferred fault zones were mapped for this study. (Bottom, a-i) Example *Galileo* imagery and inferred fault zones (black dashed lines). White half arrows indicate inferred sense of shear. Strike-slip indicators within mapped Ganymede sites are also labeled: **E* - *En echelon* structures; D - Strike-slip duplexes; O - Offset features; Sc - Strained craters. Check marks indicate presence of strike-slip indicators, double check marks indicate that the region displays numerous strike-slip indicators, and question marks indicate uncertainty.

2. Background

Twin spacecraft *Voyager* 1 and 2 imaged the Jupiter system in 1979, followed by the *Galileo* space probe that orbited Jupiter and imaged its moons between 1995 and 2003, providing improved surface imagery and geophysical data for exploring the internal and surficial structure of Ganymede. Initial interpretations of *Voyager* images were that most grooves are extensional tectonic structures (Shoemaker et al., 1982), and later *Galileo* images supported this interpretation (Belton et al., 1996, Pappalardo et al., 1998; Dombard and McKinnon, 2001; Bland and Showman, 2007). In addition, magnetic data from *Voyager* and *Galileo* provided evidence for an internally generated magnetic dipole on Ganymede, likely due to a molten iron core surrounded by a silicate rock mantle and an outer shell of ice (Anderson, 1996; Schubert et al., 1996, Sohl et al, 2002). In addition to an intrinsic magnetic field, an induced magnetic field was also inferred, suggesting the presence of a conductive layer inferred to be a subsurface liquid water ocean (Ojakangas and Stevenson, 1989; Kivelson et al., 1997; Carr et al*.,* 1998). The presence of a subsurface liquid water ocean has unique implications for the evolution of Ganymede's tectonic history and stressing mechanisms, particularly if the ocean layer acts as a decoupling interface. An outer ice I shell composed of a brittle near-surface layer and ductile interior is inferred to overlay the ocean. A separate ductile layer of higher pressure ice may lie below the subsurface ocean (Kivelson et al., 2002). The depths and thicknesses of these layers are not well constrained and may have changed over time (Showman and Malhtora, 1997).

Imagery from *Galileo* and *Voyager* reveals Ganymede's surface to be extensively fractured and composed of two distinct terrains, dark and light (grooved) terrain. Dark terrain covers about one-third of the moon and is characterized by an ancient, heavily cratered appearance (Shoemaker et al., 1982; Murchie et al., 1986, 1989; Neukum, 1997; Neukum et al., 1998; Prockter et al., 1998; Zahnle et al., 2003; Schenk et al., 2004). Much of the dark terrain is crosscut by systems of ~10 km wide furrows inferred to be remnants of large multi-ring structures (McKinnon and Melosh; 1980; Cassachia and Strom, 1984; Moore et al., 1998, 2001; Prockter et al., 2000; Pappalardo et al., 2004). Dark terrain is estimated to date from > 4 Gyr based on measured crater densities (Zahnle et al., 2003). Light (grooved)

terrain is younger and shows regions of extensive (extensional and strike-slip) tectonism. Crater density within the light terrain is 2 to 10 times less than in dark terrain, and light terrain is thus inferred to have been emplaced between 400 Myr and 4 Gyr ago. The large range in time reflects uncertainty in the impact flux (Zahnle et al., 1998; Neukum et al., 1998; Zahnle et al., 2003).

Nine mapped *Galileo* target sites of varying terrain types (Cameron et al., 2017) that show evidence of strike-slip faulting were used for this study to investigate strike-slip tectonism (Figure 3.1). Five of these sites are located primarily in light, grooved terrain (e.g. Nun Sulci, Dardanus Sulcus, Tiamat Sulcus, Uruk Sulcus and Arbela Sulcus); the remaining four sites occur within terrains transitional from dark to light terrain (e.g., Nippur/Philus Sulci, Byblus Sulcus, Anshar Sulcus, and the Transitional Terrain of Marius Regio). Sites also represent different hemispheric regions on Ganymede: trailing, leading, anti-Jovian, and sub-Jovian (see Figure 3.1). Previous work by Cameron et al. (2017) found similarities among the mapped sites, such as the presence of strike-slip indicators, the stages of deformation amongst neighboring regions, and the dominant orientation of light terrain within each site. These similarities may allow for inferences about the orientation of stress fields and the emplacement of light material on a global scale.

3. Tidal Stress Mechanisms and Modeling

Satellites commonly become synchronously locked to their parent planet, a behavior in which the same side of the satellite always faces the parent planet (Burns, 1976; Melosh, 1977; Helfenstein and Parmentier, 1980). This is due to the large tidal torques exerted by the parent planet (i.e., Jupiter) that allow for the spinning satellite to evolve into a synchronous configuration (Melosh, 1977; Peale, 1977, 1999; Helfenstein and Parmentier, 1980; Murray and Dermott, 1999). A synchronously rotating satellite will also experience a tidal bulge due to the difference in gravitational attraction of its parent planet. This tidal bulge is the cause of the ocean tides on Earth, where a bulge of water on either side of the Earth during “low tide” is observed on both sides of the planet. If the orbit of the satellite is elliptical (i.e., an eccentricity of greater than zero, and less than 1), the tidal bulge will vary in both magnitude

and longitudinal position as it changes distance from the parent planet during its diurnal orbit (Murray and Dermott, 1999). Therefore, gravitational stresses affect both orbital and rotational evolution of a satellite like Ganymede, and provide a mechanism for crustal deformation and a major source of heat (Peale, 2003).

As Ganymede orbits within Jupiter's gravitational field, the varying gravitational potential causes tidal stresses and deformation as portions of the satellite are subjected to gravitational effects (Wahr et al., 2009). Observed regions of strike-slip tectonism on Ganymede may be due, in part, to a combined effect of temporally varying stresses. Processes possibly impacted by tidal stress have been associated with the formation of global tectonic features on satellites and include reorientation of the ice shell relative to the spin axis (Melosh, 1975), tidal despinning (Melosh, 1977), radial and librational tides due to an eccentric orbit (Yoder, 1979; Greenberg et al., 1998), nonsynchronous rotation (NSR) (Helfenstein and Parmentier, 1985), orbital recession and precession (Squyres and Croft, 1986; Croft et al. 1995), and polar wander (Leith and McKinnon, 1996; Schenk et al., 2008). Effects of tidal stresses are well documented for Europa (i.e., Helfenstein and Parmentier, 1985; McEwen, 1986; Leith and McKinnon, 1996; Geissler et al., 1998; Greenberg et al., 1998; Hoppa et al., 1999; Figueredo and Greeley, 2000; Kattenhorn, 2002; Spaun et al., 2003; Schenk et al., 2008, Rhoden et al., 2010).

In this study, we focus on two primary mechanisms of tidal deformation: diurnal and nonsynchronous (NSR) stresses. As Ganymede orbits Jupiter, variable diurnal stresses sweep across the surface over a period equal to that of the satellite's orbital (diurnal) period, or 171.6 hours (Figure 3.2). Diurnal tidal stresses may be quite relevant to the formation of Ganymede's terrain; previous studies have suggested that diurnal tidal stresses are (1) responsible for the formation of Europa's ridges (Greenberg et al., 1998; Hoppa et al., 1999; Nimmo and Gaidos, 2002), and (2) may trigger geological activity along fractures of Enceladus (Showman and Malhotra, 1997; Hurford et al., 2007; Nimmo et al., 2007; Smith-Konter and Pappalardo, 2008; Olgin et al., 2011). Furthermore, NSR stresses may arise if a tidally flexed satellite has an outer icy shell that is decoupled from its interior (Helfenstein and Parmentier, 1985; Ojakangas and Stevenson, 1989), likely by a global liquid layer. As the outer shell rotates, the surface migrates eastward relative to the tidal bulge and can result

in an additional source of stress within the viscoelastic icy shell (Figure 3.2). Hoppa et al. (1999) compared *Voyager* and *Galileo* observations to constrain the present NSR period of Europa's ice shell to be > 10^4 yr. The period of NSR stresses could be on the order of the thermal diffusion timescale, or ~10^7 yrs (Ojakangas and Stevenson, 1989; Hoppa et al., 1999). Wahr et al. (2009) also considered a range of NSR periods (10^5 – 10^7) and their implications of global tidal stress variations. Nonsynchronous rotation may explain the lack of leading-trailing hemisphere crater asymmetry, a characteristic observed on satellites that are synchronously locked to their parent planet, such as Earth's Moon (Kawamura et al, 2011; Ito and Malhotra, 2010), Saturn's Triton (Strom et al., 1990; Schenk and Sobieszczyk, 1999), and the Galilean satellites (Zahnle et al. 1998, Morota and Furomoto, 2003). This asymmetry is caused in part by the leading side intercepting more impactors than the trailing side (Melosh, 2011). Additionally, the mean impact velocity on the leading side becomes higher than that on the trailing side; therefore, average crater sizes on the former tend to be larger than those on the latter. For these reasons, synchronous rotation can lead to a slight increase in the cratering rate on the leading side. In this study we adopt a NSR period of 1.42x10^5 yrs following Wahr et al. (2009).

To investigate tidal diurnal and NSR stresses on Ganymede, we utilize SatStress, a numerical code that calculates tidal stresses at any point on the surface of a satellite. SatStress (http://code.google.com/p/satstress) computes stresses based on tidal potential theory (e.g., Wahr, 1981, Wahr et al., 2009), allowing for both elastic and layered Maxwell viscoelastic treatments of the lithosphere. Table 3.1 describes the model parameters for a layered Ganymede adopted in this study, represented by a spherically symmetric ice shell underlain by a global subsurface ocean and a deep interior. We represent Ganymede's outer ice shell with two layers (Moore and Schubert, 2003; Wahr et al., 2009): (1) an upper rigid layer 10 km thick with a viscosity of 10^{19} Pa s, and (2) a more ductile ice shell extending another 140 km deep with a viscosity of 10^{14} Pa s. Beneath these ice layers, we assume a global 40 km thick liquid ocean. The deep interior is assumed to comprise the underlying mantle of high-pressure ice and the core of rock and metal, with a combined thickness of 2441 km and bulk density of 2184 kg/m^3. Degree-two Love numbers for this assumed rheology for both diurnal and NSR models were derived using a companion Love number

code available in the SatStress package (J. Wahr, personal communication, 2011) and were verified by alternative models (Moore and Schubert, 2003; F. Nimmo, personal communication, 2013).

Table 3.1: Ganymede physical, orbital and rheological model; SatStress input parameters.

Physical and Orbital Characteristics		
Satellite radius (km)	2630	
Satellite orbit eccentricity	0.0013	
Satellite orbit semi-major axis (km)	1.07×10^{6}	
Satellite gravity (m/s^2)	1.428	
Planet mass (kg)	1.90×10^{27}	

Viscoelastic Parameters		
Ice (Upper and Lower)		
Young's modulus (GPa)	9.30	
Shear modulus (GPa)	3.49	
Poisson's ratio	0.30	
Density (kg/m^3)	920	
	Upper ice layer	Lower ice layer
Thickness (km)	10	140
Viscosity (Pa s)	10^{19}	10^{14}
Ocean		
Young's modulus (GPa)	0	
Shear modulus (GPa)	0	
Poisson's ratio	0.50	
Density (kg/m^3)	1000	
Thickness (km)	40	
Viscosity (Pa s)	0	
Deep Interior (high-phase ice + silicates)		
	Diurnal	NSR
Young's modulus (GPa)	100	0
Shear modulus (GPa)	40	0
Poisson's ratio	0.25	0.50
Density (kg/m^3)	2184	2184
Thickness (km)	2441	2441
Viscosity (Pa s)	$\sim 10^{20}$	$\sim 10^{20}$

SatStress Parameters		
	Diurnal	NSR
Period (yrs)	1.42×10^{7}	1.42×10^{5}
Elastic love number h_2	1.427	
Real diurnal Love number h_2		1.427
Imaginary diurnal Love number h_2		-5.796×10^{-2}
Real NSR Love number h_2		1.962
Imaginary NSR Love number h_2		-5.704×10^{-4}
Elastic love number l_2	0.3641	
Real diurnal Love number l_2		0.3641
Imaginary diurnal Love number l_2		-1.981×10^{-2}
Real NSR Love number l_2		0.5123
Imaginary NSR Love number l_2		-5.372×10^{-4}

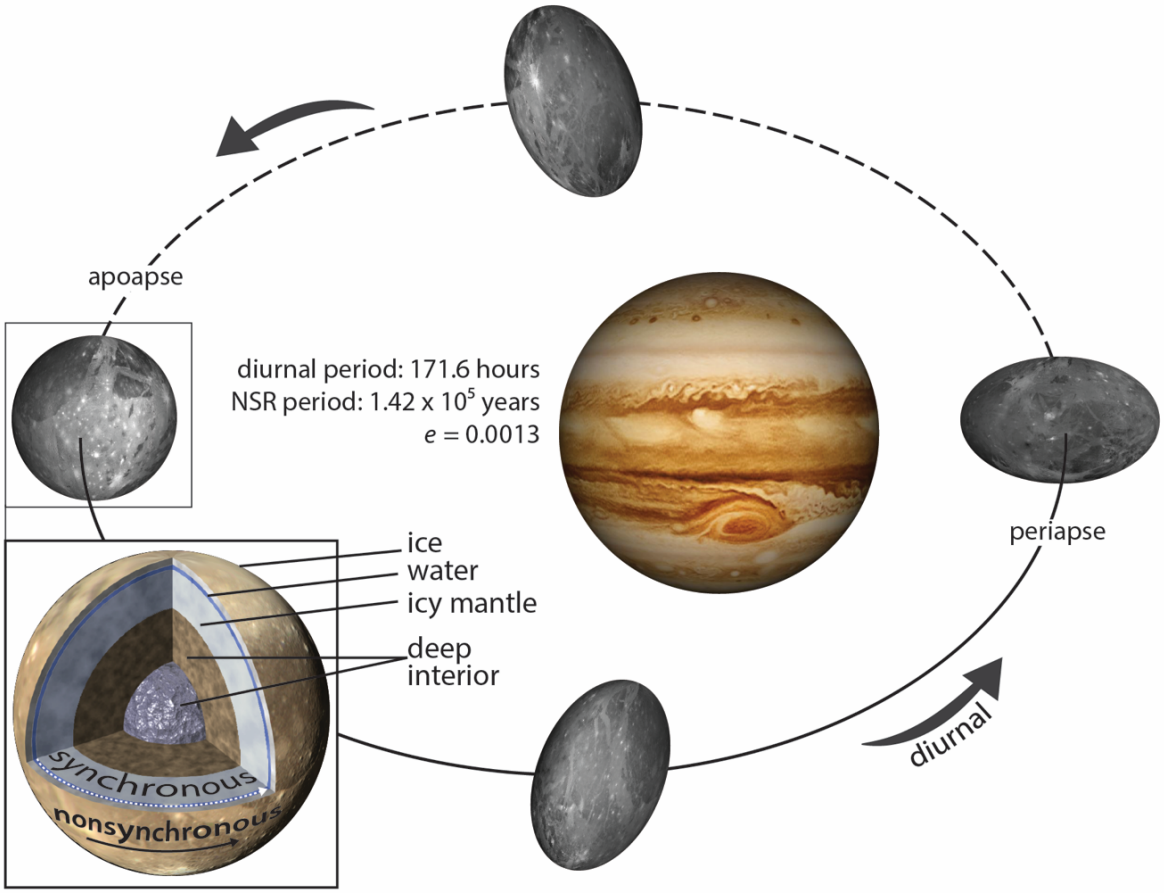

Figure 3.2. Tidal stress schematic. As Ganymede orbits Jupiter every 171.6 hours, variations in gravitational tidal stresses, due in part to the satellite's eccentric orbit (e = 0.0013), act to deform the moon's surface. Diurnal tidal stresses are on the order of kPa. Inset: Ganymede's internal structure consists of an outer ice layer ~150 km thick underlain by a thin ocean ~40 km deep, and a deep interior comprised of mantle and core material. Nonsynchronous rotation (NSR) stresses may arise if a tidally flexed satellite has an outer icy shell that is decoupled from its interior. As the outer shell rotates, the surface migrates eastward relative to the tidal bulge and can result in an additional source of stress within the viscoelastic icy shell. NSR rate may be ~10^5 years. NSR stresses are on the order of MPa.

SatStress computes both raw ($\sigma_{\varphi\varphi}$, $\sigma_{\theta\theta}$, $\sigma_{\theta\varphi}$ or latitudinal, longitudinal, and shear tractions, respectively) and diagonalized (principal) stress tensor components as a function of orbital position past periapse (i.e., the mean anomaly, m) and geographic location on the satellite. In this study we adopt a positive compressional stress sign convention to maintain consistency with our previous work. Subsequently, we apply a reverse color palette to provide a consistent visual comparison with other publications (i.e., Wahr et al., 2009). To demonstrate the behavior of Ganymede's predicted tidal stress field as a function of mean anomaly, we first plot the diurnal stresses at 90° mean anomaly intervals (Figure 3.3). The diurnal stress field provides stresses on the order of a few kPa and varies as a function of mean anomaly position, m. Moreover, inspection of the diurnal tidal stress model reveals that the most variation in stresses occurs with the $\sigma_{\theta\theta}$ (longitudinal) component (Figure 3.3b), with all nine studied fault zones subject to peak stresses of ~ +/-5 kPa throughout Ganymede's orbit. Additionally, the variability in diurnal maximum principal stresses (Figure 3.3a) is most significant in the central to mid-latitudes, where fault zones experience an exchange of peak compressive (~4 kPa) and tensile (~-4 kPa) stresses over an orbit.

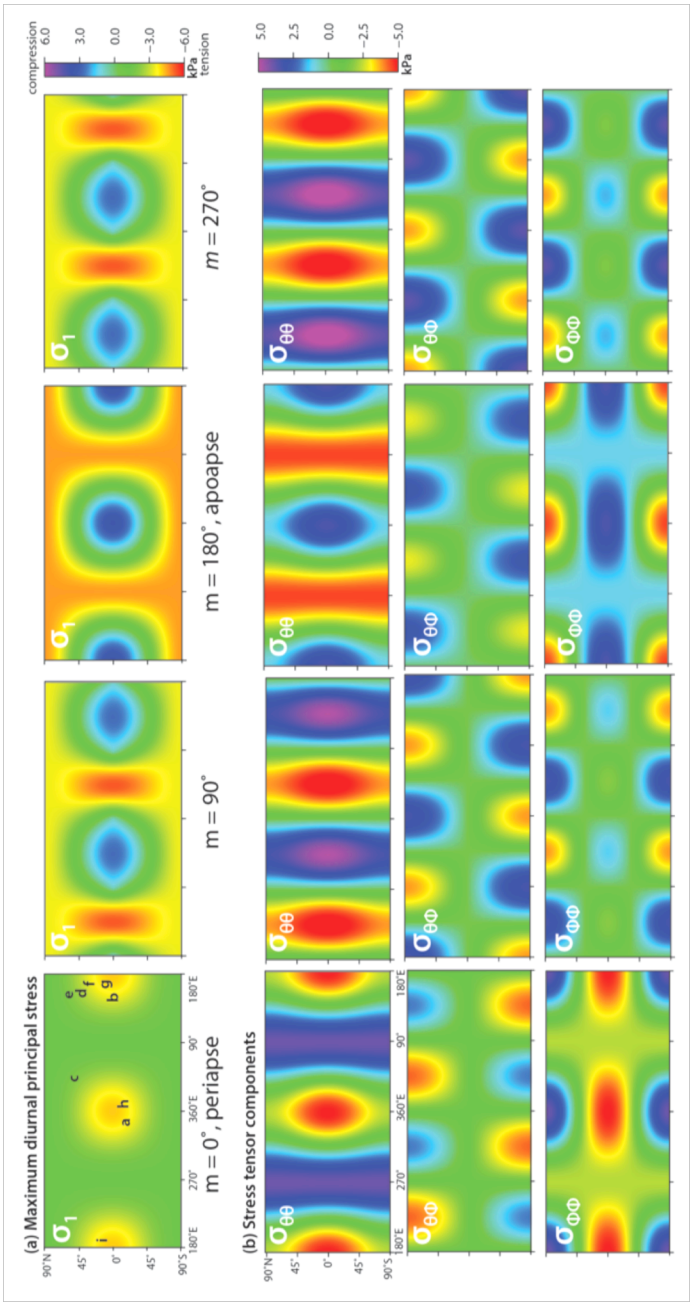

Figure 3.3. Global diurnal tidal stresses. (a) Maximum principal stress (s_1, kPa) at mean anomaly position m = 0°, 90°, 180°, and 270°. We adopt an inverted color palette to maintain visual consistency with previous studies: Negative (red) values indicate tensile stress, positive (purple) values indicate compressive stress. Letter labels a-i refer to locations of the nine strike-slip study regions of Figure 3.1. (b) Stress tensor components at anomaly position m = 0°, 90°, 180°, and 270°. Stress amplitudes are in kPa.

We next plot the combined diurnal and NSR tidal stress field (Figure 3.4) at periapse (m = 0°). The combined diurnal + NSR (which we will call diNSR) field is dominated by the large, secular NSR stresses within the ice shell. These stresses are on the order of MPa and have the largest absolute values in the central to mid-latitudes, as demonstrated by the large compressive principal stresses of Figure 3.4a. We also note that all but one of our studied sites (Nun Sulci, label c) is located within zones of large magnitude principal tensile stress. Moreover, while the diNSR stress field does vary slightly (~6 kPa) on a diurnal timescale, these variations are a very small, nearly indistinguishable fraction, of the total diNSR stress field. To demonstrate this effect, we plot the residual stress of the diNSR field (in kPa) at apoapse (m = 180°) with respect to the periapse (m = 0°) diNSR stress field (Figure 3.4b). Hence, with respect to the scope of this study, the dominant stress contribution of the diNSR model within an orbital period can largely be represented by a quasi-static MPa-order stress field. We note these particular stress contributions, as (1) subsequent figures reflect only the m = 0° diNSR stress field, which is a good approximation for the stress field at all mean anomaly positions, and (2) they are important for understanding large-scale variations in along-strike failure predicted by our models along several sections of the studied sulci, as described next in detail.

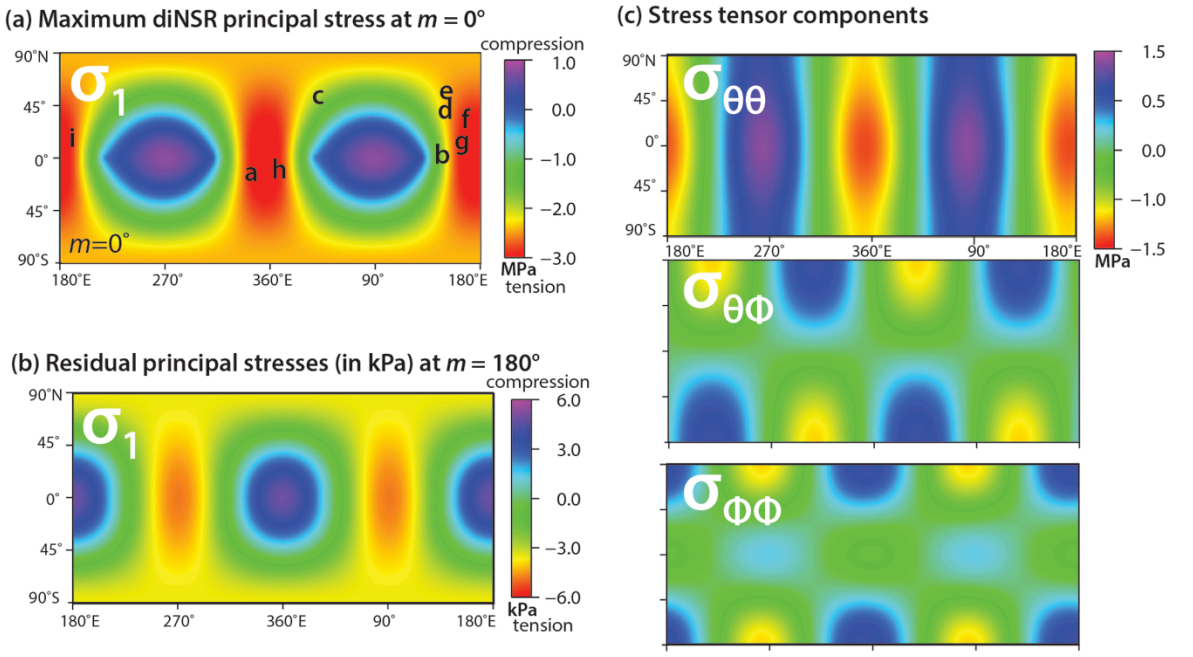

Figure 3.4. Global diNSR (diurnal + NSR) stresses: (a) Maximum principal stress (s_1, MPa) at mean anomaly m = 0°. (b) Residual s_1 stress at m = 0° and 180°, on the order of kPa, demonstrating the quasi-static nature of stresses once NSR is introduced. Negative values indicate tensile stress, positive values indicate compressive stress. (c) Stress tensor components at periapse (m = 0°). Note stress amplitudes are in MPa. This snapshot of the stress tensor is provided for m = 0°, however is nearly representative of all m positions.

4. Coulomb Failure

Coulomb failure theory accounts for a fault's frictional resistance to slip (e.g. Byerlee, 1978; Brace and Kohlstedt, 1980). Following the methodology of previous studies (Hurford et al., 2007; Nimmo et al., 2007; Smith-Konter and Pappalardo, 2008;), we resolve tidal stress tensor components onto discrete fault segments, of varying length and orientation, into normal (σ_n) and shear (τ_s) traction components:

$$\tau_s = \frac{1}{2}\left(\sigma_{\phi\phi} - \sigma_{\theta\theta}\right) sin2\beta + \sigma_{\theta\phi} cos2\beta$$

$$\sigma_n = \sigma_{\theta\theta} cos^2\beta + \sigma_{\phi\phi} sin^2\beta + \sigma_{\theta\phi} sin2\beta$$

(Eq. 1)

where β is a line segment trend, defined with respect to the longitudinal direction (β = 0° for a line segment due east-west). Where applicable, we adopted mapped feature traces (i.e., measured trend with assumed vertical dip) from Cameron et al. (2017); however, due to

sparse high-resolution imagery (commonly on the order of 10s m/pixel), we estimated fault geometry in some regions. Each sulcus is represented as a series of digitized fault segments with lengths of 5 km or less, and with orientations that may vary from the overall strike of the major fault zone. For each individual fault segment, the resolved normal traction component is defined as that acting perpendicular to each segment fault plane, while the resolved shear traction component is that acting parallel to each segment fault plane.

The Coulomb failure criterion (Byerlee, 1978; Jaeger and Cook, 1979) considers stresses that facilitate (tensile) and resist (compressive) slip along a fault, simultaneously accounting for both resolved normal and shear tidal traction, the coefficient of friction of ice, and stress at depth due to the overburden pressure (Thatcher and Hill, 1991). To model this behavior, we calculate the Coulomb stress as

$$\tau_c = |\tau_s| - \mu_f(\sigma_n + \rho g z), \qquad \text{(Eq. 2)}$$

where μ_f is the effective coefficient of friction and $\rho g z$ is the maximum overburden pressure (positive z is the vertical depth of the fault plane beneath the surface). Note that while the actual overburden pressure could be less than this, we assume the overburden pressure translates 1:1 to the lateral pressure acting on the fault. The sign of the overburden stress is taken to be positive, while normal tidal tractions are assumed positive when in compression and negative when in tension. The sign of the shear stress (positive for right-lateral, negative for left-lateral) becomes important when inferring the direction of slip where the failure conditions are met.

For simplicity, we will refer to the rightmost quantity of Eq. 2 that includes μ_f as the "frictional stress." Thus, for Coulomb failure to occur, the tidal shear traction on a fault must be greater than the frictional stress. Positive Coulomb stresses imply a fault would slip, while negative Coulomb stresses imply a locked fault. For compressive zones with no melting, no minimum fault depth limitation applies, as a fault interface will always be closed. Because the Coulomb criterion only applies for a closed fault interface, we evaluate the role of fault depth for both normal tensile and compression regimes separately. If the overburden stress is less than the tensile traction, a fault would dilate and the Coulomb failure criterion is not applicable. Using the z-depth dependence of overburden stress in this manner, we evaluate the depth sensitivity of Coulomb failure for each fault zone at 0.1 km discretized depth

observation planes.

Laboratory experiments on ice indicate $\mu_f = 0.1 – 0.7$ are applicable depending on sliding velocity, pressure, and temperature (Beeman et al., 1988; Fortt and Schulson, 2007; Schulson and Fortt, 2012). Previous studies (e.g., Nimmo and Gaidos, 2002; Nimmo et al., 2007; Olgin et al., 2011) have assumed a coefficient of friction appropriate to ice near its melting temperature ($\mu_f = 0.1 – 0.3$) for shear heating models on Europa and Enceladus. In this analysis, we consider a conservative range of friction coefficients ($\mu_f = 0.2 – 0.6$), consistent with both laboratory estimates of ice friction and previous studies by Schulson and Fortt (2012). We assume a constant frictional coefficient with depth within the shallow icy crust (0 – 5 km), and compare end-member models of high ($\mu_f = 0.6$) and low ($\mu_f = 0.2$) friction. To evaluate how Coulomb failure varies with depth, coefficient of friction, and fault orientation, we compare stresses within the ice to the stress required for Coulomb failure at each of the nine inferred strike-slip fault zones.

We note that the magnitude and sign of resolved normal and shear tractions of each fault segment are highly dependent on the β of the segment, or orientation with respect to the east-west direction. This local angle may vary considerably from segment to segment from the overall fault zone strike, as well as from nearby structures. Moreover, Coulomb failure stresses on nearby fault segments may vary significantly if the orientations of these structures significantly differ, in addition to the effects of a spatially varying stress field. To illustrate the dependency of both Coulomb failure and shear traction direction on β, we provide fault orientation dependency diagrams for a range of β (i.e., Hoppa et al., 1999; Rhoden et al., 2011) throughout this paper. An example diagram is provided for the location of Dardanus Sulcus (Figure 3.5). In this example, Equation 1 is used to compute the shear and normal tractions on faults for a range of β angles (β = 0-360°, at 10° intervals). Equation 2 is used to determine Coulomb stress, where a positive result indicates stresses that promote Coulomb failure, and a negative result indicates a locked fault; in this example case we assume $\mu_f = 0.2$ and $z = 1$ km.

In Figure 3.5a, the normal traction sign (positive for compression, negative for tension) for a range of segment orientations is illustrated; in this case all orientations experience a tensile traction. Figure 3.5b shows the sign of the shear stress (positive for right-lateral,

negative for left-lateral). For a fault plane with a β = 10° to 100°, shear tractions are negative (left-lateral). Alternatively, for fault planes with 100° < β < 190°, the resolved shear are positive (right-lateral). Figure 3.5c shows the Coulomb stress sign as a function of β, where planes favorably oriented to slip have positive Coulomb stresses, and planes that would not slip have negative Coulomb stresses. For example, for β = 120° to 260°, Coulomb stresses are positive the plane is predicted to slip. Alternatively, for 80° < β < 120°, the Coulomb stress would be negative and a fault would be locked. For simplicity, we note that only the sign of the quantity (normal and shear tractions, or Coulomb stress) is represented here, whereas the magnitude of both of these quantities will also smoothly vary with β. We use a binary color scheme to identify regions of positive or negative stress, but the function also varies smoothly from minimum magnitudes at the wedge boundaries (where colors switch from gray to black) to maximum magnitudes at each circle center (note, we do adopt a more complete representation of this behavior in subsequent figures, but we explore this simple diagram here to highlight a fundamental behavior). Moreover, a fault segment's resolved shear traction direction, and Coulomb failure tendency is strongly guided by its present-day orientation as captured by satellite imagery. We further explore the Coulomb failure tendency for each mapped sulcus in the subsequent sections.

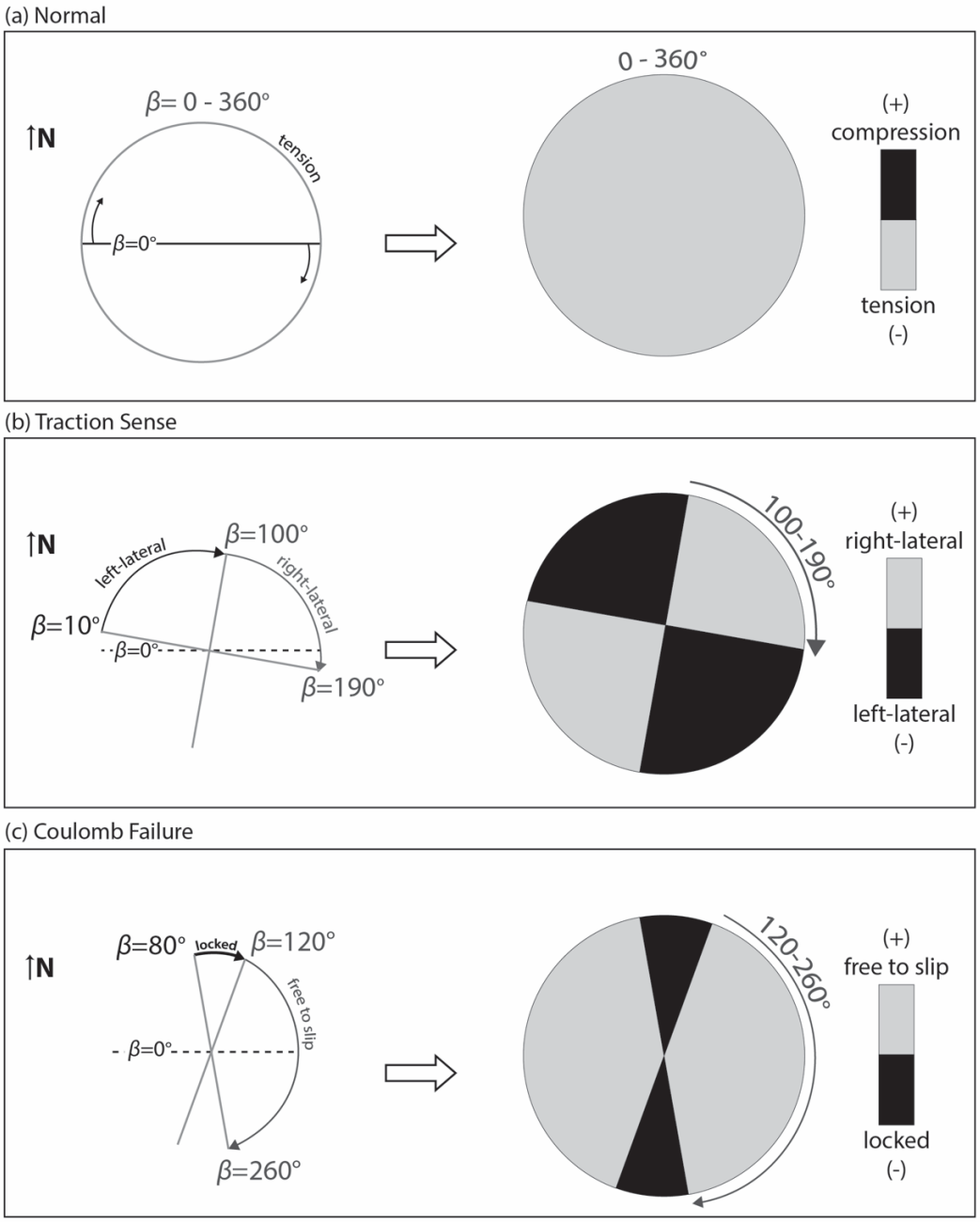

Figure 3.5. Fault orientation dependency diagrams, demonstrating the sign of resolved normal, shear and Coulomb stresses as a function of fault plane orientation. In this example, stresses from the Dardanus Sulcus region (Figure 3.1a; 340° to 345° E longitude, 22.5°S to 17.5°S) are used to demonstrate how ranges of fault strikes yield variable quantities for a depth of 1 km. (a) Normal traction orientation diagram, where fault plane orientations yielding positive normal traction (compression) is shaded black and negative normal traction (tension) is shaded gray. (b) Traction sense diagram, where fault plane orientations yielding positive shear traction is shaded gray (right-lateral) and negative shear traction (left-lateral) is shaded black. (c) Coulomb stress orientation diagram, where fault plane orientations yielding positive Coulomb stress is shaded gray (indicating orientations that promote slip, and fault plane orientations yielding negative Coulomb stress is shaded black (indicating orientations that inhibit slip).

5. Results

For completeness, we first evaluate the opportunity for Coulomb failure at each fault zone in response to diurnal tidal stresses alone and illustrate the results at 100 m depth assuming a low (μ_f = 0.2) coefficient of friction. Figure 3.6 shows the sinusoidal nature of the resolved normal and shear tractions over a complete diurnal cycle. Stresses peak at different mean anomaly positions depending on the geographic location of each fault zone. Additionally, while a diurnal sinusoid is calculated for every point along the length of the fault to accommodate the varying orientations along strike, the mean of the resulting diurnal sinusoids serves as a representation of average stress behavior and therefore is shown in Figure 3.6. If the shear traction (blue line), at any mean anomaly position *m,* exceeds the magnitude of the frictional stress (red dashed line), Coulomb failure is achieved. Our results indicate, however, that the stresses required for failure are approximately an order of magnitude larger than the modeled diurnal shear tractions, and therefore failure is not predicted. For example, at Dardanus Sulcus, the diurnal normal tractions (black line) are small (4.5 kPa) and compressive for *m* = 30-230° and then become small and tensile (-4.5 kPa) for *m* = 230-30°; shear tractions (blue line) are also small (<1 kPa) and left-lateral for *m* = 45-225° and right-lateral for *m* = 225-45°. The mean frictional stress (red line) for μ_f = 0.2 at 100 m depth is 28±1.5 kPa, which is nearly triple the magnitude of diurnal shear stress needed to drive failure. Hence, a fault segment of Dardanus Sulcus is expected to remain in a locked state throughout its diurnal orbital cycle. A higher coefficient of friction makes fault segments less prone to slip, with an even higher frictional stress; for example, for μ_f = 0.6 the mean frictional stress of Dardanus is 85±2 kPa. Moreover, tidal stress models, limited to present-day diurnal stresses, do not permit Coulomb failure along any of the nine major fault zones investigated here.

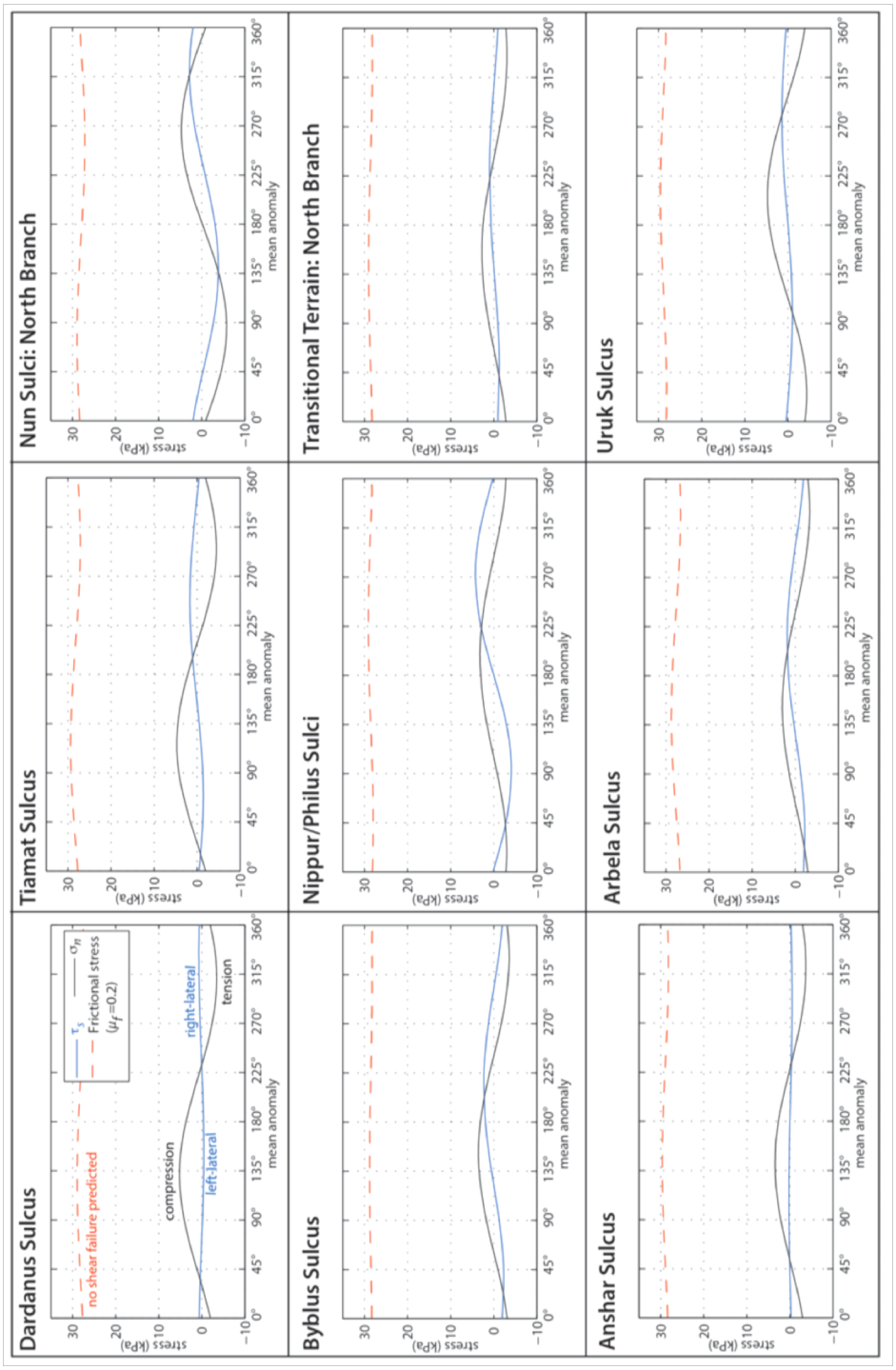

Figure 3.6. Modeled tractions on faults experiencing diurnal stresses. The mean modeled resolved normal traction (black), shear traction (blue), and frictional (red dashed) stress calculated at z = 100 m and μ_f =0.2. In this plot, negative resolved normal tractions are tensile, while positive normal tractions are compressive. Likewise, negative resolved shear tractions are left-lateral while positive shear tractions are right-lateral. The frictional stress for μ_f = 0.6 is not plotted, but has a mean value of 85±2 kPa, even higher than the low friction case demonstrated here. Shear failure is never achieved from diurnal stresses alone, given their very small magnitudes.

Given the evidence for strike-slip faults on Ganymede (Cameron et el., 2017), we next consider the role of NSR stresses as a potential driver for strike-slip faulting (Figures 3.7 – 3.15). In these figures, we demonstrate the diNSR model normal and shear tractions in map view (panel a), with tractions calculated along the midpoint position of each fault segment. Additionally, normal and shear traction dependency diagrams for varying orientations are provided in each map panel. Coulomb stresses (shear stress minus the frictional stress) are also plotted, in both map view and along cross-sections for both low ($\mu_f = 0.2$) and high ($\mu_f = 0.6$) friction cases (panel b). Representative Coulomb failure orientation dependency diagrams for varying segment orientations are also provided. Note that only the $m = 0°$ position of the diNSR model is presented here, given the negligible variation of these stresses as a function of mean anomaly (as shown in Figure 3.4). For the Coulomb failure models of Figures 3.7 – 3.15, when shear tractions exceeds the frictional stress, Coulomb stress is positive (green) and slip on the fault would be expected; if shear tractions are less than the frictional stress, Coulomb stress is negative (red) and a fault segment would be expected to be locked. For example, Figure 3.7 illustrates the major fault zone within Dardanus Sulcus, with modeled normal, shear, and Coulomb stresses for these structures, given the current fault strike and prescribed μ_f. In this and subsequent figures, small wavelength variations in stress along-strike are a result of a change in β, while longer wavelength variations are due to spatial changes in the stress field, as described in Section 3. The collective results in Figures 3.7 – 3.15 suggest Coulomb failure is possible down to depths of ~1 km for high friction ($\mu_f = 0.6$) cases and to ~2 km for low friction ($\mu_f = 0.2$) cases for most fault zones. We note that near-surface depth regions where tensile tractions are larger than the overburden stress, fault opening and frictionless shearing (and slip) are possible when a shear stress is applied. We do not model this region, as we limit the focus of this analysis to Coulomb failure guided by friction; hence this region is indicated as a gray region in the uppermost depths of each fault zone. Below we summarize the results for each fault zone individually for the assumed present-day fault geometry and location on the surface of the major fault zones of each region.

5.1. Dardanus Sulcus

Along the Dardanus Sulcus fault zone (Figure 3.7), located near the equator (sub-Jovian), normal tractions are tensile (-0.3 to -0.4 MPa) along the length of the fault zone, with some minor undulations near segments with more northerly strike. Modeled shear tractions are right-lateral (~0.15 to 0.2 MPa) along this NE-SW striking structure, with a few very low magnitude right lateral tractions along east-west oriented segments. This is consistent with the inferred right-lateral offset (Cameron et al., 2017) of the fault zone. Coulomb stress along most of the NE-SW striking segments is positive, however some of the segments that strike east-west have low magnitude Coulomb stress, and hence might not slip. An interesting feature that appears for the high friction μ_f= 0.6 model is the transition to a locked zone along the westernmost and mid-section of the fault, where the segment orientation strikes more E-W and NNE, respectively. High tensile tractions (gray zones) represent plausible slip zones, but are not guided by the physics of Coulomb failure. At Dardanus Sulcus, this prevents Coulomb failure at depths < ~800 m. For the low friction μ_f= 0.2 model, Coulomb failure is evident down to depths of ~2 km, with isolated locked zones along the southwest portion of the fault zone corresponding to patches of east-west oriented fault segments. For the high friction μ_f= 0.6 model, Coulomb stresses suggest that the much of the fault zone transitions to a locked state at depths slightly greater than 1 km.

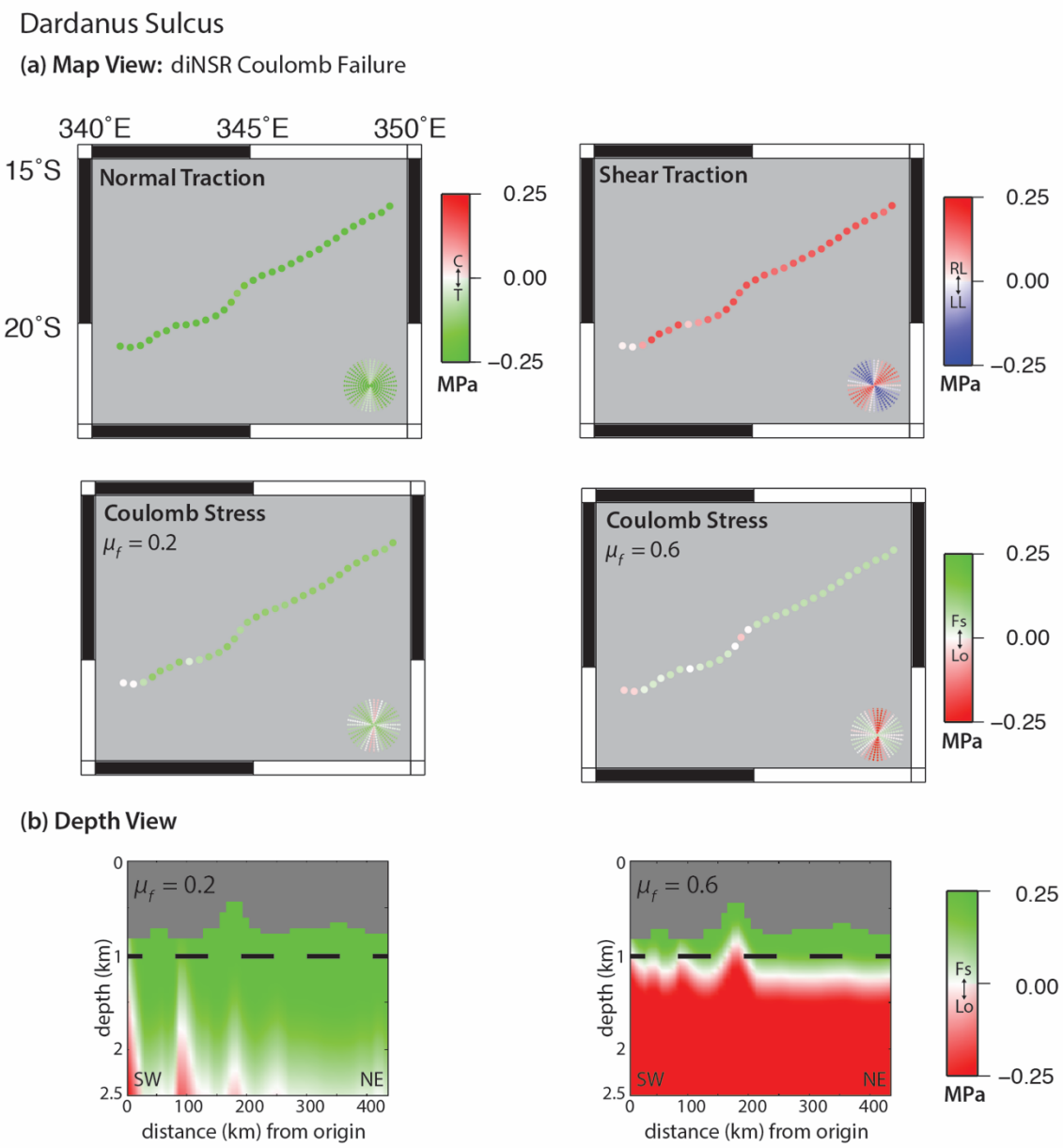

Figure 3.7 – 3.15. Resolved normal traction, shear traction, and Coulomb failure stresses of diNSR model. (a) Map view representation of normal (C = compression, T = tension), shear (RL = right-lateral, LL = left-lateral), and Coulomb stresses (Fs = indicating free to slip, Lo = locked) calculated at mean anomaly $m = 0°$. Stresses are provided at an example depth of $z = 1$ km and for $\mu_f = 0.2$ (low friction case) and 0.6 (high friction case). Each map view plot also shows the corresponding normal, shear stress, and Coulomb failure orientation diagrams (right corner), similar to the examples in Figure 3.5 but with color gradient preserved. Each orientation diagram shown is based on calculations at the midpoint of each fault zone. (b) Same as in (a), but with Coulomb stresses presented now along strike and as a function of depth in km, where the origin is defined as the western most point of the fault zone. Both low friction $\mu_f = 0.2$ and high friction $\mu_f = 0.6$ cases are provided. Gray zones are plausible slip zones, but not guided by the physics of Coulomb failure. The dashed line at 1 km corresponds to map view representation in (a).

5.2. Tiamat Sulcus

Along the Tiamat Sulcus fault zone (Figure 3.8) normal tractions are tensile along the entire length of the fault zone (-0.2 to -0.3 MPa), much like Dardanus (located ~150° to the west of Tiamat) due to their similar NE-SW orientation and similar stress regimes. Modeled shear tractions are also right-lateral (~0.1 to 0.2 MPa), in agreement with the inferred right-lateral offset (Cameron et al., 2017) across the fault zone. Coulomb stress along most of Tiamat Sulcus is positive (promoting failure) for the low friction μ_f= 0.2 model, but slightly negative for the high friction μ_f= 0.6 model. High tensile tractions (gray zones) at depths of < ~600 m represent plausible slip zones, but are not guided by the physics of Coulomb failure. For the low friction model, Coulomb stresses permit failure down to depths of ~1.5 km. For the high friction μ_f= 0.6 model, Coulomb stresses suggest that the much of the fault zone transitions to a locked state at depths of 0.7 to 1 km. This locked zone is shallower than at Dardanus Sulcus, although both features share a similar azimuthal strike, due to the lower magnitude shear tractions (and ultimately lower $\sigma_{\theta\theta}$ stress) in the region of Tiamat.

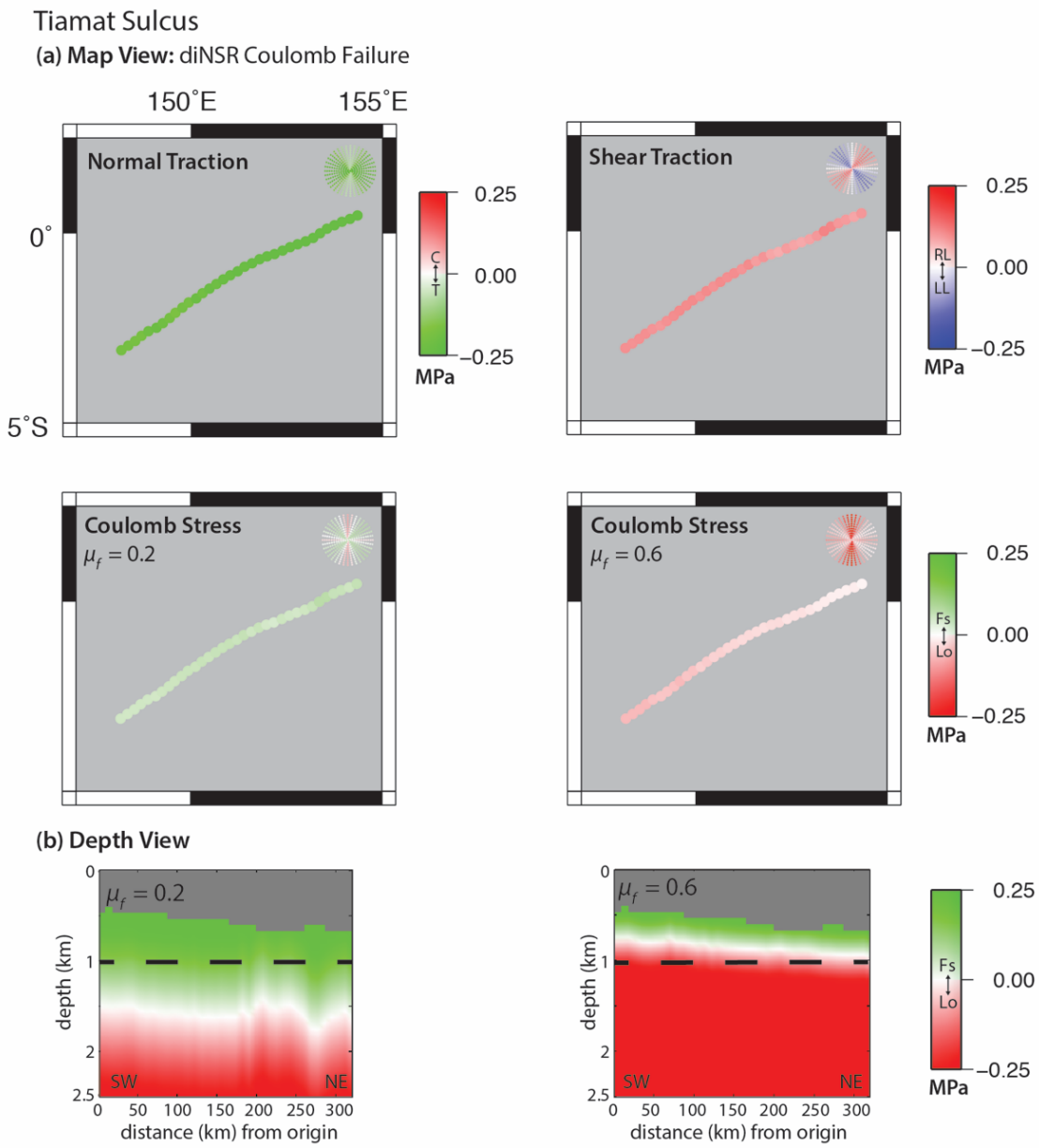
Tiamat Sulcus
(a) Map View: diNSR Coulomb Failure
150˚E
155˚E
0˚
5˚S
Normal Traction
C
T
0.25
0.00
−0.25
MPa
Shear Traction
RL
LL
0.25
0.00
−0.25
MPa
Coulomb Stress
$\mu_f = 0.2$
Coulomb Stress
$\mu_f = 0.6$
Fs
Lo
0.25
0.00
−0.25
MPa
(b) Depth View
$\mu_f = 0.2$
$\mu_f = 0.6$
depth (km)
0
1
2
2.5
SW
NE
0 50 100 150 200 250 300
distance (km) from origin
Fs
Lo
0.25
0.00
−0.25
MPa

Figure 3.8.

5.3. Nun Sulci

Along the two main branches of Nun Sulci (Figure 3.9), normal tractions are predominantly tensile along the NW-SE striking sections of the fault zone (-0.05 to -0.1 MPa) and compressional (0.1 to 0.4 MPa) along the E-W and NE-SW striking sections. We note that Nun Sulci is the only fault zone of this study located within the northern sub-Jovian latitudes, where its primarily east-west strike allows for both compressive and tensile stress regimes. Modeled shear tractions are right-lateral (~0.3 MPa). This differs from the left-lateral shear inferred from the imagery, and is discussed further in Section 6.2. The model supports Coulomb failure along much of the entire span of Nun Sulci for low ice friction μ_f= 0.2, although NE-SW striking sections of the south branch transition to locked zones in regions of highest compressive stresses. For the low friction μ_f= 0.2 model, Coulomb stresses permit failure down to depths of ~2.5 km for the north branch, and ~2 km (intermittently) for the south branch. Also along the south branch, the extended depth of the gray (non-Coulomb failure) zone along the eastern section is due to modest-to-high compressional stresses that act to clamp the fault together. For the high friction μ_f = 0.6 model, results suggest a completely locked fault from end to end on both branches at depths greater than ~700 m.

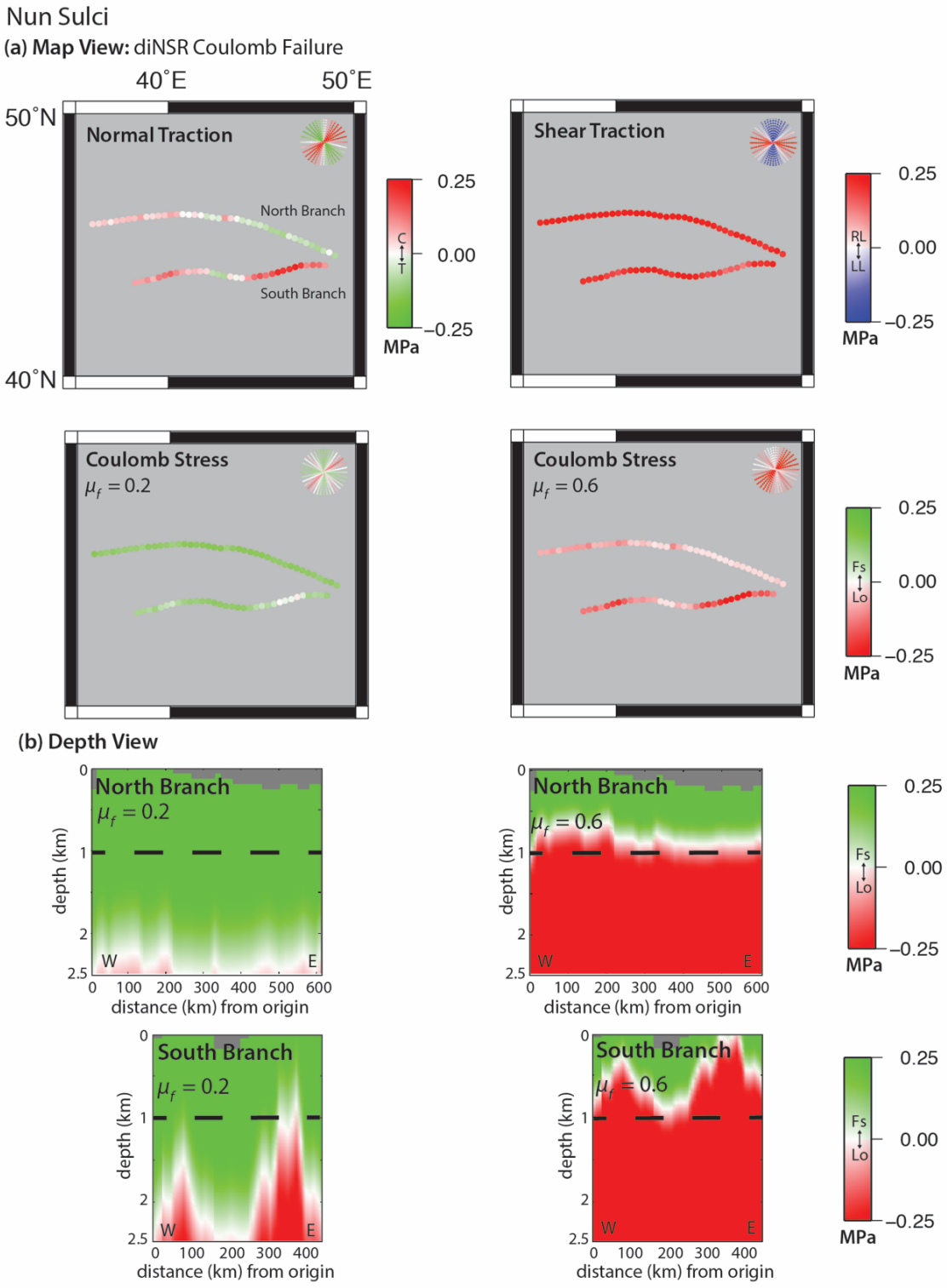
Nun Sulci
(a) Map View: diNSR Coulomb Failure
40˚E
50˚E
50˚N
40˚N
Normal Traction
North Branch
South Branch
C
T
0.25
0.00
−0.25
MPa
Shear Traction
RL
LL
0.25
0.00
−0.25
MPa
Coulomb Stress
$\mu_f = 0.2$
Coulomb Stress
$\mu_f = 0.6$
Fs
Lo
0.25
0.00
−0.25
MPa
(b) Depth View
North Branch
$\mu_f = 0.2$
North Branch
$\mu_f = 0.6$
depth (km)
0
1
2
2.5
W
E
0 100 200 300 400 500 600
distance (km) from origin
South Branch
$\mu_f = 0.2$
South Branch
$\mu_f = 0.6$
0 100 200 300 400
distance (km) from origin

Figure 3.9.

5.4. Byblus Sulcus

Along the Byblus Sulcus fault zone (Figure 3.10), located along similar longitudes to Tiamat Sulcus fault zone, normal tractions are compressive along much of the length of the fault zone (~ 0.1 MPa). Only the southeastern portion of the zone experiences low magnitude tensile stresses, due to its slight difference in strike with respect to the rest of the structure. Shear tractions are negative and hence left-lateral (~-0.1 to 0.3 MPa), in agreement with the inferred left-lateral shear in the region (Cameron et al., 2017). Coulomb stress along the NW-SE striking segments favor Coulomb failure for a low coefficient of friction (μ_f = 0.2), however the more NNW-SSE striking segments have very low to negative Coulomb stresses, limiting failure. Coulomb stresses for a high coefficient of friction are strongly negative for most of the zone. Modest tensile tractions (gray zones) at depths of < ~ 100 m represent plausible slip zones, but are not guided by the physics of Coulomb failure. For the low friction μ_f = 0.2 model, Coulomb stresses support failure down to depths of ~1 km, with only the southeastern most portion allowing failure to extend to ~2 km; the high friction μ_f = 0.6 model suggests that the much of the fault zone is locked below a depth of roughly 300 m.

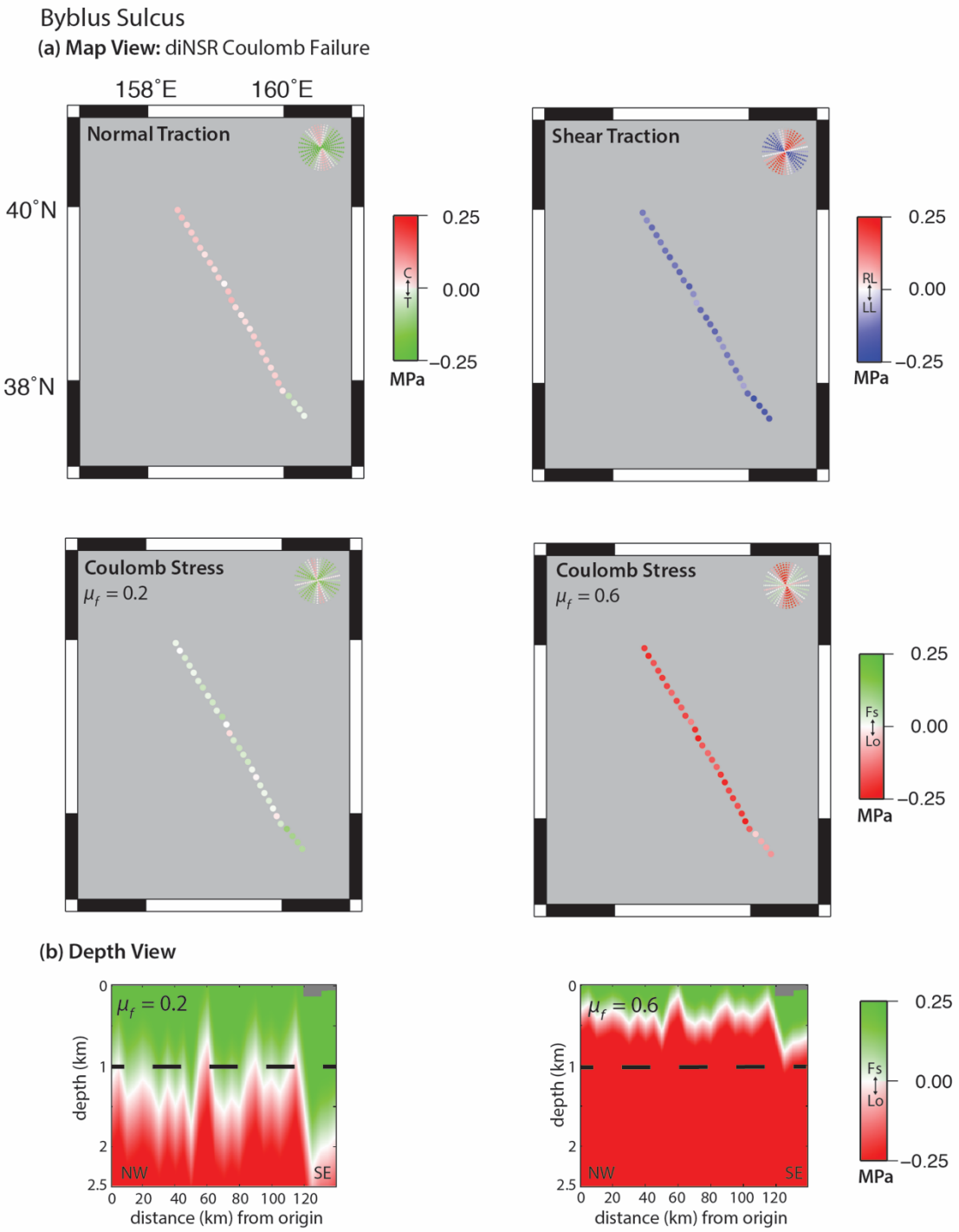
Byblus Sulcus
(a) Map View: diNSR Coulomb Failure
158˚E
160˚E
40˚N
38˚N
Normal Traction
C
T
0.25
0.00
−0.25
MPa
Shear Traction
RL
LL
0.25
0.00
−0.25
MPa
Coulomb Stress
$\mu_f = 0.2$
Coulomb Stress
$\mu_f = 0.6$
Fs
Lo
0.25
0.00
−0.25
MPa
(b) Depth View
$\mu_f = 0.2$
$\mu_f = 0.6$
depth (km)
0
1
2
2.5
NW
SE
0 20 40 60 80 100 120
distance (km) from origin
Fs
Lo
0.25
0.00
−0.25
MPa

Figure 3.10.

5.5. Nippur/Philus Sulci

Along Nippur/Philus Sulci fault zone (Figure 3.11) lying just north of the Byblus fault zone, normal tractions are tensile along much of the NW-SE striking fault zone (-0.1 to -0.2 MPa) and slightly positive (compression, ~0.1 MPa) at the northwestern side where the zone strikes slightly more north. Shear tractions are left-lateral (~-0.4 MPa), in agreement with the inferred left-lateral slip (Cameron et al., 2017) in the region. For the low friction μ_f= 0.2 model, the fault zone begins to lock only at the northwestern end due to the Coulomb stresses at 2.5 km depth, while the remaining span of the fault zone could experience slip. The high friction μ_f= 0.6 model suggests that the much of the fault zone is locked at depths > 1 km.

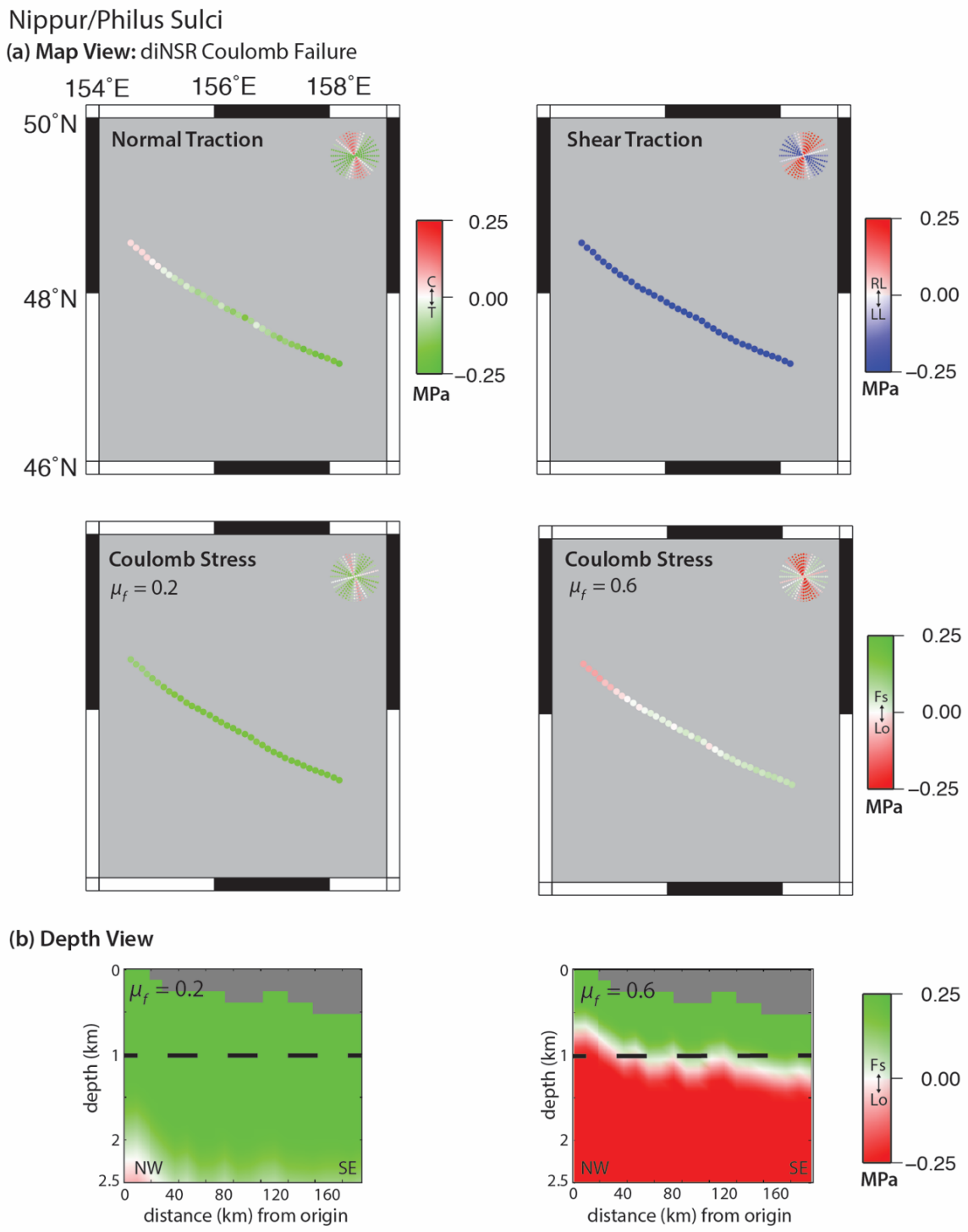
Nippur/Philus Sulci
(a) Map View: diNSR Coulomb Failure
154°E
156°E
158°E
50°N
48°N
46°N
Normal Traction
C
T
0.25
0.00
−0.25
MPa
Shear Traction
RL
LL
0.25
0.00
−0.25
MPa
Coulomb Stress
$\mu_f = 0.2$
Coulomb Stress
$\mu_f = 0.6$
Fs
Lo
0.25
0.00
−0.25
MPa
(b) Depth View
$\mu_f = 0.2$
$\mu_f = 0.6$
depth (km)
0
1
2
2.5
NW
SE
0
40
80
120
160
distance (km) from origin
Fs
Lo
0.25
0.00
−0.25
MPa

Figure 3.11.

5.6. Transitional Terrain

The Transitional Terrain region (Figure 3.12) is split into two branches (north branch spans longitudes of 170° – 176°; south branch spans 168° – 176°), located slightly southeast of Byblus Sulcus. Normal tractions reach a peak tensile stress of -0.4 MPa for the E-W and NW-SE striking segments within both the north and south branch. Segments with a more northerly strike, however, have very low magnitude, if not near-zero, normal tensile traction. Shear tractions are primarily left-lateral (-0.1 to -0.4 MPa), in agreement with the inferred left-lateral slip (Cameron et al., 2017) along the fault zone. Near the junction of the two branches is a low magnitude positive shear traction (~0.1 MPa), reflecting the east-west strike of this section. Coulomb stress along the NW-SE striking segments favor Coulomb failure for a low coefficient of friction (μ_f = 0.2), but have low magnitude positive and negative Coulomb stresses for a high coefficient of friction (μ_f = 0.6). For both friction cases, substantial variations in slip and locked zones may exist. For the low friction μ_f = 0.2 model, Coulomb stresses permit failure down to depths of ~2 km, with some locked portions in the northwest and southeast end of the north branch, and very isolated zones across the south branch. For the high friction μ_f = 0.6 model, however, Coulomb stresses suggest that the majority of both branches become locked at depths around 1 km, and become completely locked from end to end at depths of ~1.5 km.

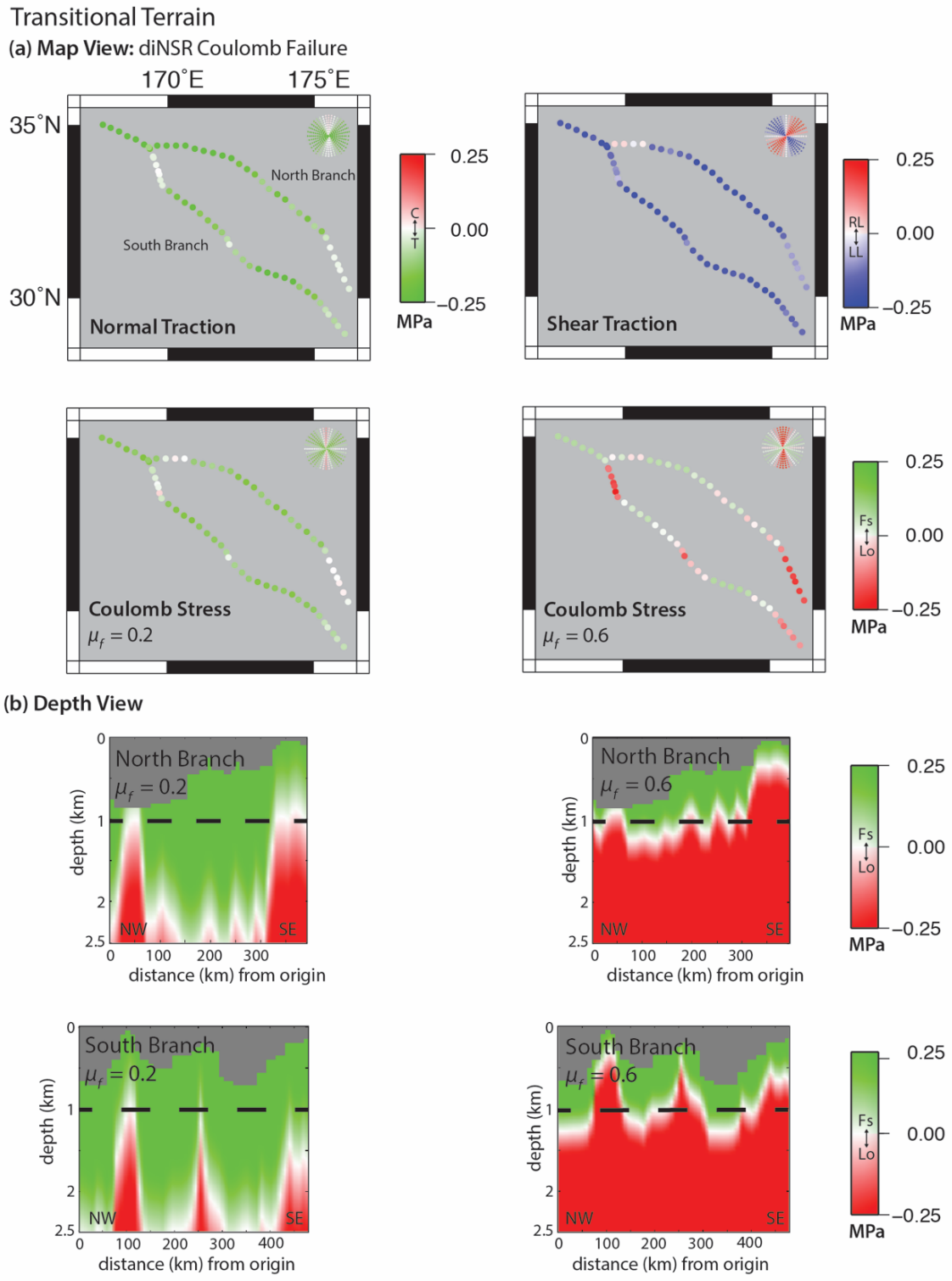
Transitional Terrain
(a) Map View: diNSR Coulomb Failure
170°E
175°E
35°N
30°N
North Branch
South Branch
Normal Traction
C
T
0.25
0.00
−0.25
MPa
Shear Traction
RL
LL
Coulomb Stress
$\mu_f = 0.2$
Coulomb Stress
$\mu_f = 0.6$
Fs
Lo
(b) Depth View
depth (km)
distance (km) from origin
NW
SE

Figure 3.12.

5.7. Anshar Sulcus

Along the Anshar Sulcus fault zone (Figure 3.13), located just to the east of Tiamat Sulcus and south of the Transitional Terrain, normal tractions are tensile along the entire length of the fault zone (-0.2 to -0.4 MPa). Shear tractions are primarily left-lateral (-0.3 MPa), with the southeastern end of the fault zone transitioning to right-lateral where the fault locally strikes east-west. This is in agreement with the inferred right-lateral slip along a fault splay (Prockter et al., 1998; Cameron et al., 2017). Coulomb stress along the entire span of Anshar is low magnitude but positive, thus promoting Coulomb failure for a low coefficient of friction (μ_f= 0.2). For high friction (μ_f= 0.6), Coulomb stresses are reduced, with both end sections of Anshar becoming slightly negative and thus locked. For the low friction μ_f= 0.2 model, Coulomb stresses permit some failure at depths > 2 km, although the fault zone would become locked at depths > 1 km near its southeast end; this behavior is less pronounced in the high friction case, where Coulomb stresses suggest that the much of the entire fault zone is locked at depths > 1 km.

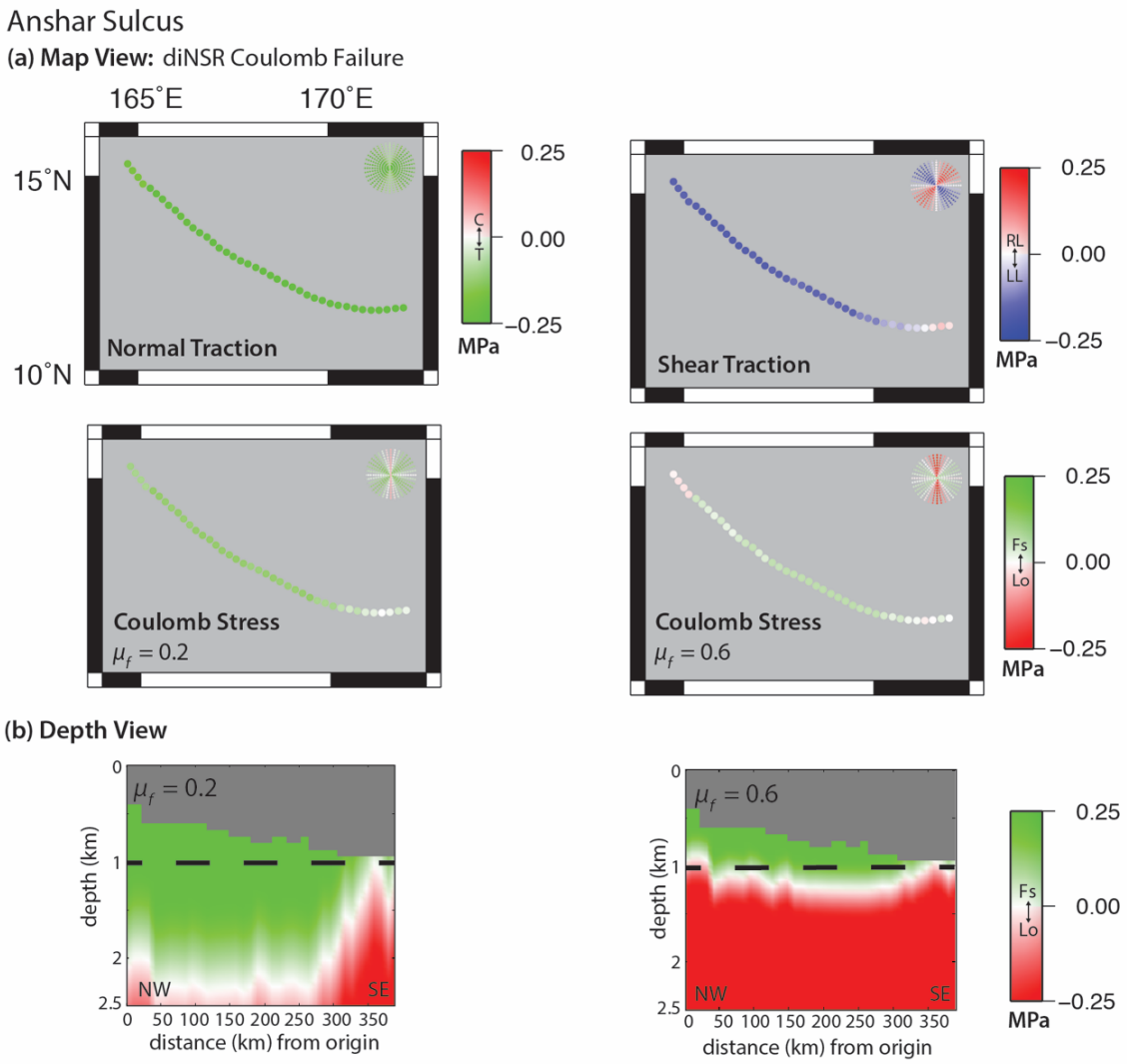
Anshar Sulcus
(a) Map View: diNSR Coulomb Failure
165°E
170°E
15°N
10°N
Normal Traction
C
T
0.25
0.00
−0.25
MPa
Shear Traction
RL
LL
0.25
0.00
−0.25
MPa
Coulomb Stress
$\mu_f = 0.2$
Coulomb Stress
$\mu_f = 0.6$
Fs
Lo
0.25
0.00
−0.25
MPa
(b) Depth View
$\mu_f = 0.2$
depth (km)
0
1
2
2.5
NW
SE
0 50 100 150 200 250 300 350
distance (km) from origin
$\mu_f = 0.6$
depth (km)
0
1
2
2.5
NW
SE
0 50 100 150 200 250 300 350
distance (km) from origin
Fs
Lo
0.25
0.00
−0.25
MPa

Figure 3.13.

5.8. Arbela Sulcus

Along the Arbela Sulcus fault zone (Figure 3.14), located along the sub-Jovian longitudes near Dardanus, resolved normal tractions are tensile along its entire length (~ -0.3 to 0.6 MPa). Shear tractions are right-lateral (~0.2 MPa), which appears incompatible with the inferred left-lateral slip and is discussed further in Section 6.2. Coulomb stress along most of Arbela is positive (promoting failure) for the low friction μ_f= 0.2 model, but slightly negative for the high friction μ_f= 0.6 model, similar to the situation along the Tiamat Sulcus fault zone, which shares a common equatorial latitude with Arbela. High tensile tractions (gray zones) at depths of < ~ 500 m represent plausible slip zones, but are not guided by the physics of Coulomb failure. For the low friction μ_f= 0.2 model, Coulomb stresses permit failure along the length of the fault zone down to depths of ~ 2 km. For the high friction μ_f= 0.6 model, Coulomb stresses suggest that much of the fault zone is locked at depths of > ~ 1 km.

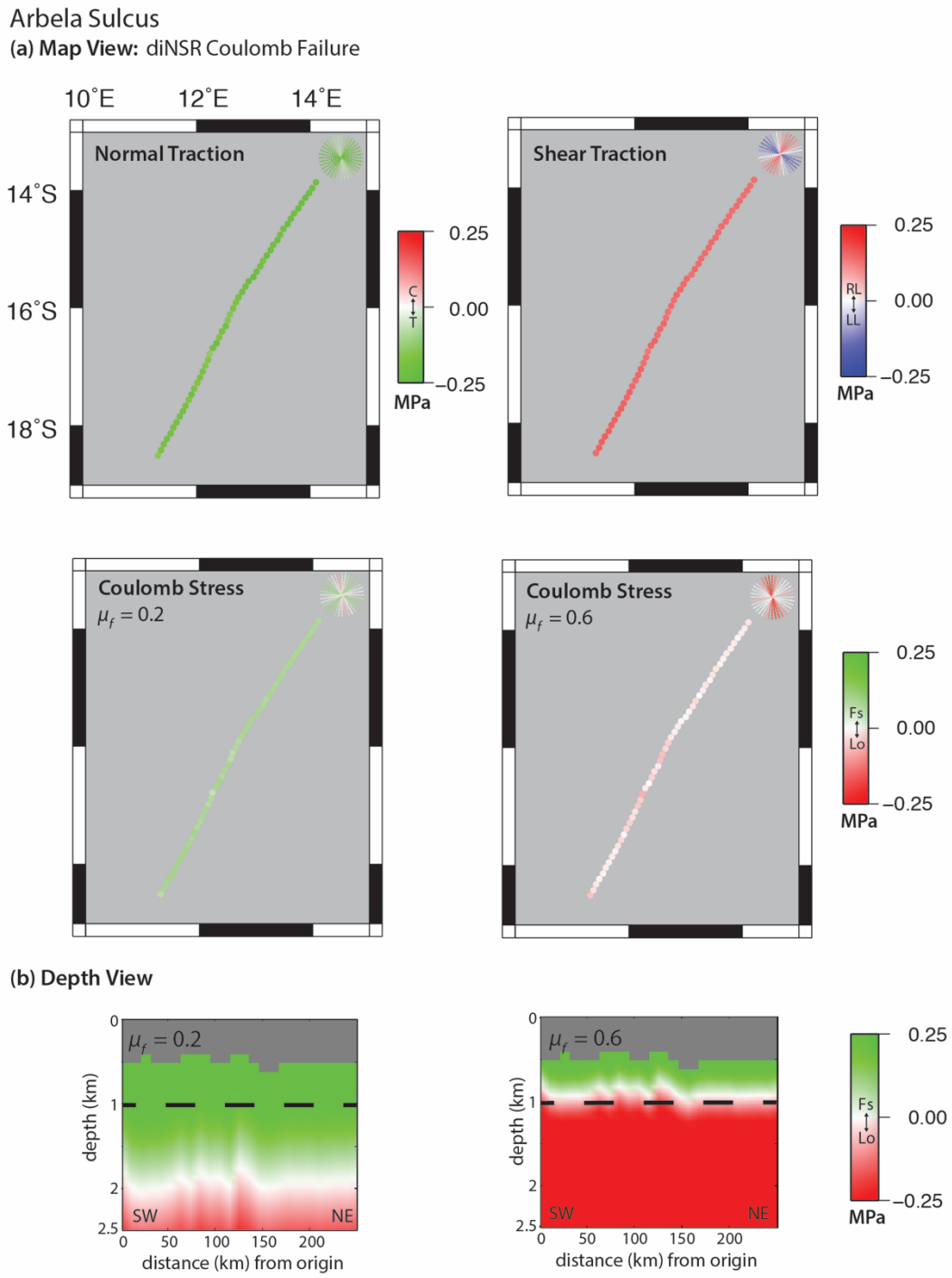
Arbela Sulcus
(a) Map View: diNSR Coulomb Failure
10°E
12°E
14°E
14°S
16°S
18°S
Normal Traction
C
T
0.25
0.00
−0.25
MPa
Shear Traction
RL
LL
0.25
0.00
−0.25
MPa
Coulomb Stress
$\mu_f = 0.2$
Coulomb Stress
$\mu_f = 0.6$
Fs
Lo
0.25
0.00
−0.25
MPa
(b) Depth View
$\mu_f = 0.2$
$\mu_f = 0.6$
depth (km)
0
1
2
2.5
SW
NE
0
50
100
150
200
distance (km) from origin
Fs
Lo
0.25
0.00
−0.25
MPa

Figure 3.14.

5.9. Uruk Sulcus

Along the Uruk Sulcus fault zone (Figure 3.15), normal tractions are tensile along the entire length of the fault zone (~-0.4 MPa). Shear tractions are primarily left-lateral (-0.2 MPa) along the ends and midpoint of the fault zone, which appears incompatible with the inferred right-lateral slip (Cameron et al., 2017); this is discussed further in Section 6.2. The regions on each side of the midpoint transition to slightly right-lateral where the zone locally strikes more nearly E-W. These nuanced variations may be in part due to Uruk Sulcus being the smallest mapped area with the highest resolution imagery (40 – 75 m/pixel) when compared with the other eight mapped sites (100+ m/pixel). The fault zone at Uruk Sulcus strikes similar to the fault zone of Anshar Sulcus, Uruk's nearest neighbor. Also like Anshar, Coulomb stresses are of low magnitude but positive, thus promoting Coulomb failure for a low coefficient of friction (μ_f= 0.2), but locked near the center of the fault. For high friction (μ_f= 0.6), Coulomb stresses are further reduced, and along the mid section of Uruk, become negative. Coulomb stresses also display the same end/midpoint pattern as the shear tractions, with stresses at the ends and midpoint permitting failure, with locked zones predicted on each side of the midpoint; this behavior demonstrates the significance of the magnitude of the shear stress in permitting slip. For the low friction μ_f= 0.2 model, Coulomb stresses permit some failure at depths > 1 km, especially on the northwestern end where β steepens. For the high friction μ_f= 0.6 model, Coulomb stresses suggest that the much of the entire fault zone is locked at depths > 1 km, with the ends of the fault zone experiencing a slightly deeper (1.25 km) locking depth.

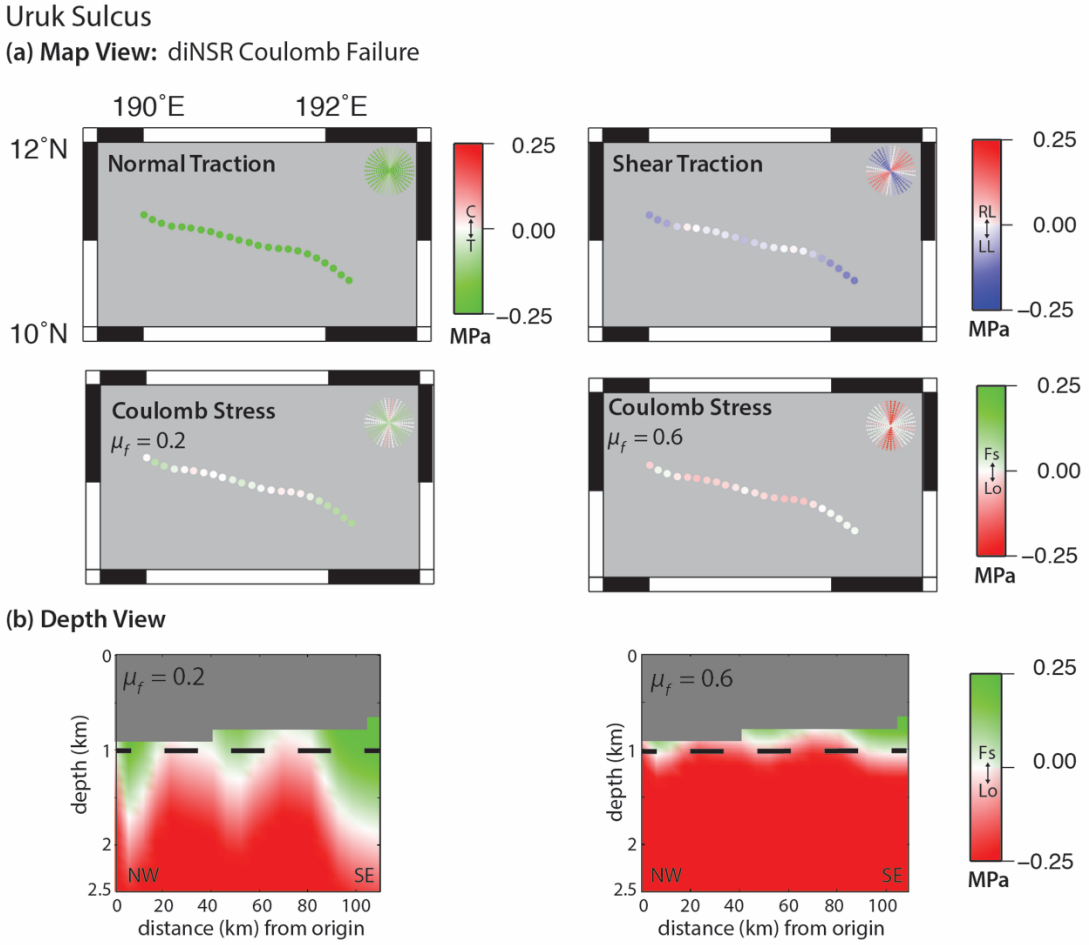
Uruk Sulcus
(a) Map View: diNSR Coulomb Failure
190°E
192°E
12°N
10°N
Normal Traction
C
T
0.25
0.00
−0.25
MPa
Shear Traction
RL
LL
0.25
0.00
−0.25
MPa
Coulomb Stress
$\mu_f = 0.2$
Coulomb Stress
$\mu_f = 0.6$
Fs
Lo
0.25
0.00
−0.25
MPa
(b) Depth View
$\mu_f = 0.2$
$\mu_f = 0.6$
depth (km)
0
1
2
2.5
NW
SE
0
20
40
60
80
100
distance (km) from origin
Fs
Lo
0.25
0.00
−0.25
MPa

Figure 3.15.

6. Discussion

These results suggest that diurnal stresses at Ganymede today are quite small (<10 kPa) and that global tidal stress models limited to only present-day diurnal stress do not permit Coulomb failure along any of the nine major fault zones investigated here. Alternatively, we find that a combination of both diurnal and NSR stress mechanisms readily generate shear and normal traction magnitudes that promote Coulomb failure in all nine regions. We note that previous work examining Europa's stress history has considered the sole role of diurnal stresses and found these to be sufficient to promote tidal walking mechanisms of faulted structures (Hoppa et al., 1999). Europa's diurnal stresses, however, are 10 times those of Ganymede's, and therefore likely play a more significant role in driving fault slip, as evidenced by cycloidal features, series of linked arcuate features (Hoppa et. al, 1999b; Kattenhorn and Hurford, 2009; Hurford et al., 2009). Moreover, while Ganymede's diurnal stresses are small today, they may have been much larger during a former period of high-eccentricity (e = 0.05, Greenberg 1987; Malhotra, 1991; Showman and Malhotra, 1997). A detailed investigation spanning the role of eccentricity is beyond the scope of this paper; however, we are currently developing models to explore the sensitivity of Coulomb failure for such a possible high-eccentricity past (Cameron et al., in prep). Nevertheless, we find that a present-day diurnal and NSR stress combination easily supports Coulomb failure for several inferred shear zones on Ganymede.

6.1. Comparisons to strike-slip indicators and failure depth

To perform a first-order comparison of mapped and modeled shear sense, we limit our analysis to the previously mapped regions of Cameron et al. (2017), where the sense of slip is deduced based on strike-slip indicators (i.e., *en echelon* structures, strained craters, and significant offsets). We compare the overall slip along fault zones in these regions to the resolved shear tractions, as derived from SatStress output and measured fault orientation (Eq. 1 and Figure 3.5) where positive shear traction is right-lateral, and negative shear traction is left-lateral. Since there is negligible diurnal variation in the diNSR model, we note that the resolved tidal shear stresses of this model do not alternate between right- and left-lateral

modes over the diurnal cycle like the traditional tidal walking model (i.e., Hoppa et al., 1999); the stresses are largely static and hence slip derived from stress accumulation gradients (Rhoden et al., 2012) do not apply here. Moreover, we find compatible senses of shear between our observations and predictions at six of the nine regions studied here, although it is important to note that these results are sensitive to both fault strike (affecting how stress is resolved onto modeled fault planes) and our inferred morphology of strike-slip indicators (Cameron et al., 2017). Because confidence in slip sense is greatest where easily-identified strike-slip offsets occur (which also provide the strongest inference of brittle failure), we next organize our results into three groups: (1) fault zones with discernable offset, (2) fault zones with indirect strike-slip indicators and a compatible predicted slip sense, and (3) fault zones with indirect strike-slip indicators and incompatible slip sense.

(1) *Fault zones with discernable offset of preexisting features:* Hard evidence for strike-slip offset, as inferred in Galileo imagery (Figure 3.1), occurs at three of our target regions: Dardanus Sulcus (45 km offset, right-lateral), Tiamat Sulcus (40 km offset, right-lateral), and Nun Sulci (50 km offset, left-lateral). These three regions have diverse geographic locations, with Dardanus Sulcus positioned in the low southern latitudes of Ganymede's sub-Jovian point, Tiamat Sulcus positioned near the equator of Ganymede's anti-Jovian point, and Nun Sulci positioned in the higher northern latitudes of Ganymede's trailing hemisphere. Resolved shear tractions along Dardanus and Tiamat offsets are consistent with their respective inferred shear senses: Dardanus Sulcus (Figure 3.7) and Tiamat Sulcus (Figure 3.8) are dominated by right-lateral modeled shear tractions along the fault zones. Alternatively, resolved shear tractions (right-lateral) for Nun Sulci are incompatible with the inferred left-lateral offset, however a well-documented strained crater, Nefertum, located within the Nun Sulci fault zone (Figure 3.9), suggests right-lateral deformation (Pappalardo and Collins, 2005), consistent with right-lateral R shear orientations along the strained crater's major axis. While models suggest Nun Sulci is dominated today by right-lateral shear tractions, this may be due to its current E-W azimuthal strike, as global models suggest much of this region is expected to experience left-lateral slip (discussed further in Section 6.2).

(2) *Fault zones with indirect strike-slip indicators and a compatible predicted slip sense:* Other fault zones that present where the deduced sense of slip is compatible with the

modeled stress fields are recognized at Byblus Sulcus (Figure 3.10), Nippur/Philus Sulci (Figure 3.11), and Transitional Terrain region (Figure 3.12). While these regions do not display any clear examples of offset of pre-existing structures, the sense of *en echelon* structures, strike-slip duplexes, and strained craters found in each region suggest prevalent left-lateral shear across the fault zones (Cameron et al., 2017). We calculate shear tractions along each major zone and find that all should be dominated today by left-lateral shear traction, consistent with the inferred sense of slip deduced from surface features. Interestingly, our models suggest both left- and right-lateral shear at Anshar Sulcus (Figure 3.13), with right-lateral shear localized at the southeast end of the fault zone as it transitions to a more E-W orientation. In this same location, Cameron et al. (2018) inferred a right-lateral splay fault (see also Prockter el al., 1998). To the west, however, a mapped strained crater just south of the main fault zone was inferred to be left-lateral by Pappalardo and Collins (2005).

(3) *Fault zones with indirect strike-slip indicators and incompatible slip sense:* The inferred sense of slip at Arbela Sulcus (left-lateral), and Uruk Sulcus (right-lateral) are not clearly compatible with present-day stress fields predicted by our tidal stress modeling. The fault zone at Arbela Sulcus, like Dardanus Sulcus, strikes roughly NE-SW and is positioned in the low southern latitudes of Ganymede's trailing hemisphere. Similar to Dardanus, Arbela's resolved shear traction is right-lateral, demonstrating the regional consistency of these two fault zones' modeled shear traction. Independent inferences from satellite imagery suggest, however, that Arbela has left-lateral *en echelon* structures and a possible left-lateral offset (Head et al., 2002). The fault zone at Uruk Sulcus, the only modeled region in the anti-Jovian leading hemisphere, is predicted to have mostly left-lateral slip; however, regions of the fault that approach a more E-W strike are predicted to be right-lateral. A possible explanation for the incompatible shear sense at Arbela and Uruk Sulcus may be due to the migration and reorientation of the ice shell, in which a feature may have formed in a different orientation or location than it is presently positioned (discussed further in Section 6.2).

Based on these results, we infer that Coulomb failure within the upper few km of Ganymede's icy outer shell is possible along the nine analyzed fault zones when NSR is included as a driving stress mechanism. Tensile stresses within the uppermost 1 km of most

fault zones are important to consider in a fault's behavior, as they are plausible regions of slip, though not subject to Coulomb failure due to fault opening. Frictionless sliding in the uppermost depths or some other mechanism may still link the motions between the interface between fault opening and Coulomb failure regions, but is not considered here. Additionally, given the parameters investigated by this work, Coulomb failure seems to be confined to depths < 2 km for most fault zones, suggesting there is a mechanical link to the brittle-ductile elastic thickness depth of Ganymede's icy shell, estimated at ~ 2 km (Nimmo, 2004; Wahr et al., 2009; Jara-Orué and Vermeersen, 2016)

The 2 km locking depth zone for shear zones of Ganymede studied here is slightly more shallow than those inferred on other icy satellites, due to the smaller tidal influence on Ganymede than many of its counterparts. For example, studies of the tiger stripe fractures on Enceladus (Smith-Konter and Pappalardo, 2008; Olgin et al., 2011) find that failure conditions may extend down to depths ~2–3 km when considering a 24 km thick ice shell; these values represent the bottom of the locked fault. Additionally, studies applying similar methods to Europa linea (Cameron et al., 2012; Cameron et al., 2015) suggest failure depths < 6 km from NSR simulations. These values are compatible with estimates of Europa's effective ice shell elastic thickness (6^{+5}_{-2} km) based on stereo topographic profiles (Nimmo et al., 2004).

6.2. Alternate stress mechanisms

Deviations of observed slip sense between imagery and global slip predictions from modeling may be due to a number of mechanisms that could alter fault location and/or orientation over time. For example, we find a small rotation of the modeled strike of Nun Sulci, Arbela, Anshar, and Uruk Sulcus (~10 – 30° counterclockwise) results in subtle but reversed sense of shear that is compatible with mapped shear indicators discussed in Section 6.1. Additionally, true polar wander (TPW) involves reorientation of an icy satellite's floating outer ice shell about the tidal axis with Jupiter. TPW is possible if the icy shell is latitudinally variable in thickness and decoupled from the rocky interior, imposing high stress levels on the shell (Schenk et al., 2008). While beyond the scope of this study, TPW has been proposed as a possible explanation for some of the features whose tectonic patterns and stress

history remains unexplained (Schenk et al., 2008). It is also important to note that for each of these tectonically complex regions, the major fault zone structure adopted for our shear calculations may not have been formed by strike-slip tectonism, but instead by tensile stresses, as suggested by several *en echelon* features associated with several of these structures. Thus local rheological conditions and pre-existing fault structures may also affect sense of shear.

6.3. Global Coulomb Failure and Sense of Shear

Beyond our localized analyses of tractions and Coulomb failure of the nine high-resolution imaged regions presented here, we can also expand our modeling efforts to a global scale. Combining the schematic representation of tractions on a fault as a function of fault orientation, or β (Figure 3.5), we explore ranges of fault strikes from 60°S-60°N, represented by structures of 5° in length and of varying β centered within 96 grid cells spanning 15° latitude by 30° longitude (Figure 3.16). For simplicity, the Coulomb failure orientation results of Figure 3.16 represent the modeled stresses at 1 km depth, consistent with previous figures.

Global normal traction patterns (Figure 3.16a) reflect the variation in principal stress magnitude and sign, with high compressional zones centered within the leading and trailing equatorial regions, for north and south latitudes less than ~ 25°. Faults of any orientation will be subjected to compressive tractions in these regions. Alternatively, high tensile zones centered within the anti- and Sub-Jovian equatorial regions (again confined to latitudes less than 25°), suggest faults of any orientation will experience tensile tractions. High north and south latitudes host the lowest principal stresses and also provide a range of compression and tension regimes as a function of fault orientation and longitudinal position.

Global shear traction patterns (Figure 3.16b) largely follow the variation in magnitude and sign of shear stress tensor component $\sigma_{\theta\varphi}$. The shear traction orientation dependency diagrams suggest that faults that strike predominately north-south within positive shear stress zones are subject to right-lateral shear. Alternatively, faults that strike predominantly north-south within negative shear stress zones are subject to left-lateral shear. This pattern repeats every 90° and is inverted about the equator. Additionally, shear traction orientation

dependency diagrams are inverted and reflected across the central meridian. This reflection/inversion pattern has previously been observed by Rhoden et al. (2010) when examining strike-slip predictions given their model considerations (diurnal stresses with no obliquity), although orientation results vary from this study. We note that there is no diurnal reversal of shear direction for this model given the quasi-steady-state of NSR. Interestingly, the four fault zones located within the highest northern latitudes and highest magnitude shear regimes have orientations that favor a reversed sense of shear: Nun Sulcus is positioned in a left-lateral shear region, but its E-W orientation subjects it to right-lateral shear tractions. Likewise, Nipper/Philus, Byblus, and the Transitional Terrain are positioned in a right-lateral shear region, however these fault zones are largely subject to left-lateral shear due to their NW-SE orientations. When investigating Coulomb failure orientations, we find there are regions where either right- or left-shear failure might occur.

From this global perspective, we also demonstrate the abundance of Coulomb failure opportunities for strike-slip structures of Ganymede. For a diNSR stress model, resolved shear and normal tidal tractions promote Coulomb failure at depths of ~1 km along a wide range of geographic locations and fault orientations (Figure 3.16c). However, Coulomb failure is highly sensitive to influences from compressive stresses when combined with low shear stress magnitudes, as evidenced by the few faults (black, or fully locked wedges) near the equator, where the largest compressive NSR stresses and lowest shear regimes are centered. As such, the only regions along the equator capable of Coulomb failure lie in longitudinal zones of high tensile stresses. Coulomb failure orientation dependency diagrams are reflected about the equator and repeated about the central meridian (0° E).

Moreover, by isolating and plotting the shear tractions and Coulomb failure potential in such a manner, we construct a more complete perspective of the sensitivity of slip to fault orientation. Modeling tidal stresses in this way may also allow us to predict whether a feature of interest is optimally oriented for failure, and in what direction it will slip. While this method may be currently applied to existing imagery, high-resolution imagery from future spacecraft may allow us to characterize regional trends in strike slip orientation based on finer scale indicators. For example, the European Space Agency's (ESA) large-class mission *JUICE* (JUpiter ICy moons Explorer) aims to spend at least three years making detailed

studies of Ganymede, Callisto, and Europa after its proposed arrival in 2030. This increased coverage may allow us to better understand the timeline of deformation and potentially constrain the time scales of secular stresses that drive this slip.

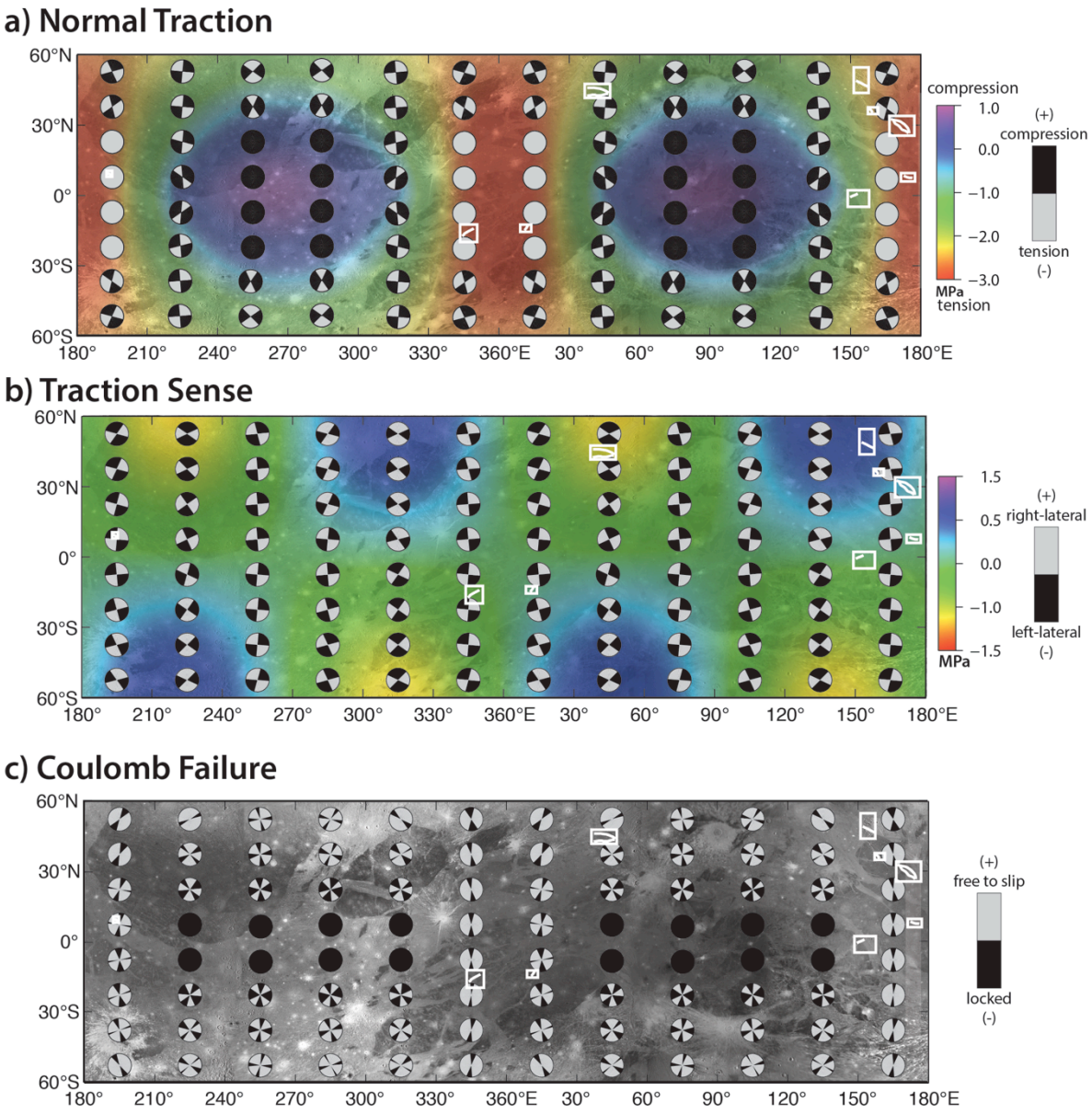

Figure 3.16. Global failure predictions for a diNSR model. (a) Normal stress orientation diagrams (simplified black and gray representations, see Figure 3.5) overlaying global imagery and maximum principal stress (σ_1, MPa). Note regions of high compressive stresses near the equator. (b) Traction sense diagrams overlaying global imagery and stress tensor component $\sigma_{\theta\varphi+\varphi\varphi}$ (MPa). (c) Coulomb failure orientation diagrams overlaying global imagery. Note regions of limited slip corresponding to high compressive stresses and low shear stresses. All images are for a mean anomaly, $m = 0°$.

7. Conclusions

In this study, we investigate the conditions necessary for tidally driven Coulomb failure on Ganymede due to two fundamental stress mechanisms: diurnal and nonsynchronous rotation tidal stresses. Using the Coulomb failure criterion to assess failure potential, we find that Ganymede's diurnal tidal stresses are not large enough to yield Coulomb failure within the shallow brittle crust. However, when stresses derived from the nonsynchronous rotation (NSR) of Ganymede's outer icy shell are included, shear and normal tractions on the order of ~1 MPa are resolved onto imaged fault structures. Moreover, we find that the diNSR tidal stress model provides stress magnitudes and orientations on Ganymede that support Coulomb failure at shallow depths along candidate strike-slip structures. We explored the sensitivity of the coefficient of ice friction ($\mu_f = 0.2 - 0.6$) and the depth dependency of Coulomb failure, demonstrating how low friction permits failure down to depths of ~ 2 km for nine fault zones with inferred (previously mapped) strike-slip structures.

Based on these results, we infer that Coulomb failure is possible, when NSR is included as a driving stress mechanism, along many fault zones spanning Ganymede's surface. The NSR model successfully predicts the same sense of slip for six candidate fault zones as inferred from imagery and mapping efforts (Dardanus Sulcus, Tiamat Sulcus, Byblus Sulcus, Nippur/Philus Sulci, Anshar Sulcus, and the Transitional Terrain region). Tractions from the three other fault zones (Nun Sulci, Arbela Sulcus, and Uruk Sulcus) that do not match the inferred sense of slip may be consistent with a migrating ice shell as due to NSR, perhaps allowing for reorientation of modeled strike. Local rheological conditions, pre-existing faults, and temporal sensitivity to orbital evolution may also affect sense of predicted slip. Moreover, these results reflect tidal dynamics assuming the present-day eccentricity for Ganymede, however preliminary work (Pappalardo et al, 2012; Cameron et al., 2017) suggests a past high eccentricity may have allowed for significant diurnal tidal stress influence on faulting at very shallow depths (< 200 m). The sensitivity of diurnal tidal stresses to Ganymede's past eccentricity is currently being investigated (Cameron et al., in prep) and may help to advance our understanding of faulting in several tectonically complex regions across Ganymede's surface.

Acknowledgments

We thank S. Martel, P. Lucey, S. Fagents, P. Mouginis-Mark, and S. Howell for constructive conversations that helped clarify this manuscript. The portion of this research by R.T.P. was carried out at the Jet Propulsion Laboratory, California Institute of Technology, under a contract with the National Aeronautics and Space Administration. This research was supported by the NASA Outer Planets Research Program (NNX14AE15G).

Author Contributions

M.C. combined previous methods used by B.S.K. and R.P. with original data and performed all numerical calculations. M.C. created all images. M.C. developed the global slip prediction method presented in the study. B.S.K., G.C., D.P., and R.P., provided feedback on results. M.C. wrote the manuscript with consultation from all authors.

CHAPTER 4. GANYMEDE THEN AND NOW: HOW PAST ECCENTRICITY MAY HAVE ALTERED TIDALLY DRIVEN COULOMB FAILURE

Marissa E. Cameron[1], Bridget R. Smith-Konter[1], Geoffrey C. Collins[2], Donald A. Patthoff[3], and Robert T. Pappalardo[3]

[1]*Department of Geology and Geophysics, University of Hawai'i at Mānoa, Honolulu, HI 96822*

[2] *Physics and Astronomy Department, Wheaton College, Norton, MA, 027663*

[3] *Jet Propulsion Laboratory, California Institute of Technology, Pasadena, CA 91109*

[*] Corresponding author: mecamero@hawaii.edu

Abstract

Laplace-like resonances among Ganymede, Europa, and Io may have once led Ganymede to acquire an eccentricity as high as ~0.07 (presently e = 0.0013). While diurnal stresses at Ganymede today are quite small (less than 10 kPa), a previous period of higher eccentricity may have allowed for a diurnal tidal stress that could drive faulting during a past period of active tectonism, with stresses increasing by at least an order of magnitude. To investigate the role of tidal stresses on faulting, we use the numerical tidal stress model SatStress to calculate diurnal tidal stresses of Ganymede's surface assuming e = 0.05, representative of a more eccentric orbit in Ganymede's past. The past model assumes a 100 km ice shell (upper 2 km is cold, stiff ice), underlain by a 140 km deep ocean. We resolve normal and shear stresses onto discrete mapped fault segments and assess Coulomb failure criteria along three previously inferred shear zones: Dardanus Sulcus, Tiamat Sulcus, and Nun Sulci. We find that for a diurnal model of present-day (low) eccentricity, Coulomb failure is not expected along any of the three shear zones. Coulomb failure is predicted, however, for a past, high eccentricity case, although in isolated diurnal slip windows and limited to very shallow depths (results are shown for a depth of 100 m, failure may extend to ~ 250 m). This model predicts a dominant right-lateral slip window for both Dardanus and Tiamat Sulcus and right- and left-lateral slip windows for both north and south branches of Nun Sulci, coincident with the sense of inferred shear from imagery and structural mapping efforts. Moreover, a low coefficient of friction (μ_f= 0.2) Coulomb failure model of right- and left- lateral slip episodes over a diurnal cycle could indicate a plausible case for tidal walking in Ganymede's high-eccentricity past.

In preparation for submittal to EPSL.

1. Introduction

Twin spacecraft *Voyager* 1 and 2 began imaging the Jupiter system in 1979, followed by the *Galileo* space probe that orbited Jupiter's moons between 1995 and 2003, providing high-resolution images and geophysical data. Images from *Galileo* and *Voyager* reveals Ganymede's surface to be extensively tectonized. The surface of Ganymede displays several candidate regions of strike-slip tectonism, with fault slip presumably driven by a combination of global and local stress sources. As Ganymede orbits Jupiter every 171.6 hours, variations in gravitational tidal forces, due in part to the satellite's eccentric orbit, act to deform the moon's surface (Greenberg et al., 1998), with diurnal stresses on the order of a few 10s of kPa when considering Ganymede's eccentricity (presently e = 0.0013). Past Laplace-like resonances among Ganymede, Europa, and Io may have altered eccentricity to as high as ~0.07 depending on the past ratio of tidal dissipation between Ganymede and Jupiter (Showman and Malhotra, 1997), yielding potential diurnal tidal stresses on the order of 100s of kPa. This increase in diurnal stress may have been a catalyst for faulting during a past period of tectonic activity, similar in nature to geologic activity currently, or fairly recently, on other icy satellites (Greenberg et al., 1998; Hurford et al., 2007; Collins, 2009).

We use the numerical code SatStress (Wahr et al., 2009) to calculate diurnal tidal stress as a plausible mechanism for strike-slip tectonism at Ganymede's surface considering a past, higher eccentricity. We utilize the Coulomb stress equation (Byerlee, 1978) to determine the Coulomb failure potential of fault segments of varying orientation and as a function of mean anomaly (orbital position), m. Previous studies (Cameron et al., 2018a) detailed nine mapped *Galileo* target sites displaying evidence of strike-slip indicators (*en echelon* structures, strike-slip duplexes, laterally offset pre-existing features, and strained craters). Of these strike-slip indicators, lateral offset (Figure 4.1) of pre-existing structures at Dardanus Sulcus, Tiamat Sulcus, and Nun Sulci provide the clearest evidence for which to evaluate sense of shear and are therefore used as the basis for testing the influence of diurnal stresses and Coulomb failure when considering a past eccentricity.

This paper revisits tidal stress modeling efforts of Cameron et al. (2018b) assuming a present-day eccentricity (0.0013) and compares those previous results with new results

considering a possible past high (~0.05) eccentricity. We first provide a brief overview of the geologic history of three target regions displaying strike-slip offset, Ganymede's orbital evolution through time, and the effects of eccentricity changes on internal structure. Next we discuss the potential for Coulomb failure induced by diurnal tidal stresses considering the limitations on failure that are imposed by the Coulomb failure criterion. We also describe adaptations to our modeling process to account for varying eccentricity tides. We demonstrate Coulomb failure results for each of the three offset regions and evaluate how failure estimates vary as a function of mean anomaly. Finally, we examine the implications of this failure model of both right- and left-lateral slip episodes over a diurnal cycle as a plausible case for tidal walking in Ganymede's high-eccentricity past. This work aims to establish the importance of tidal stresses as a driver for strike-slip tectonism, noting that past-Ganymede diurnal stresses may be comparable to those modeled for Europa today.

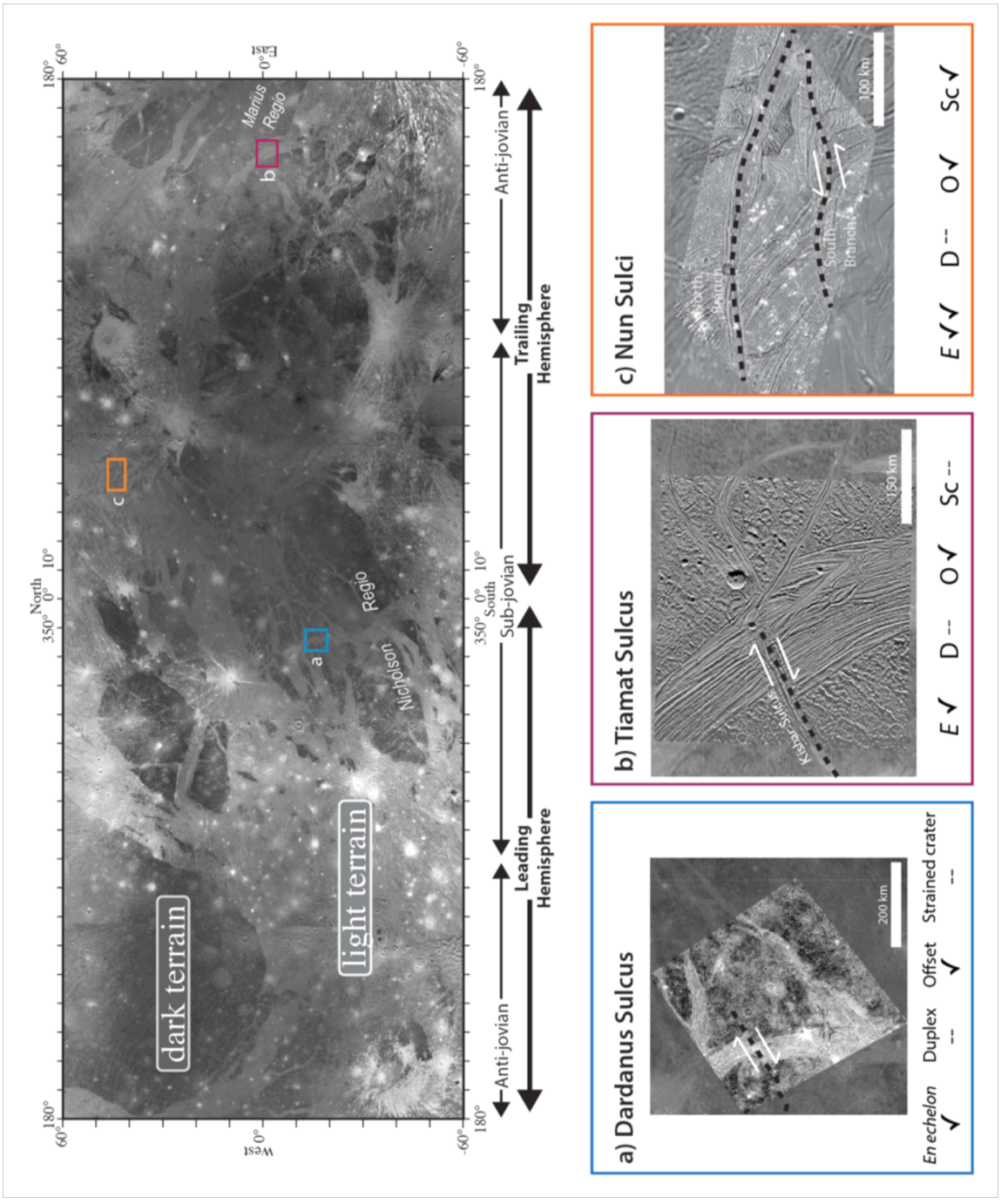

Figure 4.1: Ganymede global mosaic (0° – 360° E; 60°S - 60°N) in Mercator projection (modified from Cameron et al., 2018a). Examples of dark and light terrain are labeled; labeled boxes (a-c) denote sites where inferred fault zones were mapped for this study. (a-c) Galileo imagery and inferred fault zones (black dashed lines). White half arrows indicate inferred sense of shear. Strike-slip indicators within mapped Ganymede sites are also labeled: **E* - *En echelon* structures; D - Strike-slip duplexes; O - Offset features; Sc - Strained craters. Check marks indicate presence of strike-slip indicators and double check marks indicate that the region displays many instances of that strike-slip indicator

2. Ganymede's Orbital Evolution

Orbital resonances between Io, Europa, and Ganymede create a dynamic system that may have a strong effect on a satellite's thermal evolution (Showman and Malthotra, 1997). In the Galilean system, the strongest interactions occur between Io and Europa, and Europa and Ganymede. The current arrangement of this three-body system is known as a Laplace resonance, or a 1:2:4 orbital period ratio between Ganymede, Europa, and Io, respectively. While secular perturbations from Callisto are considered in analyses by Malhotra (1991) and Showman and Malhotra (1997), their effects are not essential to this study, and not discussed further. Many previous studies have explored the orbital history of the Galilean system and the potential effects on a satellite's eccentricity (Yoder, 1979; Yoder and Peale, 1981; Greenberg, 1987; Tittemore, 1990; Malhotra, 1991; Showman and Malhotra, 1997). Yoder and Peale (1981) determined an analytical solution for eccentricity variations in an attempt explain Io's high rate of external activity, however, Malhotra (1991) later showed that the Yoder-Peale solution was non-unique and suggested their proposed path towards the current resonance state was unlikely due to the high probability of capture into a Laplace-like resonance instead. Indeed, Showman and Malhotra (1997) revisited the Malhotra model to explore a wider range of conditions and found a high probability that the Galilean satellites would have been temporarily captured (for a period of $10^7 - 10^9$ years) in two Laplace-like resonances before reaching the current state. This is significant for Ganymede's evolution in that these resonances may have pumped Ganymede's past eccentricity to as high as ~0.07, potentially allowing for tidal dissipation to drive internal activity (Greenberg 1987; Malhotra, 1991; Showman and Malhotra, 1997). As eccentricity calculations depend on the past ratio of tidal dissipation between Ganymede and Jupiter, we choose a value of 0.05 to represent a conservative estimate.

The total orbital eccentricity of a satellite is found by the sum of the forced and free components, where each component is treated as a vector. If both forced and free vectors are in the same direction, the total eccentricity is simply the sum of the magnitudes of each component. If the forced component has a different direction than that of the free component, the total eccentricity must then be less that the sum of the magnitudes of each component.

The free component arises from a combination of the distance and velocity of a satellite after it formed around its parent planet. The forced component, however, arises from the gravitational interaction of two satellites whose orbital periods are in resonance, and therefore the forced component direction continuously changes, thus continuously changing the total eccentricity. We thus use the free eccentricity component when describing the eccentricity of Ganymede. It is worth noting that Showman and Malhotra (1997) suggest Ganymede's current free eccentricity (0.0013) to be higher than expected, and also is unlikely to have been produced by a cometary impact, further suggesting the current eccentricity is representative of some primordial value.

3. Tidal stress and Coulomb failure modeling

Ganymede is a synchronously rotating satellite, meaning that the same side of the satellite always faces Jupiter (Burns, 1976; Melosh, 1977; Helfenstein and Parmentier, 1980), causing Ganymede to experience a tidal bulge due to the difference in gravitational attraction of Jupiter. The varying gravitational potential within Jupiter's gravitational field causes tidal stresses and deformation as portions of Ganymede are subjected to these gravitational effects (Wahr et al., 2009). Additionally, Ganymede's orbit is elliptical (i.e., an eccentricity of greater than zero, and less than 1), allowing the tidal bulge to vary in both magnitude and longitudinal position as it changes distance from Jupiter during its diurnal orbit (Murray and Dermott, 1999). Moreover, the influence of tides affects both orbital and rotational evolution, and provides a major source of stress and heat (Peale, 2003); observed regions of strike-slip tectonism on Ganymede may be due, in part, to a combined effect of temporally varying stresses (Cameron et al., 2018b).

Here we focus on diurnal stress as the primary mechanism of tidal deformation due to a past, high eccentricity. As Ganymede orbits Jupiter, variable diurnal stresses sweep across the surface over a period equal to that of the satellite's orbital (diurnal) period, or 171.6 hours. Diurnal tidal stresses may be quite relevant to the formation of Ganymede's terrain; previous studies have suggested that diurnal tidal stresses are (1) responsible for the formation of Europa's ridges (Greenberg et al., 1998; Hoppa et al., 1999; Nimmo and

Gaidos, 2002), and (2) may trigger geological activity along fractures of Enceladus (Showman and Malhotra, 1997; Hurford et al., 2007; Nimmo et al., 2007; Smith-Konter and Pappalardo, 2008; Olgin et al., 2011).

To investigate the effects of these varying stresses for a past, high eccentricity, we use numerical model SatStress (http://code.google.com/p/satstress). SatStress (Wahr et al., 2009) calculates tidal stresses at any point on the surface of a satellite based on tidal potential theory (e.g., Wahr, 1981), allowing for both elastic and layered Maxwell viscoelastic treatments of the lithosphere (i.e., Smith-Konter and Pappalardo, 2008; Olgin et al., 2011, Cameron et al., 2018b). As a proof of concept, we use SatStress to model the diurnal stress of two end-member models: (1) Ganymede today (present-day, low eccentricity e = 0.0013), and (2) Ganymede in the past (using a conservative past high eccentricity e = 0.05).

We consider a simplified model of the internal structure of Ganymede (Figure 4.2) to simulate tidal stresses in the outer ice shell. Table 4.1 describes the model parameters for a present and past layered Ganymede represented by a spherically symmetric ice shell underlain by a global subsurface ocean and a deep interior. We represent Ganymede's outer ice shell as divided into two mechanically distinct layers whose properties are governed by the strong temperature dependence of ice I (Goldsby and Kohlstedt, 2001). For the present model, we assume an upper rigid layer 10 km thick and a more ductile ice shell extending another 140 km. For the past model, we assume an upper rigid layer 2 km thick, and a more ductile ice shell extending another 98 km deep. The upper layer of cold ice in both models is stiff ($\eta = 10^{19}$ Pa s), while the warmer ice in the interior of the ice shell has a viscosity that approximates ice I near its melting temperature ($\eta = 10^{14}$ Pa s, Showman et al., 1997; Goldsby and Kohlstedt, 2001; Mitri and Showman, 2005). Both layers have an ice I density of $\rho = 920$ k/m^3. Beneath the base of the ice shell, we impose an inviscid interior ocean with a density of $\rho = 1000$ kg/m^3. Beneath the ocean, we assume a deep interior that includes the high-pressure phases of ice predicted at the ocean-core interface, as well as a rocky core. The density and thickness of this layer varies with the assumed fraction of high-pressure ice (Figure 4.2). For a past, high eccentricity, tidal heat production was likely higher than present day, and we assume that more of the ice I shell and high-pressure ice layer in the deep interior would have melted when compared to the present day model. Thus, we reduce the

thickness of the ice shell and the deep interior by 50 km each (correcting the density of the deep interior layer to account for this loss), and correspondingly increase the thickness of the ocean layer by 100 km for the past model (Moore and Schubert, 2003). For the purpose of these layered models, we do not consider the volumetric change associated with melting ice.

Degree-two diurnal love numbers (Table 4.1) for this assumed rheology were derived using a companion Love number code available in the SatStress package (J. Wahr, personal communication, 2011) and were verified by alternative models (Moore and Schubert, 2003; F. Nimmo, personal communication, 2013). Love numbers are found to be similar for the present and past Ganymede structures that we assumed. Thus, the primary difference in our two end-member models is the significant change in Ganymede's eccentricity, which is manifested as increased diurnal stress magnitude for the past Ganymede model.

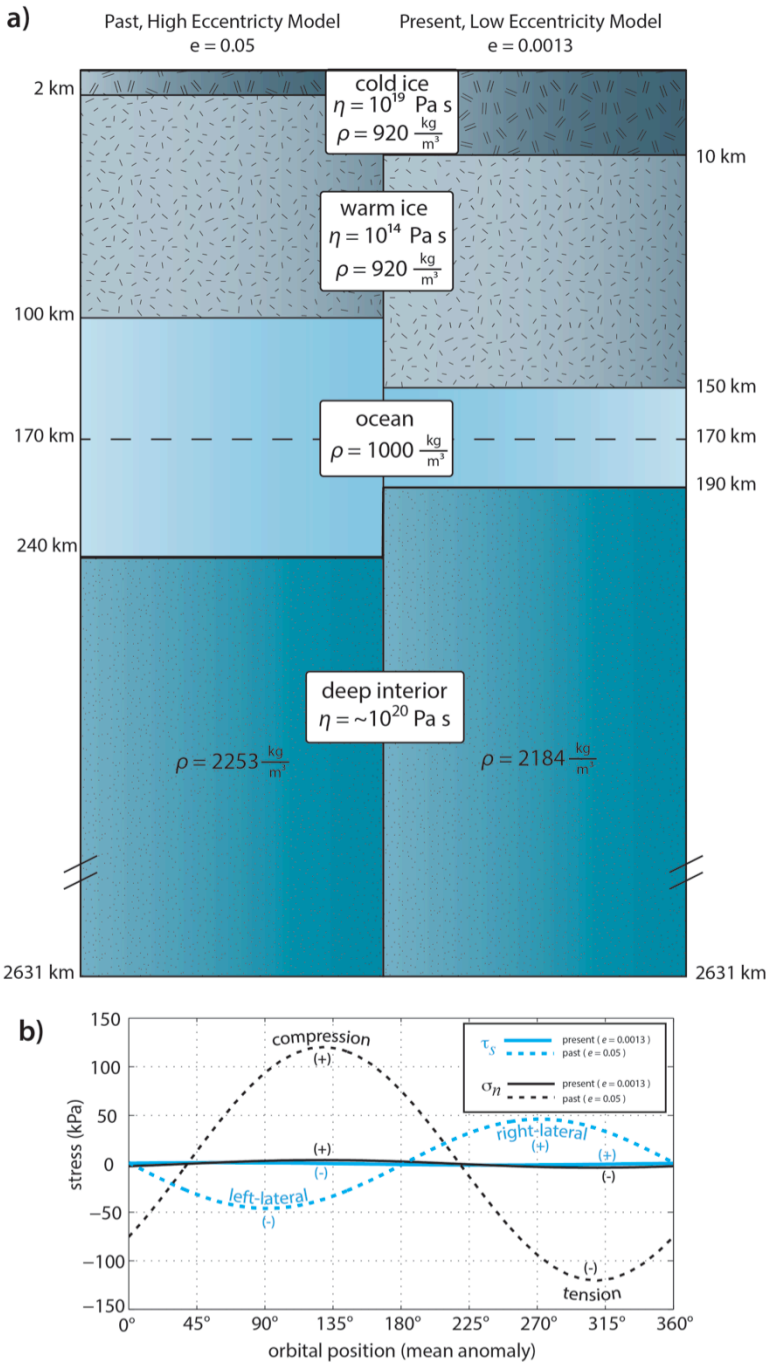

Figure 4.2: Comparison of past and present Ganymede internal structure and resulting tidal stress amplification due to variation in eccentricity. (a) The internal structure and rheology assumed for the two end member models used in this study. Note the deep interior includes high-pressure phases of ice predicted at the ocean-core interface, as well as a rocky core. (b) Diurnal shear (τ_s) and normal (σ_n) tractions at Dardanus Sulcus as a function of orbital position (mean anomaly, m). Solid lines represent Ganymede today (e = 0.0013) and dashed lines represent past, high eccentricity Ganymede (e = 0.05). At this example location, peak absolute stress magnitudes for Ganymede today approach ~4 kPa (normal) and ~1 kPa (shear). For a past Ganymede model, peak normal traction magnitudes reach 120 kPa and shear traction magnitudes approach 50 kPa. These past Ganymede diurnal stresses are comparable to those modeled for Europa today.

Table 4.1: Ganymede physical, orbital and rheological model for both a past (high) eccentricity and present day (low) eccentricity model.

Physical and Orbital Characteristics		
	Past	**Present day**
Satellite radius (km)	2630	2630
Satellite orbit eccentricity	.05	0.0013
Satellite orbit semi-major axis (km)	1.07×10^6	1.07×10^6
Satellite gravity (m/s^2)	1.428	1.428
Planet mass (kg)	1.90×10^{27}	1.90×10^{27}

Viscoelastic Parameters		
Ice (Upper and Lower)	**Past**	**Present day**
Young's modulus (GPa)	9.30	9.30
Shear modulus (GPa)	3.49	3.49
Poisson's ratio	0.30	0.30
Density (kg/m^3)	920	920
	Upper ice layer	Upper ice layer
Thickness (km)	2	10
Viscosity (Pa s)	10^{19}	10^{19}
	Lower ice layer	Lower ice layer
Thickness (km)	98	140
Viscosity (Pa s)	10^{14}	10^{14}
Ocean		
Young's modulus (GPa)	0	0
Shear modulus (GPa)	0	0
Poisson's ratio	0.50	0.50
Density (kg/m^3)	1000	1000
Thickness (km)	140	40
Viscosity (Pa s)	0	0
Deep Interior (high-phase ice + silicates)	**Past**	**Present day**
Young's modulus (GPa)	100	100
Shear modulus (GPa)	40	40
Poisson's ratio	0.25	0.25
Density (kg/m^3)	2253	2184
Thickness (km)	2391	2441
Viscosity (Pa s)	$\sim 10^{20}$	$\sim 10^{20}$

SatStress Parameters		
	Past	**Present day**
Period (yrs)	1.42×10^7	1.42×10^7
Elastic love number h_2	1.444	1.427
Elastic love number l_2	0.3765	0.3641

Coulomb failure theory relates the resolved shear and normal tractions on a fault plane; shear tractions drive strike-slip motions, while normal tractions control a fault's frictional resistance to failure (e.g. Byerlee, 1978; Brace and Kohlstedt, 1980). SatStress computes both raw ($\sigma_{\varphi\varphi}$, $\sigma_{\theta\theta}$, $\sigma_{\theta\varphi}$ or latitudinal, longitudinal, and shear tractions, respectively) and diagonalized (principal) stress tensor components as a function of orbital position past periapse (i.e., the mean anomaly, m) and geographic location on the satellite. Following the methodology of previous studies (Hurford et al., 2007; Nimmo et al., 2007; Smith-Konter and Pappalardo, 2008), we resolve tidal stress tensor components onto discrete fault segments, of varying length and orientation, into normal (σ_n) and shear (τ_s) traction components:

$$\tau_s = \frac{1}{2}\left(\sigma_{\phi\phi} - \sigma_{\theta\theta}\right) sin2\beta + \sigma_{\theta\phi} cos2\beta$$

$$\sigma_n = \sigma_{\theta\theta} cos^2\beta + \sigma_{\phi\phi} sin^2\beta + \sigma_{\theta\phi} sin2\beta \qquad \text{(Eq. 1)}$$

where β is a line segment orientation, defined with respect to the longitudinal direction (β = 0° for a fault oriented exactly east-west). Where applicable, we adopted mapped feature traces (i.e., measured trend with assumed vertical dip) from Cameron et al. (2018a); however, due to spare high-resolution imagery, we estimated fault geometry in some regions. Each sulcus is represented as a series of digitized fault segments with lengths of 5 km or less, and with β that may vary from the overall strike of the major fault zone. For each individual fault segment, the resolved normal traction component acts perpendicular to each segment, while the resolved shear traction component acts parallel to each segment.

To investigate the roles of resolved shear and normal tractions, we employ the Coulomb failure criterion (Byerlee, 1978; Jaeger and Cook, 1979) to assess the failure potential of individual fault segments. This criterion considers stresses that facilitate (tensile) and resist (compressive) slip, with faulting simultaneously accounting for both resolved normal and shear tidal traction, the coefficient of friction of ice, and additional stress at depth due to the overburden pressure (Thatcher and Hill, 1991). To model this behavior, we calculate the Coulomb stress as

$$\tau_c = |\tau_s| - \mu_f(\sigma_n + \rho g z), \qquad \text{(Eq. 2)}$$

where μ_f is the effective coefficient of friction and ρgz is the maximum overburden pressure (positive z is the vertical depth of the fault plane beneath the surface). Note the actual overburden pressure could be less than this, we conservatively assume the overburden pressure translates 1:1 to the lateral pressure acting on the fault. The sign of the overburden stress is taken to be positive, while normal tidal tractions are assumed positive when in compression and negative when in tension. The sign of the shear traction (positive for right-lateral, negative for left-lateral) becomes important when inferring the sense of slip when the failure conditions are met. Compressive tractions work to clamp a fault together, thus enhancing the frictional resistance and inhibiting failure, and require higher shear tractions to overcome the failure criterion. Alternatively, tensile tractions work to unclamp a fault, reducing the frictional contact between fault surfaces and encouraging failure if the acting shear traction is large enough. In general, the failure criterion is most easily met when tensile tractions dominate.

For simplicity, we will refer to the rightmost quantity of Eq. 2 that includes μ_f as the "frictional stress." Thus, for Coulomb failure to occur, the tidal shear traction on a fault must be greater than the frictional stress. According to this model, Coulomb failure will occur on optimally oriented fault segments when the shear traction exceeds the frictional resistance of the fault. Thus positive Coulomb stresses imply conditions supporting fault slip, while negative Coulomb stresses imply a locked fault. Because the Coulomb criterion only applies for a closed fault interface, we evaluate the role of fault depth for both normal tensile and compression regimes separately. For compressive tractions with no melting, no minimum fault depth limitation applies, as a fault interface will always be closed. For tensile zones however, the overburden stress must be larger than the tensile traction, otherwise a fault would dilate. Using the z-depth dependence of overburden stress in this manner, we evaluate the depth sensitivity of Coulomb failure for each fault zone at 0.1 km discretized depth observation planes.

4. Results

For completeness, we first evaluate the opportunity for Coulomb failure of a fault zone resulting from diurnal tidal stresses with a present-day eccentricity (Figure 4.3). We demonstrate the regional sinusoidal nature of resolved normal and shear tractions over a complete diurnal cycle for Dardanus Sulcus, Tiamat Sulcus, and the southern branch of Nun Sulci. We discretize each fault zone into many short (< 5 km) segments and calculate tractions along their midpoints. As segments may have varying orientations across the fault length (~ 30° of variation for Dardanus Sulcus, 20° for Tiamat Sulcus, and 30° for Nun Sulci's south branch), a range of diurnal stress patterns are estimated along the full length of each fault zone. To generalize this variation, we present the mean of these, which serves as a representation of each fault zone's along-strike behavior. Moreover, shear and normal tractions peak as a function of mean anomaly position depending on the geographic location of each fault zone. We assume a nominal depth of z = 100 m and a coefficient of friction of μ_f = 0.2. If the shear traction (blue line), at any mean anomaly position (orbital position) m, exceeds the magnitude of the frictional stress (red dashed line), Coulomb failure is achieved. We find that the tractions required for failure are approximately an order of magnitude larger than the diurnal shear tractions produced by the models, and therefore, Coulomb failure is not achieved when considering a present-day eccentricity (Cameron et al., 2018b). For example, the present-day mean diurnal normal traction at Dardanus Sulcus is small (4.5 kPa) and compressive for m = 30 – 230° and then becomes small and tensile (-4.5 kPa) for m = 230 – 30°; the present-day mean shear traction is also small (<1 kPa) and left-lateral for m = 45 – 225° and then right-lateral for m = 225 – 45°. The mean frictional stress (red line) for μ_f = 0.2 at 100 m depth is 28±1.5 kPa, which is nearly triple the magnitude of diurnal shear tractions needed to drive failure. The low coefficient of friction assumed here, μ_f = 0.2, is a conservative end member for ice (Fortt and Schulson, 2007; Schulson and Fortt, 2012); a higher coefficient of friction (i.e., μ_f = 0.6) yields an even higher mean frictional stress of 85±2 kPa. Hence, a fault segment of Dardanus Sulcus is expected to remain locked throughout its diurnal orbital cycle given this range of stresses.

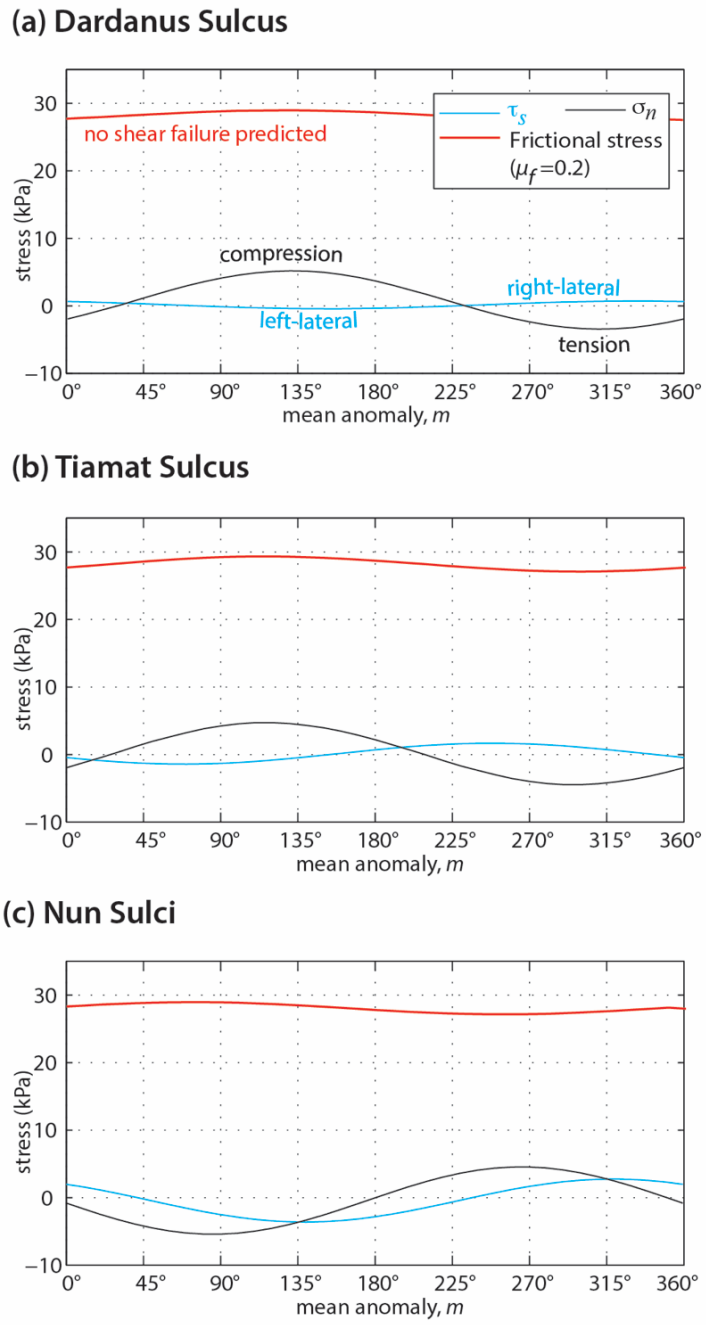

Figure 4.3. Modeled tractions on faults experiencing diurnal stresses for a present eccentricity. (a) Dardanus Sulcus, located in the sub-Jovian leading hemisphere, (b) Tiamat Sulcus, located in the anti-Jovian trailing hemisphere, and (c) Nun Sulci, located in the sub-Jovian trailing hemisphere. The mean resolved normal traction (black), shear traction (blue), and frictional stresses (red line, calculated at z = 100 m and μ_f =0.2) are provided. Negative resolved normal tractions are tensile, while positive normal tractions are compressive; negative resolved shear stresses are left-lateral while positive shear stresses are right-lateral. Shear failure is never achieved from diurnal stresses alone, given their very small magnitudes. Figure adapted from Cameron et al. (2018b).

Next we evaluate the opportunity for Coulomb failure of a fault zone subject to a much larger orbital eccentricity (Figure 4.4). We find that for a past, high eccentricity, both normal and shear tractions are larger in magnitude than for the present day eccentricity, although they follow the same pattern of transition between compressive-to-tensile or left-to-right-lateral regimes throughout an orbit. Frictional stress is also larger, however a combined effect of increased normal and shear tractions allows for slip windows (gray regions; Figure 4.4), or a continuous range of mean anomaly positions where the Coulomb criterion for failure is met. Additionally, these slip windows may allow for either right- and left-lateral slip along a fault zone depending on orbital position, m. For example, past diurnal normal tractions at Dardanus Sulcus are large (as great as 120 kPa) and compressive for m = 40 – 220° and then become large and tensile (as negative as -120 kPa) for m = 220 – 40°; shear tractions are smaller (as great as 50 kPa) and left-lateral for m = 0 – 180° and right-lateral for m = 180 – 360°.

Failure in slip windows is estimated at each fault zone for diurnal cycles for a past, high eccentricity. We calculate the net sense of slip for cases with μ_f =0.6 and μ_f =0.2 from the slip windows and sense of slip predicted by the models of the three fault zones. At Dardanus Sulcus when considering μ_f =0.6, we find that the feature is free to slip in only one window, from m ~270° – 355°, where the sense of shear at this position is right-lateral. Thus, considering only the sense of shear, the net sense of slip is estimated to be right-lateral. For a low coefficient of friction, μ_f =0.2, Coulomb failure criteria are met only for a right-lateral slip window occurring at m = 260° – 20°. Thus, in the simplest form, net slip for this example at Dardanus Sulcus, is predicted to be right-lateral. For Tiamat Sulcus, considering the high friction case, we identify a single slip window with right-lateral slip from m = 225° – 325°. For a low coefficient of friction, the left-lateral slip window occurs from m = 350° – 95° and the right-lateral slip window occurs from m = 190° – 350°, also suggesting the net slip to be right-lateral. Along the south branch of Nun Sulci, a high friction model yields a slip window where the sense of shear is left-lateral, at m = 110° – 190° and a right-lateral slip window at m = 30° – 110°, implying no net sense of slip. Additionally, the low friction model also yields equal windows of left- and right-lateral slip. Interestingly, the net sense of slip modeling estimates match strongly justified sense of slip inferences at both Dardanus and

Tiamat Sulcus from high-resolution imagery (Figure 4.1, also Cameron et al., 2018a).

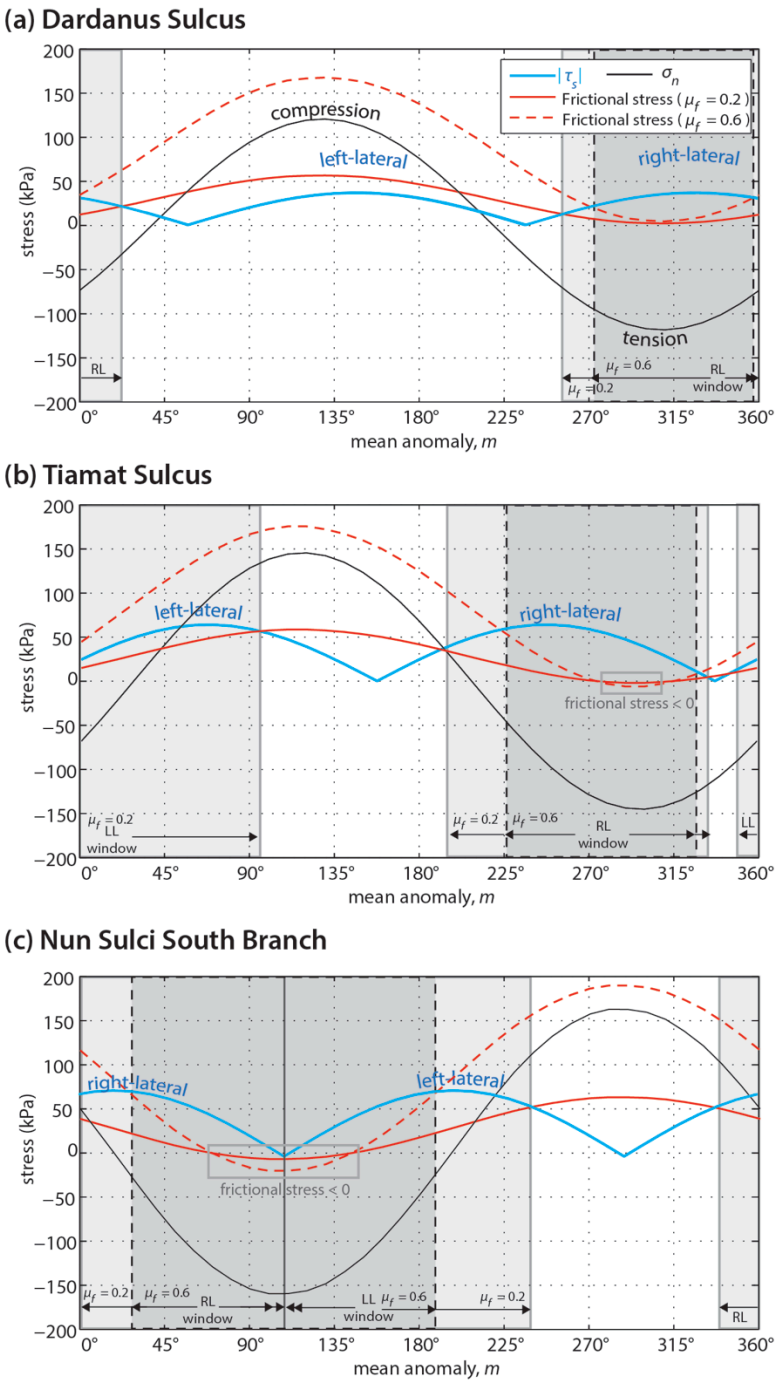

Figure 4.4. Modeled tractions on faults experiencing diurnal stresses for a past eccentricity. (a) Dardanus Sulcus, (b) Tiamat Sulcus, and (c) Nun Sulci. The mean modeled resolved normal traction (black), shear traction (blue), and frictional (red, calculated at z = 100 m and μ_f =0.2 (dashed) and μ_f =0.6 (solid) stresses are provided. As in Figure 4.3, negative resolved normal tractions are tensile, while positive normal tractions are compressive. Alternatively, the absolute value of shear stress is plotted here, to illustrate the occasional coinciding magnitudes of the frictional stress sinusoid. Gray shaded windows (light gray, μ_f =0.2; dark gray, μ_f =0.6) denote regions where the shear traction is greater than the frictional stress and Coulomb failure could be manifested as strike-slip. Gray outlined boxes indicate regions where frictional stress is < 0.

We next explore the implications of a past, high eccentricity orbit in map view at each fault zone (Figures 4.5 – 4.7). Map view results closely follow those from the sinusoids shown in Figure 4.4, with the exception that mean diurnal sinusoid (per fault zone) is represented in previous figures. In the interest of clarity and simplicity, we next show only four mean anomaly positions, m = 0°, 90°, 180° and 270°, acknowledging that the nuanced behavior of the stresses may be diminished. For example, map view results of Dardanus Sulcus (Figure 4.5) indicate that the fault zone transitions from tensile to compressive tractions between m = 0° and 90°, and back to a tensile regime by m = 270°, but the precise mean anomaly position of this transition is observed only in the sinusoidal data presented in Figure 4. Still, the map view plots (Figures 4.5 – 4.7) provide the ability to make observations regarding the sensitivity of shear and normal tractions to fault strike. As an example, when examining shear tractions, the mid-section of Dardanus Sulcus has a more northern strike that behaves opposite to the less northern striking sections on either side, regardless of mean anomaly position. When inspecting Coulomb stress, this same section also varies in magnitude and is especially noticeable when consider a lower μ_f. We explore this sensitivity to fault strike in great detail in Cameron et al. (2018b). Tiamat Sulcus (Figure 4.6) is more linear than Dardanus Sulcus, but changes in magnitude are also observed in shear traction and Coulomb stress for the less northern striking section. We note that there are also a few segments along Tiamat spanning the last quarter of Ganymede's orbit where Coulomb failure theory does not apply due to high tensile stresses that exceed the overburden strength. Similar patterns are observed along both branches of Nun Sulci (Figure 4.7), specifically where sections of the fault that strike southeast (e.g., near the midpoint of the southern branch) behave similarly to the southeast striking sections of the northern branch, but with varied magnitude when compared to the northeast striking sections. In all cases, increasing μ_f reduces the likelihood of Coulomb criterion failure to be met. While Figures 4.5 – 4.7 highlight results for a z value of 100 m, we find Coulomb failure along all fault zones may be possible down to an average depth of 250 m for μ_f = 0.2.

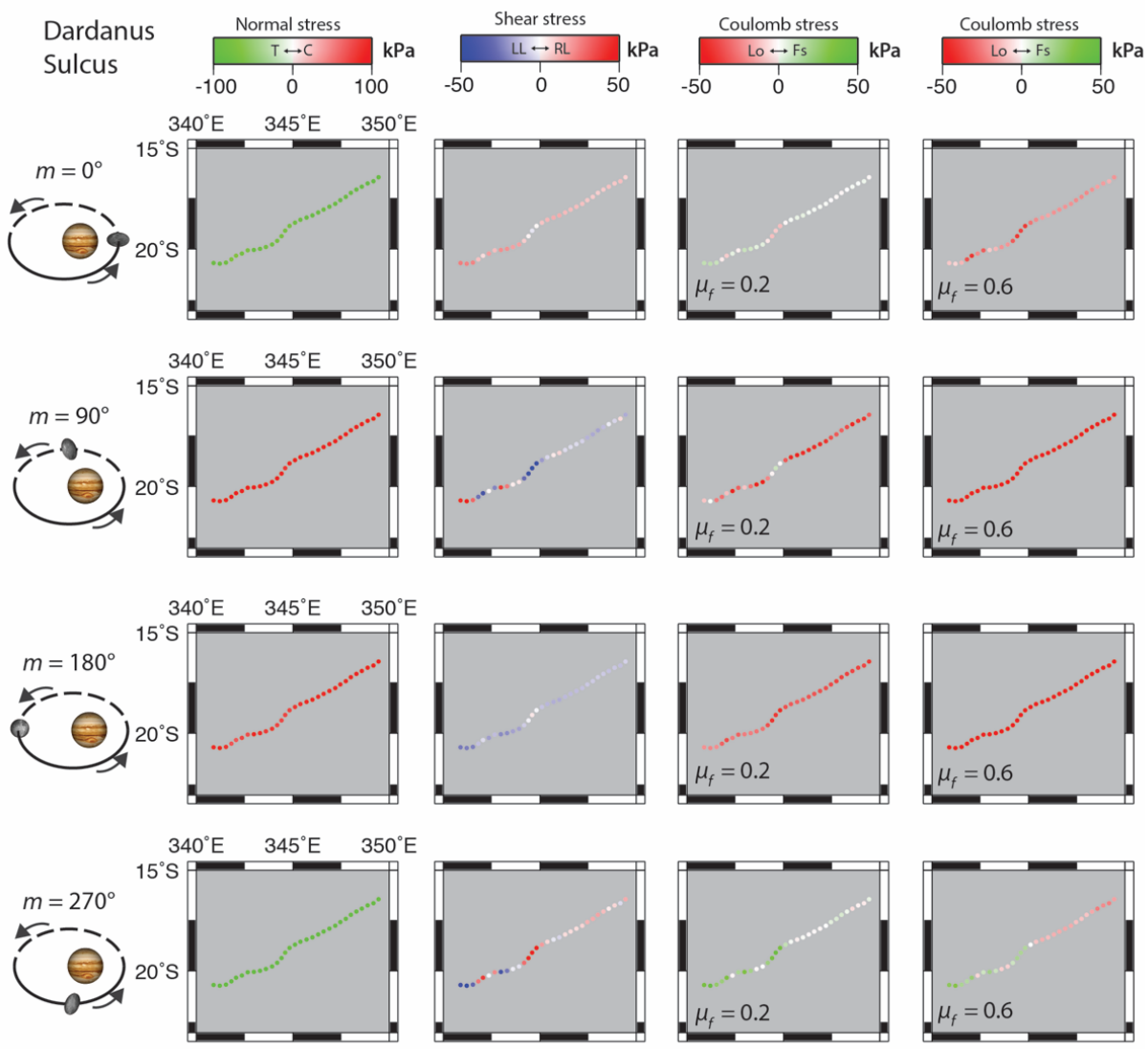

Figure 4.5. Map view representation of normal traction, shear traction, and Coulomb failure stresses of diurnal model along Dardanus Sulcus. (C = compression, T = tension), shear (RL = right-lateral, LL = left-lateral), and Coulomb stresses (Fs = indicating free to slip, Lo = locked) calculated at mean anomaly positions m = 0°, 90°, 180°, and 270°. Stresses are provided at an example depth of z = 100 m and for μ_f = 0.2 (low friction case) and 0.6 (high friction case).

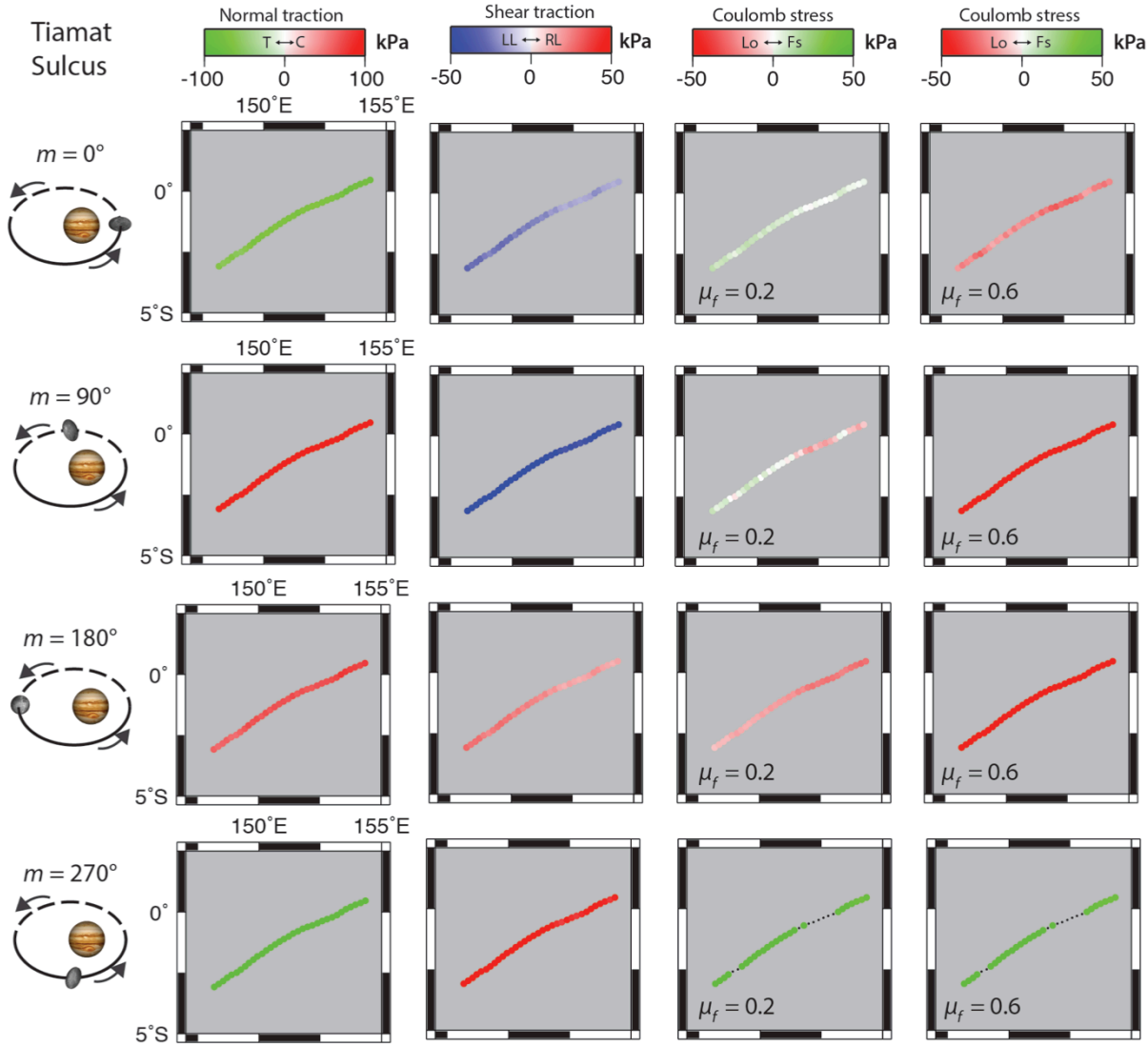

Figure 4.6. Map view representation of normal traction, shear traction, and Coulomb failure stresses of diurnal model along Tiamat Sulcus. (C = compression, T = tension), shear (RL = right-lateral, LL = left-lateral), and Coulomb stresses (Fs = indicating free to slip, Lo = locked) calculated at mean anomaly positions m = 0°, 90°, 180°, and 270°. Stresses are provided at an example depth of z = 100 m and for μ_f = 0.2 (low friction case) and 0.6 (high friction case). Black dots indicate plausible shallow slip zones, but not guided by the physics of Coulomb failure due to high tensile stresses.

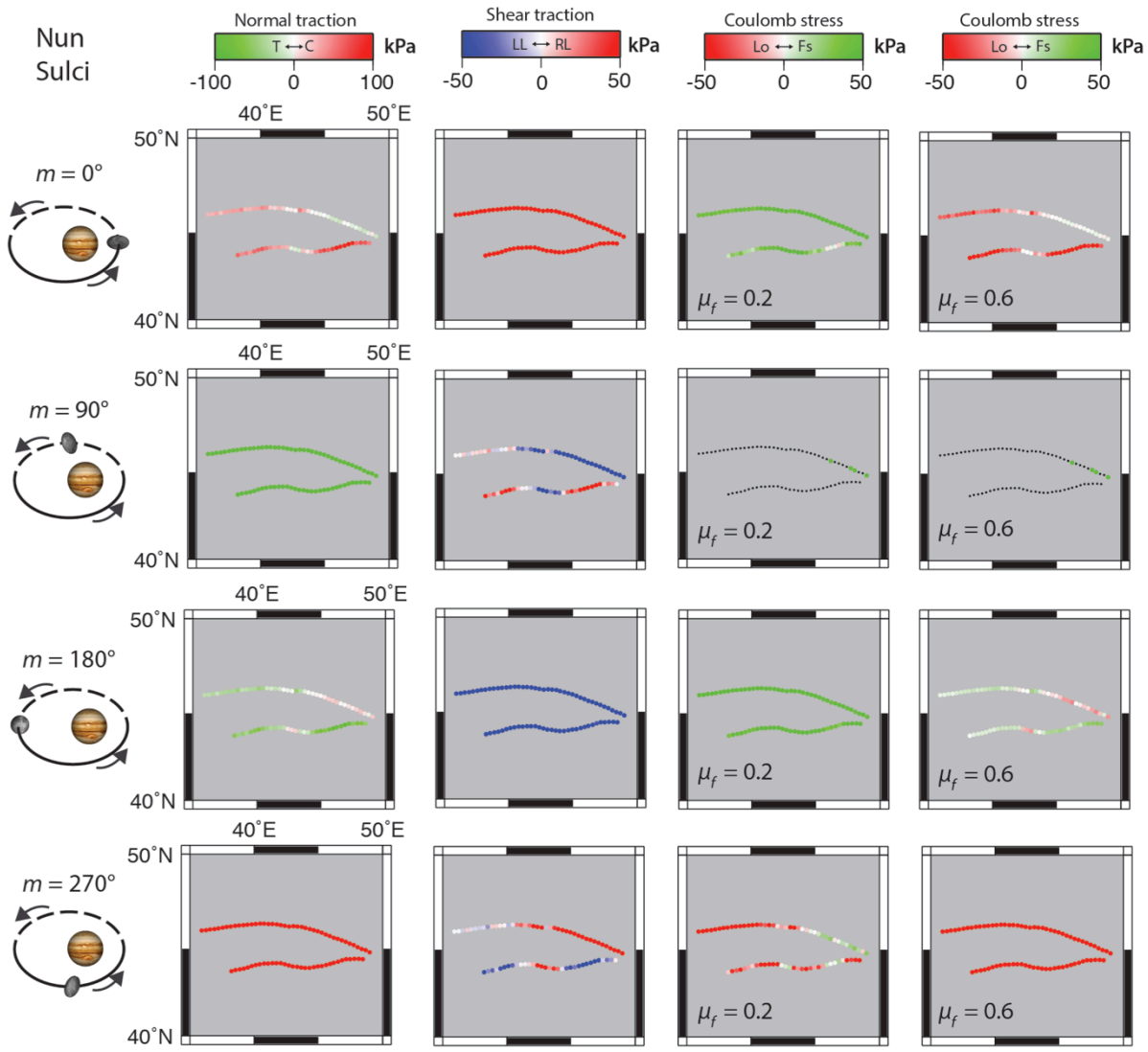

Figure 4.7. Map view representation of normal traction, shear traction, and Coulomb failure stresses of diurnal model along Nun Sulci. (C = compression, T = tension), shear (RL = right-lateral, LL = left-lateral), and Coulomb stresses (Fs = indicating free to slip, Lo = locked) calculated at mean anomaly m = 0°, 90°, 180°, and 270°. Stresses are provided at an example depth of z = 100 m and for μ_f = 0.2 (low friction case) and 0.6 (high friction case). Black dots indicate plausible slip zones, but not guided by the physics of Coulomb failure due to high tensile stresses.

6. Discussion

To illustrate the behavior of Coulomb failure on a larger scale, we next expand our analysis to a global perspective of Ganymede's stress field. As demonstrated in previous figures, a fault segment's resolved traction depends on its orientation. We attempt to capture (1) the dependency of traction on fault strike and (2) the time-dependent variability, by adopting the schematic representation of stress as a function of fault orientation (i.e., Hoppa et al., 1999; Rhoden et al., 2011; Cameron et al., 2018b), where all possible fault orientations are represented. We explore the dependency of hypothetical fault segments with varying orientations that span the global stress field (60°S - 60°N), represented by structures of 5° in length and of varying strikes centered within 96 grid cells spanning 15° latitude by 30° longitude. In Figures 4.8 – 4.9, we plot the Coulomb stress and resolved shear traction direction, respectively, as a function of position and strike, and note that only the sign of the quantity (Coulomb stress or shear) is represented here, whereas the magnitude of both of these quantities will also smoothly vary along strike. That is, we use a binary color scheme to identify regions of positive or negative stress, but the function varies smoothly from a minimum magnitude at the wedge boundaries (where colors change from gray to black) to maximum magnitudes at the circle centers. For simplicity, the results represent the stress regime at 100 m depth, μ_f = 0.2, and mean orbital positions m = 0°, 90°, 180°, 270°, consistent with previous figures.

Using this global perspective, we demonstrate the abundance of shear failure opportunities for strike-slip structures of Ganymede due to diurnal stresses when considering a past eccentricity (Figure 4.8). For this model, resolved shear and normal tidal stresses promote Coulomb failure along a wide range of geographic locations and fault orientations for each orbital position examined. Patterns of Coulomb failure as a function of fault orientation are noted to reflect about the equator and repeat across the central meridian (0° E). While m = 0° (periapse) and m = 180° (apoapse) are additionally reflected about a major axis at the central meridian, minor reflection patterns also appear at 90° intervals. At m = 90° and m = 270°, reflections occur at meridians of intervals 45° from 0° E. Alternatively, the global pattern of sense of shear as a function of fault orientation (Figure 4.9) displays an anti-

symmetric pattern across the equator and central meridian, and largely follow the shear stress tensor component ($\sigma_{\theta\varphi}$). In both figures, the locations and average strike of Dardanus, Tiamat, and Nun are also plotted (locations approximated by the grid cell of closest proximity), illustrating the dependency on fault orientation for each fault zone's preference for Coulomb failure and shear sense throughout an orbital cycle.

Examining sense of slip patterns of Figures 4.4 and 4.9 allows for consideration of a plausible case for tidal walking, where both right- and left- lateral slip episodes could be possible over a diurnal cycle, during Ganymede's high eccentricity past. We adopt three assumptions from the shell tectonics model (Rhoden et al., 2012) and Coulomb shear failure model (Smith-Konter and Pappalardo, 2008) for Ganymede: (1) we include tidal diurnal stress only (i.e., no secular stress), (2) we limit evaluation depths to the very shallow uppermost region of the ice shell, where overburden stress is very low (z = 100 m), and (3) we assume that strike-slip can occur in the directional sense of the applied stress only if the Coulomb failure criterion are met. Following this approach, as with the diurnal sinusoids shown in Figure 4.4, we find that when tracking a single hypothetical fault zone through different orbital positions, the fault zone may have the potential for both left- or right- lateral slip over a complete orbit, as described in Section 5. We note that the primary assumption of strike-slip occurring in the same directional sense of the applied stress, if the Coulomb failure criterion are met, is a deviation from Rhoden et al. (2012), which considers a net stress gradient. To test the uniqueness of the Rhoden model, we next permit our quantification of sense of slip to account for shear stress gradients (i.e., positive stress slopes equate to left-lateral slip, and vice versa). With this model, Dardanus Sulcus has a net left-lateral slip for μ_f = 0.2 and 0.6, Tiamat Sulcus has a net right-lateral slip for μ_f = 0.2 and 0.6, and the south branch of Nun Sulci has a net right-lateral slip for μ_f = 0.2 and 0.6. We find the sense of slip predicted by this alternate method, with the exception of Tiamat Sulcus, is not in agreement with geologic evidence, and is not considered further. Future work aims to compile global sense of shear results from all mean anomaly positions evaluated against feasible slip windows as dictated by the Coulomb failure criterion to provide a means to evaluate a hypothetical faults behavior.

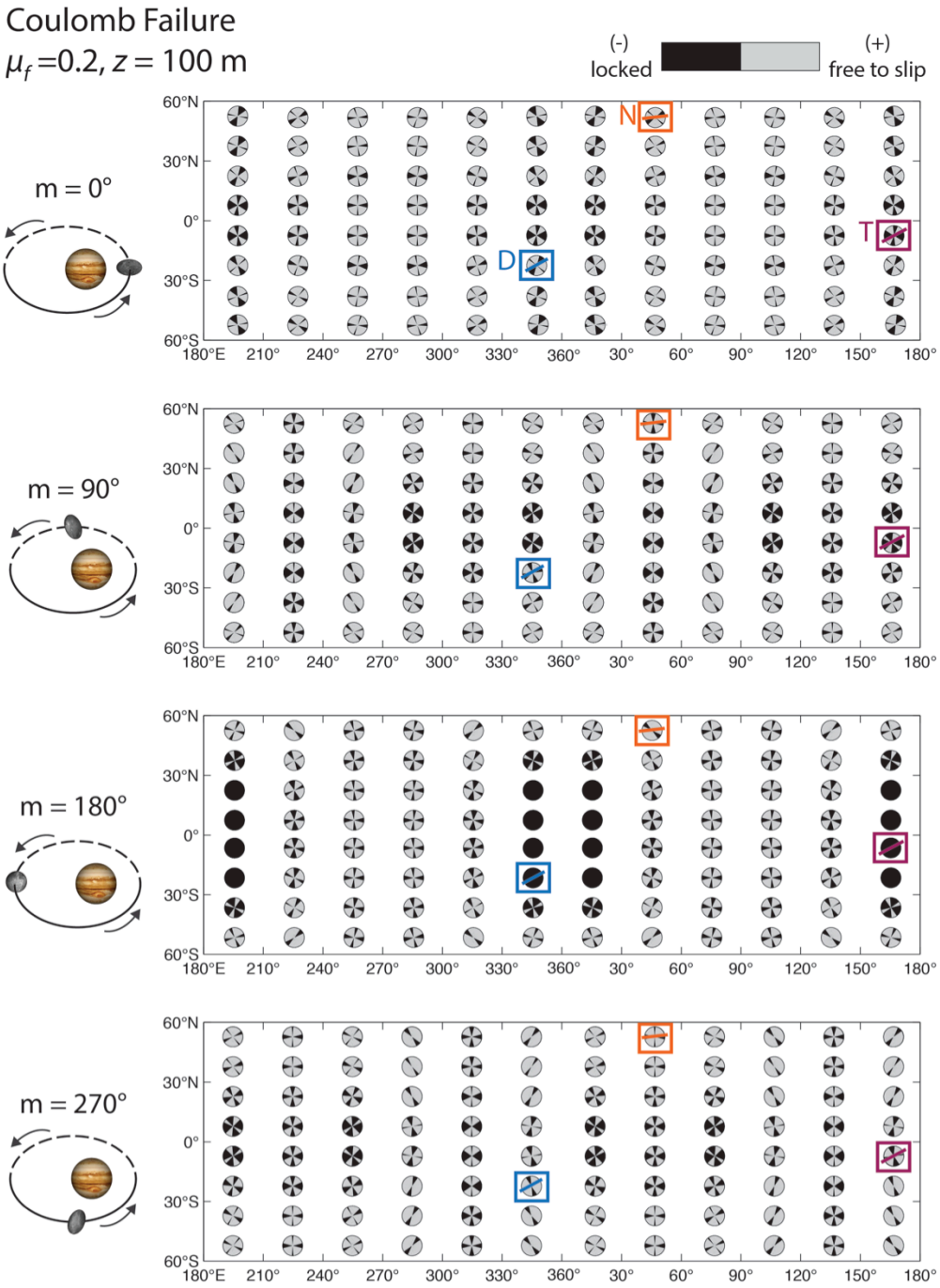

Figure 4.8: Global Coulomb failure predictions, and range of fault orientations permitting failure, for a past, high eccentricity model at mean anomaly m = 0°, 90°, 180°, and 270°. Mean anomaly position about Jupiter is illustrated on the left side of each map. Per circular schematic, zones shaded in gray represent possible fault orientations that exhibit positive Coulomb stress, and hence be free to slip at a z = 100 m depth, assuming a coefficient of friction of μ_f = 0.2. Alternatively, zones shaded in black represent possible fault orientations that exhibit negative Coulomb stress, and hence would be locked. Blue, purple, and orange outlined boxes correspond to mapped regions as shown in Figure 4.1. Similarly, blue, purple, and orange line segments represent the approximate strike of the corresponding fault zones. D: Dardanus Sulcus. T: Tiamat Sulcus. N: Nun Sulci.

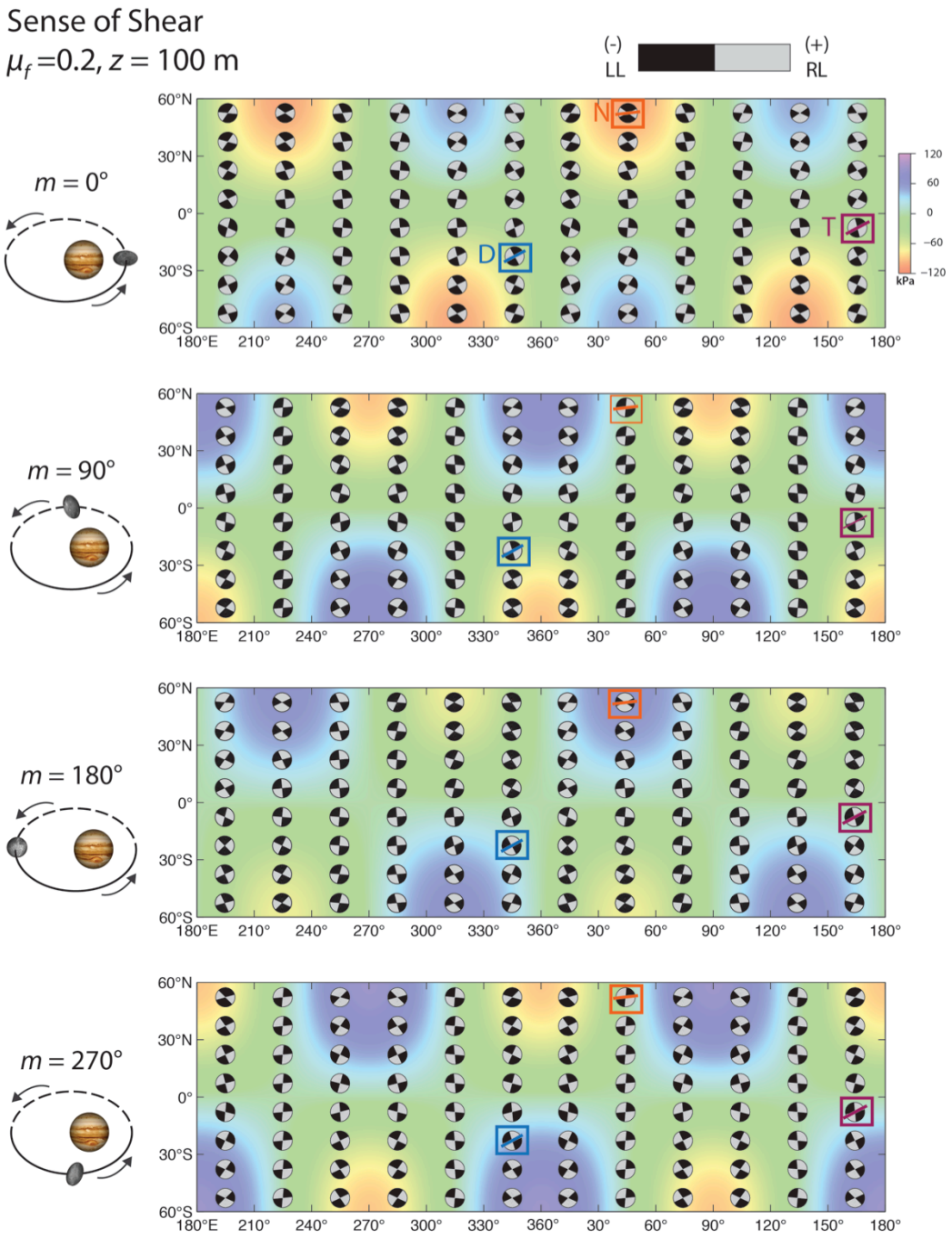

Figure 4.9: Global sense of shear predictions, either right-lateral (RL) or left-lateral (LL) for a past, high eccentricity model at mean anomaly m = 0°, 90°, 180°, and 270° overlaying stress tensor component $\sigma_{\theta\varphi}$ (kPa). Mean anomaly position about Jupiter is illustrated on the left side of each map. Per circular schematic, zones shaded in gray represent possible fault orientations that exhibit right-lateral slip at a z = 100 m depth, assuming a coefficient of friction of μ_f = 0.2. Alternatively, zones shaded in black represent possible fault orientations that exhibit left-lateral slip. Blue, purple, and orange outlined boxes correspond to mapped regions as shown in Figure 4.1. Similarly, blue, purple, and orange line segments represent the idealized strike of the corresponding fault zones. D: Dardanus Sulcus. T: Tiamat Sulcus. N: Nun Sulci.

7. Conclusions

These results suggest that diurnal stresses on Ganymede today are quite small (<10 kPa) and do not permit Coulomb shear failure along any of the three major fault zones investigated here, nor along six other fault zones investigated by Cameron et al. (2018b). Diurnal stresses during a former period of high-eccentricity (~100 kPa), however, readily generate shear and normal traction magnitudes that promote Coulomb shear failure, though limited to shallow depths and isolated windows of slip. This model predicts a dominant (≥ 45° mean anomaly) right-lateral slip window for Dardanus Sulcus when considering both μ_f = 0.2 and 0.6. Tiamat Sulcus has a dominant right- and left-lateral slip window when only considering μ_f = 0.2, but is isolated to a dominant right-lateral slip window when considering μ_f = 0.6. The south branch of Nun Sulci has a dominant right- and left-lateral slip window when considering only μ_f = 0.2, but is isolated to a dominant left-lateral slip window when considering μ_f = 0.6. These models match the sense of inferred shear from imagery and structural mapping efforts, with right-lateral offset inferred for Dardanus and Tiamat Sulcus, and left-lateral offset for Nun Sulci. Moreover, a low coefficient of friction (μ_f = 0.2) Coulomb failure model of right- and left- lateral slip episodes over a diurnal cycle could indicate a plausible case for tidal walking in Ganymede's high-eccentricity past. This past, high eccentricity provides stresses that may be comparable to Europa's current diurnal stresses, which are also considered to be sufficient to promote slip of faulted structures (Hoppa et al., 1999b; Kattenhorn and Hurford, 2009; Hurford et al., 2009).

Acknowledgments

We thank S. Martel, P. Lucey, S. Fagents, and P. Mouginis-Mark for constructive conversations that helped clarify this manuscript. The portion of this research by R.T.P. was carried out at the Jet Propulsion Laboratory, California Institute of Technology, under a contract with the National Aeronautics and Space Administration. This research was supported by the NASA Outer Planets Research Program (NNX14AE15G).

Author Contributions

M.C. performed all numerical calculations. M.C. created all images. B.S.K., G.C., D.P., and R.P., provided feedback on results. M.C. wrote the manuscript with consultation from all authors.

CHAPTER 5. CONCLUSIONS

5.1. Summary

This dissertation engages in a broad-ranging planetary investigation - connecting surface observations and morphological mapping to global tidal stress mechanisms that drive and evolve large-scale tectonism - of the largest moon in the solar system, Ganymede. This body of work is the first to study the occurrence and significance of strike-slip tectonism on Ganymede in significant detail, however the methods presented may be applied to many icy satellites. Beginning with a detailed morphological mapping study of nine areas of Ganymede's morphologically complex icy surface in Chapter 2, *Galileo* high-resolution imagery relationships and *Voyager* context imagery are used to infer tectonic domains of similar morphology, similar to how geologic units may be used on Earth. Unlike Earth, Ganymede's surface evolution is not well constrained, and age relationships rely almost exclusively on relative age dating. Through detailed mapping, this dissertation asserts that strike-slip tectonism has helped shape the terrain in addition to the more commonly studied extensional processes. This study finds strike-slip tectonism is present in all nine regions detailed. By noting local similarities in these mapped sites, which lie scattered across a broad geographical area, larger scale trends may be observed between locations that suggest a fingerprint of a shifting stress field through time. Future missions, specifically ESA's *JUICE*, will provide increased high-resolution image coverage and increased instrument analysis that will aid in strengthening the mapping observations presented in this study.

Now that strike-slip tectonism has been established as a contributor to the formation of Ganymede's terrain, we may consider the source of this tectonic activity in Chapter 3. Specifically, it is necessary to consider the effects of tidal stresses acting on Ganymede as it interacts with the dynamic Jupiter and Galilean satellite system. Thus, the conditions necessary for tidally driven Coulomb failure on Ganymede are likely due to two fundamental stress mechanisms: diurnal stresses, or the stress imparted on Ganymede solely due to its

orbit around Jupiter; and nonsynchronous rotation tidal stresses, a secular stress that may arise if the surface of the satellite is decoupled from its interior, in this case due to the global, subsurface liquid water ocean. These tidal stresses are modeled using the numerical code SatStress, and the Coulomb failure criterion is used to assess the resulting stresses.

While Ganymede's current eccentricity (e = 0.0013) yields diurnal stresses that are small (<10 kPa), stresses derived from the nonsynchronous rotation (NSR) of Ganymede's outer icy shell may yield shear and normal tractions on the order of ~1 MPa. This increase in magnitude of stresses owing to NSR ultimately provides stresses that are large enough to allow for strike-slip along fault zones. Stresses for a combined diurnal and NSR model (diNSR) indeed allow for strike-slip along each of the major fault zones identified in the nine regions mapped in detail in Chapter 2. Additionally, the compatibility of modeled sense of slip, either right- or left-lateral, inferred sense of slip from *Voyager* and *Galileo* images may be compared. Specifically, the models of this study predict the same sense of slip as inferences from mapping in six of nine regions, with the three incompatible areas perhaps being influenced by reorientation of the icy shell.

The dynamism of Ganymede's orbit within the Jupiter-Io-Europa system becomes even more important when considering the effects of much more eccentric orbit (e = 0.5) during Ganymede's past, as described in Chapter 4. When considering this model, diurnal stresses may be ~100 kPa, an order of magnitude larger than present day. These higher diurnal stresses may permit an abundance of strike-slip opportunities along fault zones of varying orientation, without the need to consider secular stresses such as NSR. These strike-slip failure opportunities are however limited to shallow depths (<250 m) and are highly dependent on Ganymede's orbital position, allowing for a transition between slip and locked zones as Ganymede's distance from Jupiter changes during a single orbit.

Combined, these three studies explore past and modern tectonic history at Ganymede, and will hopefully provide a significant contribution to the body of Ganymede and icy moon,

literature. Given the renewed interest in future missions to Jupiter and its Galilean moons, this dissertation documents one of the first attempts to perform detailed analysis of the role of strike-slip tectonism. While this work provides the initial framework for future analyses of its kind, it also reveals several areas for improvement.

5.2. Future Work

5.2.1. Directions for Modeling

This study focused primarily on use of the Coulomb failure criterion to assess slip along an inferred fault zone. In short, for Coulomb failure to occur, the tidal shear traction on a fault must be greater than the frictional stress. However, because the Coulomb failure criterion only applies for a closed fault interface, the criterion is not applicable in areas of high tensile tractions. This does not mean that that these high tensile regions are not plausible zones of slip, only that the type of slip that might occur here was not modeled. Future modeling efforts then should explore other failure mechanics models that include high tensile regions, especially since these regions typically occur in the shallow subsurface, an area of focus for instruments onboard spacecraft collecting data.

5.2.2. Upcoming Spacecraft Missions

The current lack of global coverage of Ganymede from decades-past surveys inhibits mapping the most complex features, and makes it difficult to expand from regional to more global observations. This is where improved imagery and geophysical data, such as the type of data anticipated from *JUICE* will greatly refine existing models of Ganymede tectonics. The science payload aboard *JUICE* will include a comprehensive remote sensing package, consisting of multiple spectral imaging instruments (MAJIS, Moons And Jupiter Imaging Spectrometer; UVS, Ultraviolet Spectograph; and SWI, Submillimeter Wave Instrument) and an optical camera (JANUS, Jovis, Amorum ac Natorum Undique Scrutator) capable of a 2.4

m spatial resolution (Della Corte et al., 2014).

Additionally, the processes that drive ice shell tectonics and the forces associated with decoupling between the ice shell and interior are not well understood. Here, the geophysical package on *JUICE* will be key: GALA (GAnymede Laser Altimeter) will study the tidal deformation of Ganymede and the morphology and topography of the surfaces of the icy moons (Lingenauber et al., 2014), while RIME (Radar for Icy Moons Exploration) uses ice penetrating radar to characterize the subsurface structure of icy moons (Bruzzone et al., 2013). Specifically, data from spacecraft based radar may help constrain thicknesses of near surface features, ultimately allowing for improved inputs in geodynamic models. Additionally, J-MAG (*JUICE* Magnetometer) will further investigate the interaction of Jupiter's magnetic field with the internal magnetic field of Ganymede (both intrinsic and induced) and may provide more information about the subsurface ocean (Plaut et al., 2014). While Ganymede is not a target for NASA's flagship mission, *Europa Clipper*, will carry a comparable science payload to study Europa, providing additional context for icy tectonics. In conclusion, this body of research strengthens the scientific foundation that will support planned future missions to Jupiter and its Galilean moons.

REFERENCES

Anderson, J.D., Laing, P.A., Lau, E.L., Liu, A.S., Nieto, M.M., and Turyshev, S.G., 1998, Indication, from Pioneer 10/11, Galileo, and Ulysses Data, of an Apparent Anomalous, Weak, Long-Range Acceleration: Physical Review Letters, v. 81, p. 2858–2861, doi: 10.1103/PhysRevLett.81.2858.

Anderson, J.D., Lau, E.L., Sjogren, W.L., Schubert, G., and Moore, W.B., 1996, Gravitational constraints on the internal structure of Ganymede: Nature, v. 384, p. 541, doi: 10.1038/384541a0.

ASCN, 1961, American Code of Stratigraphic Nomenclature: Am. Assoc. Petroleum Geol. Bull., p. 645–660.

Basilevsky, A.T., Pronin, A.A., Ronca, L.B., Kryuchkov, V.P., Sukhanov, A.L., and Markov, M.S., 1986, Styles of tectonic deformations on Venus: Analysis of Venera 15 and 16 data: Journal of Geophysical Research: Solid Earth, v. 91, p. 399–411.

Becker, T., Archinal, B., Colvin, T., Davies, M., Gitlin, A., Kirk, R.L., and Weller, L., 2001, Final digital global maps of Ganymede, Europa, and Callisto, in Lunar and Planetary Science Conference, v. 32.

Beeman, M., Durham, W.B., and Kirby, S.H., 1988, Friction of ice: Journal of Geophysical Research: Solid Earth, v. 93, p. 7625–7633.

Belton, M.J.S., Head III, J.W., Ingersoll, A.P., Greeley, R., McEwen, A.S., Klaasen, K.P., Senske, D., Pappalardo, R., Collins, G., Vasavada, A.R., Sullivan, R., Simonelli, D., Geissler, P., Carr, M.H., et al., 1996, Galileo's first images of Jupiter and the Galilean satellites: Science, v. 274, p. 9, doi: 10.1126/science.274.5286.377.

Bland, M.T., and McKinnon, W.B., 2017, Viscous relaxation as a prerequisite for tectonic resurfacing on Ganymede: Insights from numerical models of lithospheric extension: Icarus.

Bland, M.T., and Showman, A.P., 2007, The formation of Ganymede's grooved terrain: Numerical modeling of extensional necking instabilities: Icarus, v. 189, p. 439–456, doi: 10.1016/j.icarus.2007.01.012.

Brace, W.F., and Kohlstedt, D.L., 1980, Limits on lithospheric stress imposed by laboratory experiments: Journal of Geophysical Research: Solid Earth, v. 85, p. 6248–6252.

Bruzzone, L., Plaut, J.J., Alberti, G., Blankenship, D.D., Bovolo, F., Campbell, B.A., Ferro, A., Gim, Y., Kofman, W., Komatsu, G. and McKinnon, W., 2013. RIME: Radar for icy moon exploration. In Geoscience and Remote Sensing Symposium (IGARSS), 2013 IEEE International, p. 3907-3910.

Burns, J.A., 1976, Consequences of the tidal slowing of Mercury: Icarus, v. 28, p. 453–458, doi: 10.1016/0019-1035(76)90118-4.

Byerlee, J., 1978, Friction of rocks: pure and applied geophysics, v. 116, p. 615–626, doi: 10.1007/BF00876528.

Cameron, M.E., Nahm, A.L., Smith-Konter, B.R., and Pappalardo, R.T., 2012, Tidally Driven Coulomb Failure Along Europa's Agenor Linea, in Lunar and Planetary Science Conference, v. 43.

Cameron, M.E., Smith-Konter, B.R., Burkhard, L.M., Collins, G.C., Seifert, F., and Pappalardo, R.T., 2015, What causes an icy fault to slip? Investigating strike-slip failure conditions on Ganymede at Dardanus and Tiamat Sulcus., in AGU Fall Meeting Abstracts.

Cameron, M.E., Smith-Konter, B.R., Burkhard, L.M., Collins, G.C., Seifert, F., and Pappalardo, R.T., 2018a, Morphological mapping of Ganymede: Investigating the role of strike-slip tectonics in the evolution of terrain types: in review, Icarus.

Cameron, M.E., Smith-Konter, B.R., Burkhard, L., Patthoff, D.A., Pappalardo, R.T., and Collins, G.C., 2017, Strike-Slip Tectonism and Shear Failure on Ganymede, in Lunar and Planetary Science Conference, v. 48.

Cameron, M.E., Smith-Konter, B.R., Collins, G.C., Patthoff, D.A., and Pappalardo, R.T., 2018b, Tidal stress modeling of Ganymede: Strike-slip tectonism and coulomb failure: in review, Icarus.

Cameron, M.E., Smith-Konter, B.R., Collins, G.C., Patthoff, D.A., and Pappalardo, R.T., 2018c, Ganymede then and now: How past eccentricity may have altered tidally driven Coulomb failure: in preparation, Earth Planet. Sci. Lett..

Cameron, M.E., Smith-Konter, B.R., Pappalardo, R.T., Siefert, F., Collins, G.C., Burkhard, L., 2018d, ArcGIS Map Package with Ganymede imagery and locations of morphological strike-slip indicators: Mendeley Data, doi:10.17632/xkwnhn48hf.2.

Carr, M.H., Belton, M.J.S., Bender, K., Breneman, H., Greeley, R., Head, J.W., Klaasen, K.P., McEwen, A.S., Moore, J.M., and Murchie, S., 1995, The Galileo Imaging Team plan for observing the satellites of Jupiter: Journal of Geophysical Research: Planets, v. 100, p. 18935–18955.

Carr, M.H., Belton, M.J., Chapman, C.R., Davies, M.E., Geissler, P., Greenberg, R., McEwen, A.S., Tufts, B.R., Greeley, R., Sullivan, R., Head, J.W., Pappalardo, R.T., Klaasen, K.P., Johnson, T.V., et al., 1998, Evidence for a subsurface ocean on Europa: Nature, v. 391, p. 363–365, doi: 10.1038/34857.

Casacchia, R., and Strom, R.G., 1984, Geologic evolution of Galileo Regio, Ganymede: Journal of Geophysical Research: Solid Earth, v. 89, p. B419–B428, doi: 10.1029/JB089iS02p0B419.

Chyba, C.F., and Phillips, C.B., 2001, Possible ecosystems and the search for life on Europa: Proceedings of the National Academy of Sciences, v. 98, p. 801–804, doi: 10.1073/pnas.98.3.801.

Collettini, C., and Trippetta, F., 2007, A slip tendency analysis to test mechanical and structural control on aftershock rupture planes: Earth and Planetary Science Letters, v. 255, p. 402–413.

Collins, G., 2009, The origin of grooved terrain on Ganymede, in p. 516, http://adsabs.harvard.edu/abs/2009epsc.conf..516C (accessed February 2018).

Collins, G.C., Head, J.W., and Pappalardo, R.T., 1998a, Formation of Ganymede grooved terrain by sequential extensional episodes: Implications of Galileo observations for regional stratigraphy: Icarus, v. 135, p. 345–359.

Collins, G.C., Head, J.W., and Pappalardo, R.T., 1998b, The role of extensional instability in creating Ganymede grooved terrain: Insights from Galileo High-Resolution Stereo Imaging: Geophysical Research Letters, v. 25, p. 233–236.

Collins, G.C., Head, J.W., Pappalardo, R.T., and Team, G.S., 2000, A global database of grooves and dark terrain on Ganymede, enabling quantitative assessment of terrain features, in Lunar and Planetary Science Conference, v. 31.

Collins, G.C., Head, J.W., Pappalardo, R.T., and Team, G.S., 1998, Geology of the Galileo G7 Nun Sulci target area, Ganymede, in Lunar and Planetary Science Conference, v. 29.

Collins, G.C., Patterson, G.W., Head, J.W., Prockter, L., Pappalardo, R.T., Lucchitta, B.K., and Kay, J.P., 2013, Global geologic map of Ganymede: US Department of the Interior, US Geological Survey.

Croft, S.K., Casacchia, R., and Strom, R.G., 1990, Geologic map of the Tiamat Sulcus quadrangle of Ganymede: US Department of the Interior, US Geological Survey.

Croft, S.K., Kargel, J.S., Kirk, R.L., Moore, J.M., Schenk, P.M., and Strom, R.G., 1995, The geology of Triton., in Neptune and Triton, p. 879–947.

Croft, S.K., and Strom, R.G., 1985, Ganymede's Crust: Structural Indicators in the Tiamat Sulcus Quadrangle, in v. 16, p. 156–157, http://adsabs.harvard.edu/abs/1985LPI16156C.

Davis, G.H., Bump, A.P., García, P.E., and Ahlgren, S.G., 2000, Conjugate Riedel deformation band shear zones: Journal of Structural Geology, v. 22, p. 169–190.

Davis, G.H., and Reynolds, S.J., 1996, Structural geology of rocks and regions, in Structural geology of rocks and regions. 2nd edition, Wiley.

Della Corte, V., Schmitz, N., Zusi, M., Castro, J.M., Leese, M., Debei, S., Magrin, D., Michalik, H., Palumbo, P., Jaumann, R. and Cremonese, G., 2014, The JANUS camera onboard JUICE mission for Jupiter system optical imaging. In Space Telescopes and Instrumentation 2014: Optical, Infrared, and Millimeter Wave, vol. 9143, p. 91433I.

Deremer, L.C., and Pappalardo, R.T., 2003, Manifestations of strike-slip faulting on Ganymede, in Lunar and Planetary Science Conference, v. 34.

Dewey, J.F., Holdsworth, R.E., and Strachan, R.A., 1998, Transpression and transtension zones: Geological Society, London, Special Publications, v. 135, p. 1–14.

Dombard, A.J., and McKinnon, W.B., 2006, Folding of Europa's icy lithosphere: an analysis of viscous-plastic buckling and subsequent topographic relaxation: Journal of structural geology, v. 28, p. 2259–2269.

Dombard, A.J., and McKinnon, W.B., 2001, Formation of Grooved Terrain on Ganymede: Extensional Instability Mediated by Cold, Superplastic Creep: Icarus, v. 154, p. 321–336, doi: 10.1006/icar.2001.6728.

Drake, S., 1976, Galileo's First Telescopic Observations: Journal for the History of Astronomy, v. 7, p. 153.

Dzurisin, D., 1978, The tectonic and volcanic history of Mercury as inferred from studies of

scarps, ridges, troughs, and other lineaments: Journal of Geophysical Research: Solid Earth, v. 83, p. 4883–4906.

Farrell, W.E., 1973, Earth Tides, Ocean Tides and Tidal Loading: Philosophical Transactions of the Royal Society of London Series A, v. 274, p. 253–259, doi: 10.1098/rsta.1973.0050.

Faulkner, D.R., Lewis, A.C., and Rutter, E.H., 2003, On the internal structure and mechanics of large strike-slip fault zones: field observations of the Carboneras fault in southeastern Spain: Tectonophysics, v. 367, p. 235–251.

Figueredo, P.H., Greeley, R., and Galileo SSI Team, 1999, Fracture Patterns on Ganymede and the Initiation of Tectonic Resurfacing, in v. 30, http://adsabs.harvard.edu/abs/1999LPI301832F.

Fortt, A.L., and Schulson, E.M., 2007, The resistance to sliding along Coulombic shear faults in ice: Acta materialia, v. 55, p. 2253–2264.

Gault, D.E., and Wedekind, J.A., 1978, Experimental studies of oblique impact, in Lunar and Planetary Science Conference Proceedings, v. 9, p. 3843–3875.

Geissler, P.E., Greenberg, R., Hoppa, G., Helfenstein, P., McEwen, A., Pappalardo, R., Tufts, R., Ockert-Bell, M., Sullivan, R., and Greeley, R., 1998, Evidence for non-synchronous rotation of Europa: Nature, v. 391, p. 368.

Goldsby, D.L., and Kohlstedt, D.L., 2001, Superplastic deformation of ice: Experimental observations: Journal of Geophysical Research: Solid Earth, v. 106, p. 11017–11030, doi: 10.1029/2000JB900336.

Golombek, M.P., 1982, Constraints on the expansion of Ganymede and the thickness of the lithosphere: Journal of Geophysical Research: Solid Earth, v. 87.

Golombek, M.P., Tanaka, K.L., and Franklin, B.J., 1996, Extension across Tempe Terra, Mars, from measurements of fault scarp widths and deformed craters: Journal of Geophysical Research: Planets, v. 101, p. 26119–26130.

Grasset, O., Dougherty, M.K., Coustenis, A., Bunce, E.J., Erd, C., Titov, D., Blanc, M., Coates, A., Drossart, P., Fletcher, L.N., Hussmann, H., Jaumann, R., Krupp, N., Lebreton, J.-P., et al., 2013, JUpiter ICy moons Explorer (JUICE): An ESA mission to orbit Ganymede and to characterise the Jupiter system: Planetary and Space Science, v.

78, p. 1–21, doi: 10.1016/j.pss.2012.12.002.

Graymer, R.W., Sarna-Wojcicki, A.M., Walker, J.P., McLaughlin, R.J., and Fleck, R.J., 2002, Controls on timing and amount of right-lateral offset on the East Bay fault system, San Francisco Bay region, California: Geological Society of America Bulletin, v. 114, p. 1471–1479, doi: 10.1130/0016-7606(2002)114<1471:COTAAO>2.0.CO;2.

Greenberg, R., 1987, Galilean satellites: Evolutionary paths in deep resonance: Icarus, v. 70, p. 334–347.

Greenberg, R., Geissler, P., Hoppa, G., Tufts, B.R., Durda, D.D., Pappalardo, R., Head, J.W., Greeley, R., Sullivan, R., and Carr, M.H., 1998, Tectonic processes on Europa: Tidal stresses, mechanical response, and visible features: Icarus, v. 135, p. 64–78.

Grundy, W.M., Buratti, B.J., Cheng, A.F., Emery, J.P., Lunsford, A., McKinnon, W.B., Moore, J.M., Newman, S.F., Olkin, C.B., and Reuter, D.C., 2007, New horizons mapping of Europa and Ganymede: Science, v. 318, p. 234–237.

Guest, J.E., Bianchi, R., and Greeley, R., 1988, Geologic map of the Uruk Sulcus quadrangle of Ganymede.:

Hanel, R., Conrath, B., Flasar, M., Kunde, V., Lowman, P., Maguire, W., Pearl, J., Pirraglia, J., Samuelson, R., and Gautier, D., 1979, Infrared observations of the Jovian system from Voyager 1: Science, v. 204, p. 972–976.

Hansen, V.L., 2000, Geologic mapping of tectonic planets: Earth and Planetary Science Letters, v. 176, p. 527–542.

Harding, T.P., 1974, Petroleum traps associated with wrench faults: AAPG bulletin, v. 58, p. 1290–1304.

Hartmann, W.K., 1984, Does crater “saturation equilibrium” occur in the Solar System? Icarus, v. 60, p. 56–74.

Head, J., Pappalardo, R., Collins, G., Belton, M.J., Giese, B., Wagner, R., Breneman, H., Spaun, N., Nixon, B., and Neukum, G., 2002, Evidence for Europa-like tectonic resurfacing styles on Ganymede: Geophysical Research Letters, v. 29.

Head, J.W., Pappalardo, R.T., Kay, J., Collins, G., Prockter, L., Greeley, R., Chapman, C., Carr, M., Belton, M.J.S., and Team, G.I., 1998, Cryovolcanism on Ganymede: Evidence in bright terrain from Galileo solid state imaging data, in Lunar and Planetary Science

Conference, v. 29.

Head, J.W., Pieters, C., McCord, T., Adams, J., and Zisk, S., 1978, Definition and detailed characterization of lunar surface units using remote observations: Icarus, v. 33, p. 145–172.

Helfenstein, P., and Parmentier, E.M., 1980, Fractures on Europa-Possible response of an ice crust to tidal deformation, in Lunar and Planetary Science Conference Proceedings, v. 11, p. 1987–1998.

Helfenstein, P., and Parmentier, E.M., 1985, Patterns of fracture and tidal stresses due to nonsynchronous rotation: Implications for fracturing on Europa: Icarus, v. 61, p. 175–184.

Hoppa, G., Tufts, B.R., Greenberg, R., and Geissler, P., 1999, Strike–slip faults on Europa: Global shear patterns driven by tidal stress: Icarus, v. 141, p. 287–298.

Hurford, T.A., Sarid, A.R., and Greenberg, R., 2007, Cycloidal cracks on Europa: Improved modeling and non-synchronous rotation implications: Icarus, v. 186, p. 218–233, doi: https://doi.org/10.1016/j.icarus.2006.08.026.

Hurford, T.A., Sarid, A.R., Greenberg, R., and Bills, B.G., 2009, The influence of obliquity on europan cycloid formation: Icarus, v. 202, p. 197–215.

Ito, T., and Malhotra, R., 2010. Asymmetric impacts of near-Earth asteroids on the Moon. Astronomy and Astrophysics, 519, A63.

Jara-Orué, H.M., and Vermeersen, B.L.A., 2016, Tides on Jupiter's moon Ganymede and their relation to its internal structure: Netherlands Journal of Geosciences, v. 95, p. 191–201.

Jeager, J.C., and Cook, N.G.W., 1979, Fundamentals of rock mechanics, 593 pág: Chapman & Hall Pub., Londres.

Jones, K.B., Head III, J.W., Pappalardo, R.T., and Moore, J.M., 2003, Morphology and origin of palimpsests on Ganymede based on Galileo observations: Icarus, v. 164, p. 197–212.

Kattenhorn, S.A., 2002, Nonsynchronous rotation evidence and fracture history in the Bright Plains region, Europa: Icarus, v. 157, p. 490–506.

Kattenhorn, S.A., 2004, Strike-slip fault evolution on Europa: evidence from tailcrack

geometries: Icarus, v. 172, p. 582–602.

Kattenhorn, S.A., and Hurford, T.A., 2009, Tectonics of Europa, in Pappalardo, R.T., McKinnon, W.B., and Khurana, K. eds., Europa, Tuscon, University of Arizona Press, p. 199–236.

Kawamura, T., Morota, T., Kobayashi, N. and Tanaka, S., 2011. Cratering asymmetry on the Moon: new insight from the Apollo passive seismic experiment. Geophysical Research Letters, v. 38, p. 15.

Kay, J.E., and Head III, J.W., 1999, Geologic mapping of the Ganymede G8 Calderas region: Evidence for cryovolcanism, in Lunar and Planetary Science Conference, v. 30.

Keller, J.V.A., Hall, S.H., Dart, C.J., and McClay, K.R., 1995, The geometry and evolution of a transpressional strike-slip system: the Carboneras fault, SE Spain: Journal of the Geological Society, v. 152, p. 339–351.

Keszthelyi, L., Becker, T.L., Sides, S., Barrett, J., Cook, D., Lambright, S., Lee, E., Milazzo, M., Oyama, K., and Richie, J., 2013, Support and future vision for the integrated software for imagers and spectrometers (ISIS), in Lunar and Planetary Science Conference, v. 44, p. 2546.

Keszthelyi, L., Becker, T., Titus, T., Sides, S., Gaddis, L., Hare, T., Kirk, R., Edmundson, K., and Anderson, J., 2014, Utilizing the Integrated Software for Imagers and Spectrometers (ISIS) to support future missions, in Lunar and Planetary Science Conference, v. 45, p. 1686.

Kingma, J.T., 1958, The Tongaporutuan sedimentation in central Hawke's Bay: New Zealand journal of geology and geophysics, v. 1, p. 1–30.

Kivelson, M.G., Khurana, K.K., Coroniti, F.V., Joy, S., Russell, C.T., Walker, R.J., Warnecke, J., Bennett, L., and Polanskey, C., 1997, The magnetic field and magnetosphere of Ganymede: Geophysical Research Letters, v. 24, p. 2155–2158.

Kivelson, M.G., Khurana, K.K., Russell, C.T., Volwerk, M., Walker, R.J., and Zimmer, C., 2000, Galileo magnetometer measurements: A stronger case for a subsurface ocean at Europa: Science, v. 289, p. 1340–1343.

Kivelson, M.G., Khurana, K.K., Russell, C.T., Walker, R.J., Warnecke, J., Coroniti, F.V., Polanskey, C., Southwood, D.J., and Schubert, G., 1996, Discovery of Ganymede's

magnetic field by the Galileo spacecraft: Nature, v. 384, p. 537.

Kivelson, M.G., Khurana, K.K., and Volwerk, M., 2002, The permanent and inductive magnetic moments of Ganymede: Icarus, v. 157, p. 507–522.

Lawson, A.E., 2002, What does Galileo's discovery of Jupiter's moons tell us about the process of scientific discovery? Science & Education, v. 11, p. 1–24.

Lee Allison, M., and Clifford, S.M., 1987, Ice-covered water volcanism on Ganymede: Journal of Geophysical Research: Solid Earth, v. 92, p. 7865–7876, doi: 10.1029/JB092iB08p07865.

Leith, A.C., and McKinnon, W.B., 1996, Is there evidence for polar wander on Europa? Icarus, v. 120, p. 387–398.

Lingenauber, K., Hussmann, H., Michaelis, H., Oberst, J., Kobayashi, M., Namiki, N., Thomas, N. and Seiferlin, K., 2014. The Ganymede Laser Altimeter (GALA) on ESA's JUICE mission: Overview of the instrument design. Instrument for Planetary Mission (IPM).

Lisle, R.J., and Srivastava, D.C., 2004, Test of the frictional reactivation theory for faults and validity of fault-slip analysis: Geology, v. 32, p. 569–572.

Lopes, R.M., and Spencer, J.R., 2007, Io after Galileo: a new view of Jupiter's volcanic moon: Springer Science & Business Media.

Lucchita, B.K., 1980, Grooved terrain on Ganymede: Icarus, v. 44, p. 481–501.

Malhotra, R., 1991, Tidal origin of the Laplace resonance and the resurfacing of Ganymede: Icarus, v. 94, p. 399–412.

Martin, E.S., 2016, The distribution and characterization of strike-slip faults on Enceladus: Geophysical Research Letters, v. 43, p. 2456–2464.

McKinnon, W.B., and Melosh, H.J., 1980, Evolution of planetary lithospheres: Evidence from multiringed structures on Ganymede and Callisto: Icarus, v. 44, p. 454–471.

McKinnon, W.B., and Parmentier, E.M., 1986, Ganymede and Callisto, Satellites JA Burns, MS Matthews, 718–763: University of Arizona Press, Tucson.

Means, W.D., 2012, Stress and strain: basic concepts of continuum mechanics for geologists: Springer Science & Business Media.

Melosh, H.J., 1977, Global tectonics of a despun planet: Icarus, v. 31, p. 221–243.

Melosh, H.J., 1989, Impact cratering: A geologic process: Research supported by NASA. New York, Oxford University Press (Oxford Monographs on Geology and Geophysics, No. 11), 1989, 253 p., v. 11.

Melosh, H.J., 1975, Large impact craters and the Moon's orientation: Earth and Planetary Science Letters, v. 26, p. 353–360.

Melosh, H.J., 2011. Planetary surface processes. Cambridge University Press, v. 13.

Michalski, J.R., and Greeley, R., 2002, *En echelon* ridge and trough structures on Europa: Geophysical research letters, v. 29.

Mitri, G., and Showman, A.P., 2005, Convective–conductive transitions and sensitivity of a convecting ice shell to perturbations in heat flux and tidal-heating rate: Implications for Europa: Icarus, v. 177, p. 447–460, doi: 10.1016/j.icarus.2005.03.019.

Moeck, I., Kwiatek, G., and Zimmermann, G., 2009, Slip tendency analysis, fault reactivation potential and induced seismicity in a deep geothermal reservoir: Journal of Structural Geology, v. 31, p. 1174–1182.

Moore, J.M., Asphaug, E., Belton, M.J., Bierhaus, B., Breneman, H.H., Brooks, S.M., Chapman, C.R., Chuang, F.C., Collins, G.C., and Giese, B., 2001, Impact features on Europa: results of the Galileo Europa Mission (GEM): Icarus, v. 151, p. 93–111.

Moore, J.M., Asphaug, E., Morrison, D., Spencer, J.R., Chapman, C.R., Bierhaus, B., Sullivan, R.J., Chuang, F.C., Klemaszewski, J.E., and Greeley, R., 1999, Mass movement and landform degradation on the icy Galilean satellites: Results of the Galileo nominal mission: Icarus, v. 140, p. 294–312.

Moore, J.M., Asphaug, E., Sullivan, R.J., Klemaszewski, J.E., Bender, K.C., Greeley, R., Geissler, P.E., McEwen, A.S., Turtle, E.P., and Phillips, C.B., 1998, Large impact features on Europa: Results of the Galileo nominal mission: Icarus, v. 135, p. 127–145.

Moore, J.M., and Malin, M.C., 1988, Dome craters on Ganymede: Geophysical Research Letters, v. 15, p. 225–228.

Moore, W.B., and Schubert, G., 2000, The tidal response of Europa: Icarus, v. 147, p. 317–319.

Moore, W.B. and Schubert, G., 2003. The tidal response of Ganymede and Callisto with and without liquid water oceans. Icarus, v. 166, p. 223-226.

Morota, T. and Furumoto, M., 2003. Asymmetrical distribution of rayed craters on the Moon. Earth and Planetary Science Letters, 206(3-4), pp.315-323.

Morris, A., Ferrill, D.A., and Henderson, D.B., 1996, Slip-tendency analysis and fault reactivation: Geology, v. 24, p. 275–278.

Morrison, D., 1982, Satellites of Jupiter, in Satellites of Jupiter.

Murchie, S.L., and Head, J.W., 1989, Geologic map of the Philus Sulcus (Jg-4) quadrangle of Ganymede: US Geol. Surv. Map I-1966.

Murchie, S.L., and Head, J.W., 1988, Possible breakup of dark terrain on Ganymede by large-scale shear faulting: Journal of Geophysical Research: Solid Earth, v. 93, p. 8795–8824.

Murchie, S.L., Head, J.W., Helfenstein, P., and Plescia, J.B., 1986, Terrain types and local-scale stratigraphy of grooved terrain on Ganymede: Journal of Geophysical Research: Solid Earth, v. 91.

Murchie, S.L., Head, J.W., and Plescia, J.B., 1989, Crater densities and crater ages of different terrain types on Ganymede: Icarus, v. 81, p. 271–297.

Murray, C.D., and Dermott, S.F., 1999, Solar system dynamics: Cambridge university press.

Naylor, M.A., Mandl, G. t, and Supesteijn, C.H.K., 1986, Fault geometries in basement-induced wrench faulting under different initial stress states: Journal of Structural Geology, v. 8, p. 737–752.

Neukum, G., 1997, Bombardment history of the jovian system, in The Three Galileos: The Man, the Spacecraft, the Telescope, Springer, p. 201–212.

Neukum, G., Wagner, R., Wolf, U., Ivanov, B.A., Head, J.W., Pappalardo, R.T., Klemaszewski, J.E., Greeley, R., and Belton, M.J.S., 1998, Cratering chronology in the Jovian system and derivation of absolute ages: Lunar and Planetary Science XXIX, v. 29, p. 1742-.

Nimmo, F., 2004, What is the Young's Modulus of Ice?, in Workshop on Europa's Icy Shell: Past, Present, and Future.

Nimmo, F., and Gaidos, E., 2002, Strike-slip motion and double ridge formation on Europa: Journal of Geophysical Research: Planets, v. 107, p. 5-1-5–8, doi: 10.1029/2000JE001476.

Nimmo, F., Spencer, J.R., Pappalardo, R.T., and Mullen, M.E., 2007, Shear heating as the origin of the plumes and heat flux on Enceladus: Nature, v. 447, p. 289.

Oberst, J., Schreiner, B., Giese, B., Neukum, G., Head, J.W., Pappalardo, R.T., and Helfenstein, P., 1999, The distribution of bright and dark material on Ganymede in relationship to surface elevation and slopes: Icarus, v. 140, p. 283–293.

Ojakangas, G.W., and Stevenson, D.J., 1989, Thermal state of an ice shell on Europa: Icarus, v. 81, p. 220–241.

Olgin, J.G., Smith-Konter, B.R., and Pappalardo, R.T., 2011, Limits of Enceladus's ice shell thickness from tidally driven tiger stripe shear failure: Geophysical Research Letters, v. 38.

Owen, T., 1976, Jovian satellite nomenclature: Icarus, v. 29, p. 159–163.

Pappalardo, R.T., and Collins, G.C., 2005, Strained craters on Ganymede: Journal of structural geology, v. 27, p. 827–838.

Pappalardo, R.T., Collins, G.C., Head, J.W., Helfenstein, P., McCord, T.B., Moore, J.M., Prockter, L.M., Schenk, P.M., and Spencer, J.R., 2004, Geology of Ganymede, in Bagenal, F.D., Dowling, T.E., and McKinnon, W.B. eds., Jupiter, Cambridge, UK, Cambridge University Press, Cambridge planetary science, p. 363–396.

Pappalardo, R.T., and Greeley, R., 1995, A review of the origins of subparallel ridges and troughs: Generalized morphological predictions from terrestrial models: Journal of Geophysical Research: Planets, v. 100, p. 18985–19007.

Pappalardo, R.T., Head, J.W., Collins, G.C., Kirk, R.L., Neukum, G., Oberst, J., Giese, B., Greeley, R., Chapman, C.R., Helfenstein, P., Moore, J.M., McEwen, A., Tufts, B.R., Senske, D.A., et al., 1998, Grooved Terrain on Ganymede: First Results from Galileo High-Resolution Imaging: Icarus, v. 135, p. 276–302, doi: 10.1006/icar.1998.5966.

Pappalardo, R.T., Smith-Konter, B.R., Cameron, M.E., DeRemer-Keeney, L.C., and Nimmo, F., 2012, Strike-slip Faulting On Ganymede, Now And Then, in AAS/Division for Planetary Sciences Meeting Abstracts, v. 44.

Pasachoff, J.M., 2015, Simon Marius's Mundus Iovialis: 400th Anniversary in Galileo's Shadow: Journal for the History of Astronomy, v. 46, p. 218–234, doi: 10.1177/0021828615585493.

Patel, J.G., Pappalardo, R.T., Head, J.W., Collins, G.C., Hiesinger, H., and Sun, J., 1999, Topographic wavelengths of Ganymede groove lanes from Fourier analysis of Galileo images: Journal of Geophysical Research: Planets, v. 104, p. 24057–24074.

Patterson, G.W., Collins, G.C., Head, J.W., Pappalardo, R.T., Prockter, L.M., Lucchitta, B.K., and Kay, J.P., 2010, Global geological mapping of Ganymede: Icarus, v. 207, p. 845–867.

Peale, S.J., 1999, Origin and evolution of the natural satellites: Annual Review of Astronomy and Astrophysics, v. 37, p. 533–602.

Peale, S.J., 1977, Rotation histories of the natural satellites, in IAU Colloq. 28: Planetary Satellites, p. 87–111.

Peale, S.J., and Lee, M.H., 2003, On the origin of the Laplace relation among the Galilean satellites, in Bulletin of the American Astronomical Society, v. 35, p. 1047.

Phillips, C.B., and Pappalardo, R.T., 2014, Europa clipper mission concept: exploring Jupiter's ocean moon: Eos, Transactions American Geophysical Union, v. 95, p. 165–167.

Pizzi, A., Domenica, A.D., Komatsu, G., Cofano, A., Mitri, G., and Bruzzone, L., 2017, Spreading vs. Rifting as modes of extensional tectonics on the globally expanded Ganymede: Icarus, v. 288, p. 148–159, doi: 10.1016/j.icarus.2017.01.034.

Plaut, S., Barabash, S., Bruzzone, L., Dougherty, M.K., Erd, C., Fletcher, L., Gladstone, R., Grasset, O., Gurvits, L., Hartogh, P. and Hussmann, H., 2014. Jupiter Icy Moons Explorer (JUICE): Science Objectives, Mission and Instruments.

Pollard, D.D., Segall, P., and Delaney, P.T., 1982, Formation and interpretation of dilatant echelon cracks: Geological Society of America Bulletin, v. 93, p. 1291–1303.

Porco, C.C., West, R.A., McEwen, A., Del Genio, A.D., Ingersoll, A.P., Thomas, P., Squyres, S., Dones, L., Murray, C.D., and Johnson, T.V., 2003, Cassini imaging of Jupiter's atmosphere, satellites, and rings: Science, v. 299, p. 1541–1547.

Prockter, L.M., Figueredo, P.H., Pappalardo, R.T., Head, J.W., and Collins, G.C., 2000, Geology and mapping of dark terrain on Ganymede and implications for grooved terrain formation: Journal of Geophysical Research: Planets, v. 105, p. 22519–22540.

Prockter, L.M., Head, J.W., Pappalardo, R.T., Senske, D.A., Neukum, G., Wagner, R., Wolf,

U., Oberst, J.O., Giese, B., and Moore, J.M., 1998, Dark terrain on Ganymede: Geological mapping and interpretation of Galileo Regio at high resolution: Icarus, v. 135, p. 317–344.

Prockter, L.M., Pappalardo, R.T., and Head, J.W., 2000, Strike-slip duplexing on Jupiter's icy moon Europa: Journal of Geophysical Research: Planets, v. 105, p. 9483–9488.

Ramsay, J., 1967, Folding and fracturing of rocks:

Ramsay, J.G., and Huber, M.I., 1983, Strain analysis, The techniques of modern structural geology, Vol. 1: Strain Analysis. Academic Press, London.

Reading, H.G., 1980, Characteristics and recognition of strike-slip fault systems: Sedimentation in oblique-slip mobile zones, v. 4, p. 7–26.

Rhoden, A.R., Hurford, T.A., and Manga, M., 2011, Strike-slip fault patterns on Europa: Obliquity or polar wander? Icarus, v. 211, p. 636–647.

Rhoden, A.R., Militzer, B., Huff, E.M., Hurford, T.A., Manga, M., and Richards, M.A., 2010, Constraints on Europa's rotational dynamics from modeling of tidally-driven fractures: Icarus, v. 210, p. 770–784.

Rhoden, A.R., Wurman, G., Huff, E.M., Manga, M., and Hurford, T.A., 2012, Shell tectonics: A mechanical model for strike-slip displacement on Europa: Icarus, v. 218, p. 297–307.

Schenk, P., 2010, Atlas of the Galilean satellites: Cambridge University Press.

Schenk, P.M., Chapman, C.R., Zahnle, K., and Moore, J.M., 2004, Ages and interiors: The cratering record of the Galilean satellites: Jupiter: The planet, satellites and magnetosphere, p. 427–456.

Schenk, P., Matsuyama, I., and Nimmo, F., 2008, True polar wander on Europa from global-scale small-circle depressions: Nature, v. 453, p. 368.

Schenk, P.M., McKinnon, W.B., Gwynn, D., and Moore, J.M., 2001, Flooding of Ganymede's bright terrains by low-viscosity water-ice lavas: Nature, v. 410, p. 57.

Schenk, P.M., and Moore, J.M., 1995, Volcanic constructs on Ganymede and Enceladus: Topographic evidence from stereo images and photoclinometry: Journal of Geophysical Research: Planets, v. 100, p. 19009–19022.

Schenk, P.M. and Sobieszczyk, S., 1999. Cratering asymmetries on Ganymede and Triton:

from the sublime to the ridiculous, in Bulletin of the American Astronomical Society, v. 31, p. 1182.

Schmidt, B.E., Blankenship, D.D., Patterson, G.W., and Schenk, P.M., 2011, Active formation of 'chaos terrain'over shallow subsurface water on Europa: Nature, v. 479, p. 502.

Schubert, G., Anderson, J.D., Spohn, T., and McKinnon, W.B., 2004, Interior composition, structure and dynamics of the Galilean satellites: Jupiter: The planet, satellites and magnetosphere, v. 1, p. 281–306.

Schubert, G., Zhang, K., Kivelson, M.G., and Anderson, J.D., 1996, The magnetic field and internal structure of Ganymede: Nature, v. 384, p. 544.

Schulson, E.M., and Fortt, A.L., 2012, Friction of ice on ice: Journal of Geophysical Research: Solid Earth, v. 117.

Segall, P., and Pollard, D.D., 1980, Mechanics of discontinuous faults: Journal of Geophysical Research: Solid Earth, v. 85, p. 4337–4350.

Shoemaker, E.M., Lucchitta, B.K., Wilhelms, D.E., Plescia, J.B., and Squyres, S.W., 1982, The geology of Ganymede, in Satellites of Jupiter, p. 435–520.

Shoemaker, E.M., and Wolfe, R.F., 1982, Cratering time scales for the Galilean satellites, in Satellites of Jupiter, p. 277–339.

Showman, A.P., and Malhotra, R., 1999, The galilean satellites: Science, v. 286, p. 77–84.

Showman, A.P., and Malhotra, R., 1997, Tidal evolution into the Laplace resonance and the resurfacing of Ganymede: Icarus, v. 127, p. 93–111.

Showman, A.P., Stevenson, D.J., and Malhotra, R., 1997, Coupled Orbital and Thermal Evolution of Ganymede: Icarus, v. 129, p. 367–383, doi: 10.1006/icar.1997.5778.

Smith, B.A., Soderblom, L.A., Beebe, R., Boyce, J., Briggs, G., Carr, M., Collins, S.A., Cook, A.F., Danielson, G.E., and Davies, M.E., 1979, The Galilean satellites and Jupiter: Voyager 2 imaging science results: Science, v. 206, p. 927–950.

Smith, B.A., Soderblom, L.A., Johnson, T.V., Ingersoll, A.P., Collins, S.A., Shoemaker, E.M., Hunt, G.E., Masursky, H., Carr, M.H., and Davies, M.E., 1979, The Jupiter system through the eyes of Voyager 1: Science, v. 204, p. 951–972.

Smith-Konter, B., and Pappalardo, R.T., 2008, Tidally driven stress accumulation and shear

failure of Enceladus's tiger stripes: Icarus, v. 198, p. 435–451.

Sohl, F., Spohn, T., Breuer, D., and Nagel, K., 2002, Implications from Galileo observations on the interior structure and chemistry of the Galilean satellites: Icarus, v. 157, p. 104–119.

Spaun, N.A., Head III, J.W., Pappalardo, R.T., and Team, G.S., 2001, Scalloped depressions on Ganymede from Galileo (G28) very high resolution imaging, in Lunar and Planetary Science Conference, v. 32.

Spaun, N.A., Pappalardo, R.T., and Head, J.W., 2003, Evidence for shear failure in forming near-equatorial lineae on Europa: Journal of Geophysical Research: Planets, v. 108.

Spencer, J.R., 1987, Surfaces of Europa, Ganymede, and Callisto: An investigation using Voyager IRIS thermal infrared spectra: Univ. Arizona, Tucson..

Spohn, T., and Schubert, G., 2003, Oceans in the icy Galilean satellites of Jupiter? Icarus, v. 161, p. 456–467, doi: 10.1016/S0019-1035(02)00048-9.

Squyres, S.W., and Croft, S.K., 1986, The tectonics of icy satellites, in IAU Colloq. 77: Some Background about Satellites, p. 293–341.

Strom, R.G., Croft, S.K. and Boyce, J.M., 1990. The impact cratering record on Triton. Science, 250(4979), pp.437-439.

Survey (US), G., Lucchitta, B.K., Barnes, C.W., and Glotfelty, M.F., 1992, Geologic Map of the Memphis Facula Quadrangle (Jg-7) of Ganymede: The Survey.

Tchalenko, J.S., 1970, Similarities between shear zones of different magnitudes: Geological Society of America Bulletin, v. 81, p. 1625–1640.

Tchalenko, J.S., and Ambraseys, N.N., 1970, Structural analysis of the Dasht-e Bayaz (Iran) earthquake fractures: Geological Society of America Bulletin, v. 81, p. 41–60.

Thatcher, W., and Hill, D.P., 1991, Fault orientations in extensional and conjugate strike-slip environments and their implications: Geology, v. 19, p. 1116–1120.

Thomas, P.G., and Allemand, P., 1993, Quantitative analysis of the extensional tectonics of Tharsis Bulge, Mars: geodynamic implications: Journal of Geophysical Research: Planets, v. 98, p. 13097–13108.

Thomas, A.L., and Pollard, D.D., 1993, The geometry of echelon fractures in rock: implications from laboratory and numerical experiments: Journal of Structural Geology,

v. 15, p. 323–334.

Tittemore, W.C., 1990, Chaotic motion of Europa and Ganymede and the Ganymede-Callisto dichotomy: Science, v. 250, p. 263–267.

Tsurutani, B.T., Southwood, D.J., Smith, E.J., and Balogh, A., 1993, A survey of low frequency waves at Jupiter: The Ulysses encounter: Journal of Geophysical Research: Space Physics, v. 98, p. 21203–21216.

Vetterlein, J., and Roberts, G.P., 2003, Cracking up: faulting on Earth and Mars: Astronomy & Geophysics, v. 44, p. 4.22-4.22.

Wahr, J., Selvans, Z.A., Mullen, M.E., Barr, A.C., Collins, G.C., Selvans, M.M., and Pappalardo, R.T., 2009, Modeling stresses on satellites due to nonsynchronous rotation and orbital eccentricity using gravitational potential theory: Icarus, v. 200, p. 188–206.

Welsh, W.F., Orosz, J.A., Aerts, C., Brown, T.M., Brugamyer, E., Cochran, W.D., Gilliland, R.L., Guzik, J.A., Kurtz, D.W., and Latham, D.W., 2011, KOI-54: The Kepler discovery of tidally excited pulsations and brightenings in a highly eccentric binary: The Astrophysical Journal Supplement Series, v. 197, p. 4.

Wernicke, B., and Burchfiel, B.C., 1982, Modes of extensional tectonics: Journal of Structural Geology, v. 4, p. 105–115.

Wilcox, R.E., Harding, T. t, and Seely, D.R., 1973, Basic wrench tectonics: Aapg Bulletin, v. 57, p. 74–96.

Wilhelms, D.E., 1990, Geologic mapping: Planetary mapping, p. 208.

Wilhelms, D.E., 1972, Geologic mapping of the second planet: USGS Inter-Agency Rep., Astrogeology, v. 55.

Williams, M., 1997, Rene Taton and Curtis Wilson, The General History of Astronomy, Volume 2. Planetary Astronomy from the Renaissance to the Rise of Astrophysics. Part B: The Eighteenth and Nineteenth Centuries. Cambridge: Cambridge University Press, 1995. Pp. xiii+ 281. ISBN 0-521-35168-5.

Woodcock, N.H., and Fischer, M., 1986, Strike-slip duplexes: Journal of structural geology, v. 8, p. 725–735.

Yoder, C.F., 1979, How tidal heating in Io drives the Galilean orbital resonance locks: Nature, v. 279, p. 767.

Yoder, C.F., and Peale, S.J., 1981, The tides of Io: Icarus, v. 47, p. 1–35.

Zahnle, K., Dones, L., and Levison, H.F., 1998, Cratering rates on the Galilean satellites: Icarus, v. 136, p. 202–222.

Zahnle, K., Schenk, P., Levison, H., and Dones, L., 2003, Cratering rates in the outer Solar System: Icarus, v. 163, p. 263–289, doi: 10.1016/S0019-1035(03)00048-4.

Zoback, M.D., Zoback, M.L., Mount, V.S., Suppe, J., Eaton, J.P., Healy, J.H., Oppenheimer, D., Reasenberg, P., Jones, L., and Raleigh, C.B., 1987, New evidence on the state of stress of the San Andreas fault system: Science, v. 238, p. 1105–1111.